Coronal Implosions in Solar Eruptions and Flares

Juntao Wang, M.Sci.

Astronomy and Astrophysics Group
School of Physics and Astronomy
Kelvin Building
University of Glasgow
Glasgow, G12 8QQ
Scotland, U.K.

Presented for the degree of
Doctor of Philosophy
The University of Glasgow
September 2018

This thesis is my own composition except where indicated in the text. No part of this thesis has been submitted elsewhere for any other degree or qualification.

10th September 2018

For my parents and family.

Acknowledgements

I wish to thank Drs. Lyndsay Flecther, Paulo J. A. Simoes, Julia K. Thalmann, Natasha L. S. Jeffrey, Hugh S. Hudson, Iain G. Hannah, and Mr. Paul J. Wright, who have made a lot of contributions to our published works in Chapters 2, 3 and 4.

I also wish to express my sincerest gratitude to Drs. Lyndsay Flecther and Paulo J. A. Simoes, for helping me on the road of understanding solar physics and writting scientific papers, and invaluable guidance, suggestions and advice on research career.

Abstract

Coronal implosions - the convergence motion of plasmas and entrained magnetic field in the corona due to a reduction in magnetic pressure - can help to locate and track sites of magnetic energy release or redistribution during solar flares and eruptions. Although this conjecture was proposed almost two decades ago, observations of such phenomena are still rare, and even our understanding of it is far from complete. In this thesis, following an introduction to the background and techniques used, we first generalise the implosion idea based on its spirit concerning about the relationship between magnetic energy release and field shrinkage, which allows us to unite and explain three different phenomena, that is, peripheral implosions, inflows and dipolarisations, using only one single principle. Previous observations of apparent contractions in the periphery of active regions are mainly in a face-on state, which cannot exclude the possibilty of field inclining instead of a real contraction as the cause. This then motivates us to study an excellent event observed near the solar disk center, and evidence from both observations and coronal magnetic field extrapolations is found to support the implosion idea. In a unification of three main concepts for active region magnetic evolution implied by the observation, namely the metastable eruption model, the implosion conjecture, and the standard "CSHKP" flare model, the contraction of the field is explained by the removal of the erupting filament originally underneath rather than local magnetic energy dissipation in a flare invoked by previous authors.

However, the observation and extrapolation results in the work above are indirect and still not adequate, as the complex structure of the solar atmosphere, and the simplified assumption and preprocessing in the extrapolation may lead us to a wrong conclusion. Thus in the following four carefully seleted events with the continuously contracting loops in an almost edge-on geometry are for the first time investigated, demonstrating the reality of contraction of field lines in the global coronal dynamics

unambiguously. Meanwhile, two categories of implosions, flare- and eruption-driven, are identified, which could be interpreted well in the framework of the implosion conjecture, disproving other authors' proposal. We also revisit one of the original assumptions of the implosion conjecture which may fail when a heavily-mass-loaded filament is involved, and in this case implosions can be suppressed, possibly served as an alternative explanation for their observational rarity.

In the end, we move on to one of the generalised implosion types, i.e., the inflow, and also study other reconnection flows associated with it. Intrinsic to the well-accepted reconnection picture of a solar eruptive event, particularly in the standard model for two-ribbon flares ("CSHKP" model), are an advective flow of magnetized plasma into the reconnection region, expansion of field above the reconnection region as a flux rope erupts, retraction of heated post-reconnection loops, and downflows of cooling plasma along those loops. However, the evidence of these flows is still circumstantial and rare. We report in this work on a unique set of SDO/AIA imaging and Hinode/EIS spectroscopic observations of a flare in which all four flows are present simultaneously. This also includes spectroscopic evidence for a plasma upflow at the edge of the active region claimed by previous authors, which we suggest decomposing into two components, one associated with open field at quasi-separatrix layers, the other with large-scale expanding closed arcade field. The reconnection inflows are symmetric, and consistent with fast reconnection, and the post-reconnection loops show a clear cooling and deceleration as they retract. Unlike previous events observed at the solar limb which are obscured by complex foregrounds and thus makes the relationship between the plasma flows, the flare ribbons, cusp field and arcades formed in the lower atmosphere difficult to interpret, the disk location and favorable perspective of this event studied here have removed these ambiguities giving a clear picture of the reconnection dynamics.

We end with a brief chapter summarizing the thesis and suggesting some future work.

Contents

List of Figures

Chapter 1

Introduction

Part of the chapter can be found in my annual reports and the publications Wang et al. (2016, 2017, 2018).

1.1 The Sun and Its Atmosphere

The Sun (Figure 1.1) is an ordinary star with an age around five billion years on the main sequence and located in the center of the solar system in the Galaxy. It continuously provides energy via nuclear fusion in the core to the home of humanity, the Earth, but also creates dramatic events of destructive effects to our life and surrounding environment. This makes the study of the Sun a necessity. The Sun is a huge fireball consisting of plasma where ions and electrons interact with each other ($\sim$ 92 % H, $\sim$ 8 % He, and 0.1 % heavier elements by number, such as C, N and O), in which inward gravity and outward pressure gradient balance. It has a diameter of ~ 695.5 Mm, a mass $\sim 1.99 \times 10^{30}$ kg, and a luminosity $\sim 3.86 \times 10^{33}$ W.

The interior of the Sun has been investigated by modelling and helioseismology by which photospheric oscillations can be used to derive solar internal structures and properties. It comprises three regions, the core, radiative zone and convection zone, illustrated in Figure 1.2. In the core energy is released through the fusion of H to He. The generated high energy photons (gamma rays) are absorbed and emitted repeatedly in the radiative zone until they can escape into the convection zone where the energy transport is dominant by plasma convection. At the bottom of the convection zone, a strong shear layer called the tachocline may exist that can create intense magnetic flux transported upward by convection.

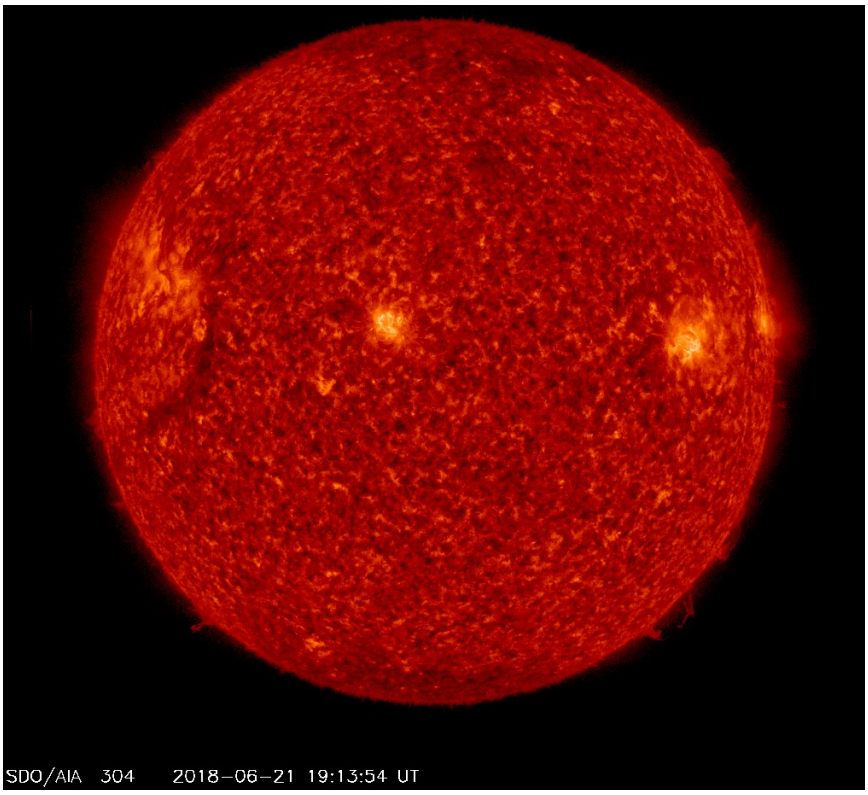

Figure 1.1: The Sun captured by the observatory SDO/AIA in 304 Å. Taken from https://sdo.gsfc.nasa.gov/data/.

The solar atmosphere is the outer part of the Sun, and also the direct source of radiation from the Sun as below the atmosphere photons cannot escape into space because of the optical thickness $\tau \gg 1$. According to different physical properties, the atmosphere is mainly divided into three layers, that is, from bottom to top, photosphere, chromosphere, and corona (Figure 1.2). With a thickness ~ 0.5 Mm, temperature ~ 5800 K and electron density $\sim 10^{23}$ m^{-3}, the photosphere contributes to most of the solar radiation. The chromosphere is optically thick in strong spectral lines, it thus absorbs radiation from the photosphere underneath, accounting for remarkable absorption lines in observed solar spectra. It has a thickness ~ 2.5 Mm, temperature $\sim 10^4$ K, and electron density decreases from the photospheric level to 10^{15} m^{-3}. Above the chromosphere, through a very thin transition region (a few 100 km thick), the temperature dramatically increases to the coronal level $\sim 10^6$ K, while the electron density decreases further by about one order of magnitude. The corona extends upward with a thickness ~ 7.5 Mm (the bright feature above the solar disk in Figure 1.3). In reality, the solar atmosphere is highly nonuniform and dynamic,

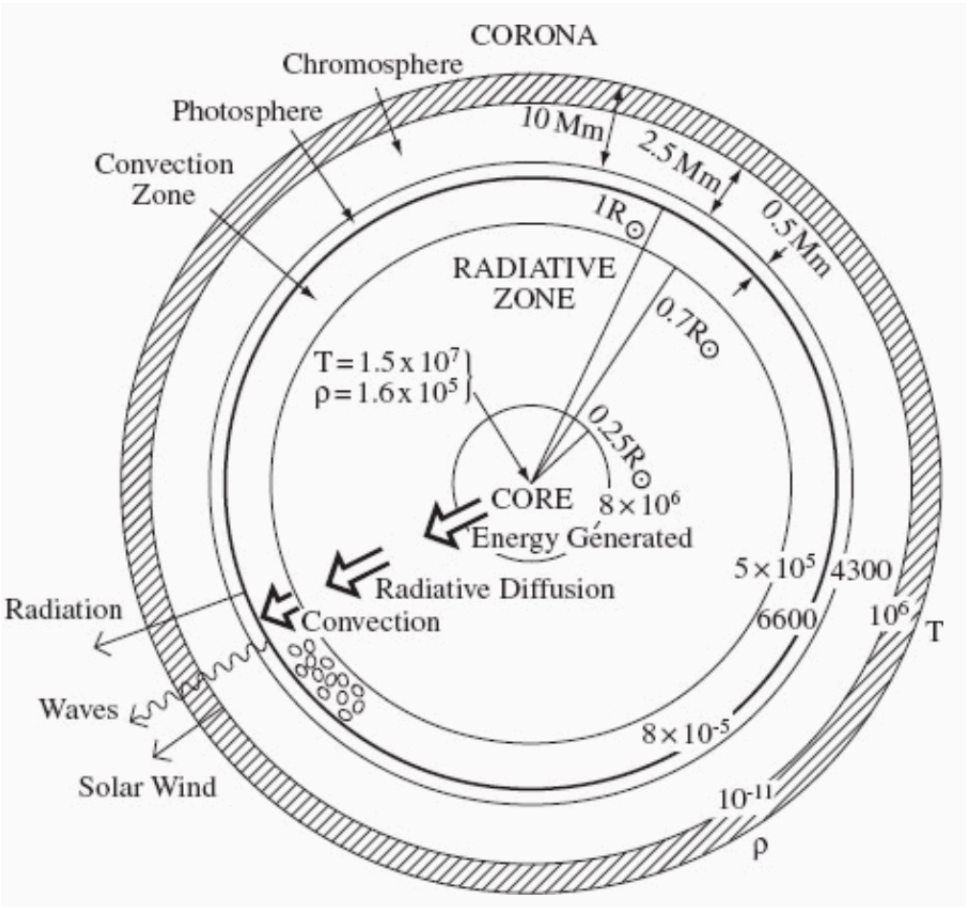

Figure 1.2: The structure of the Sun, from inner to outer, consists of a core, radiative zone, convection zone, photosphere, chromosphere and corona. T is temperature in K, and ρ density in kg m^{-3}. Taken from Priest (2014).

making the three major layers not so easily distinguished.

1.2 Active Regions, Solar Flares and Eruptions

A solar active region is an area where the magnetic field is significantly enhanced (its temperature and density may also be higher than surrounding quiet regions). Figure 1.4(a) shows a magnetogram of the Sun, and the intense magnetic regions are indicated by white and black areas (they separately correspond to positive and negative polarity whose magnetic field vector points toward or in the opposite direction to the observer), which are usually located within ± 30 degrees of the equator and have a mean field strength ∼ 100 G and strongest fields of ∼ 2 kG.

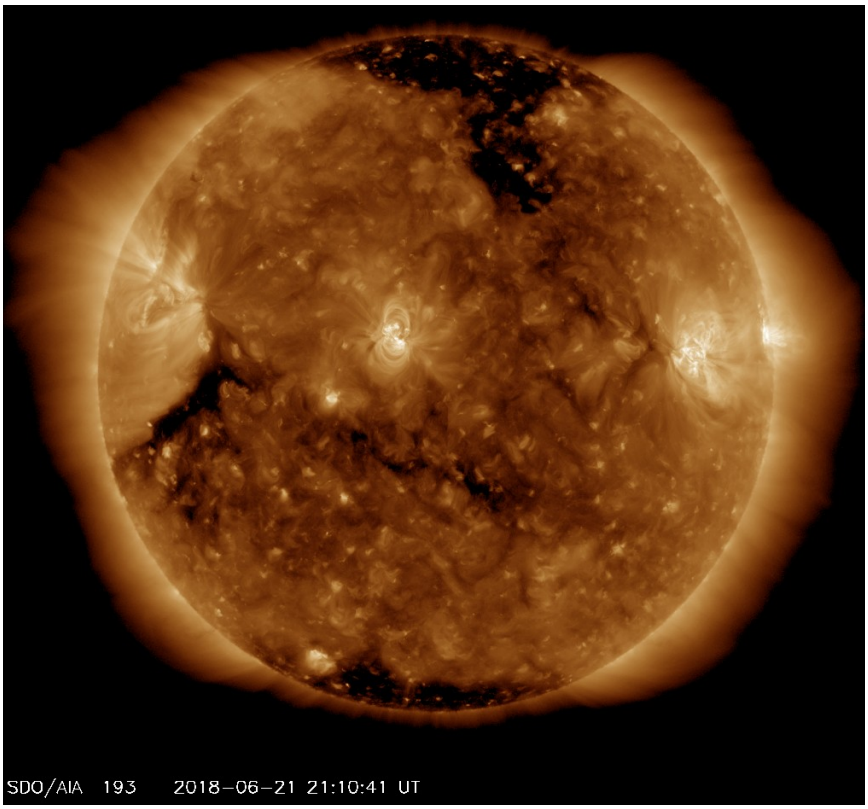

Figure 1.3: The corona of the Sun imaged by the observatory SDO/AIA in 193 Å. Taken from https://sdo.gsfc.nasa.gov/data/.

When the magnetic fields in these regions are strong enough to effectively prohibit convection from surrounding quiet regions, sunspots or dark pores in white light will appear (Figure 1.4(b); Stix 2004). In soft X-ray (SXR) or extreme ultraviolet (EUV) coronal images as in Figure 1.4(c) and (d), they can be seen as regions with bright arches of plasma, called loops. These coronal loops represent magnetic flux tubes connecting opposite polarities, possibly generated in the tachocline and raised up through the photosphere and chromosphere by magnetic buoyancy. Sometimes filaments (viewed on the solar disk in absorption) or prominences (viewed above the solar limb in emission) as in Figure 1.5 can also be seen in active regions, running almost parallel to the magnetic neutral line or polarity inversion line, which separates areas of positive and negative magnetic flux. They possess plasma a hundred times cooler and denser than surrounding corona, and are believed to be held up by upward tension force of twisted magnetic flux ropes, against downward gravity.

A solar flare is a sudden brightening in the solar atmosphere, which usually

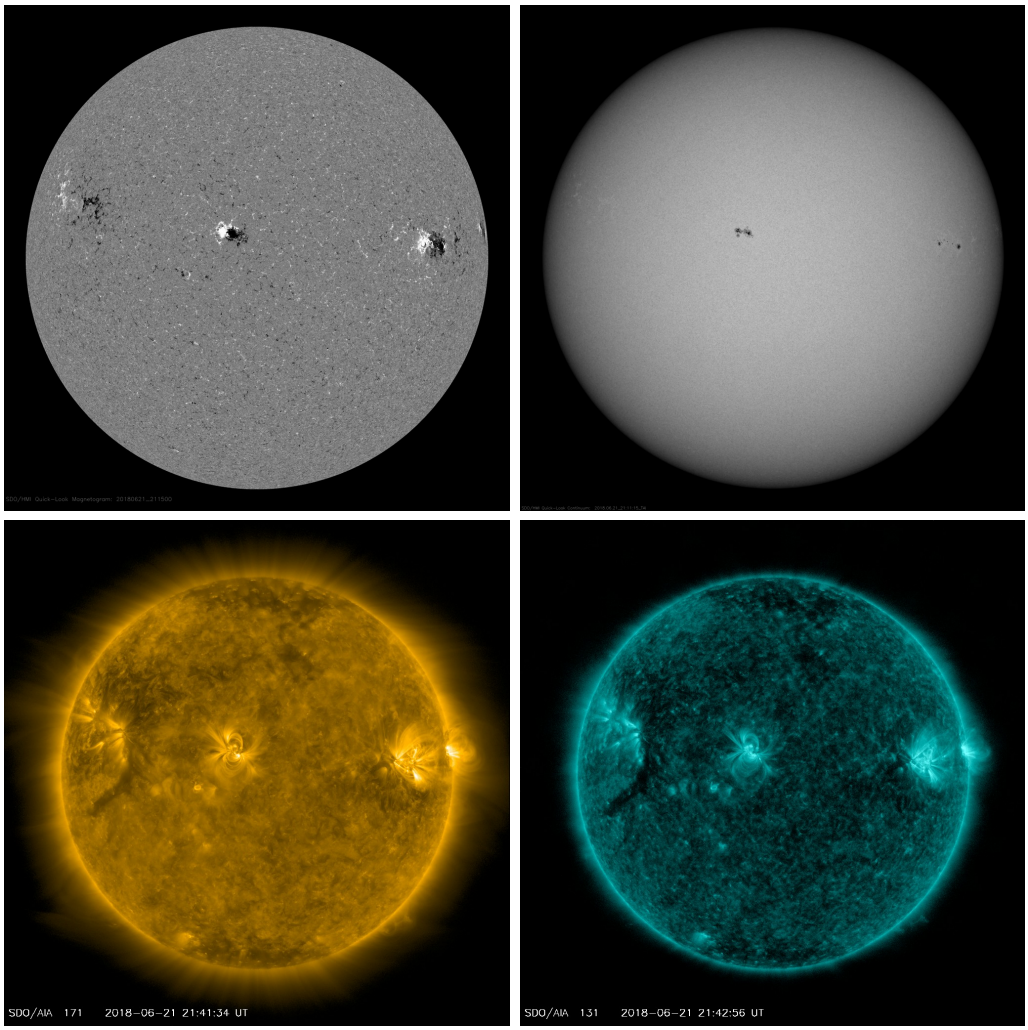

Figure 1.4: (a) Magnetogram of the Sun observed by the observatory SDO/HMI. (b) Intensity map of the Sun observed by SDO/HMI. (c)-(d) Corresponding coronal images by the observatory SDO/AIA in 171 and 131 Å. Taken and adapted from https://sdo.gsfc.nasa.gov/data/.

happens in solar active regions. An excellent example can be seen in Figure 1.6. Flares can be detected from radio up to gamma-ray energy bands. Based on the peak soft X-ray flux measured by the Geostationary Operational Environmental Satellite (GOES) in 1-8 Å, flares can be classified into A (10^{-8} W m^{-2}), B (10^{-7} W m^{-2}), C (10^{-6} W m^{-2}), M (10^{-5} W m^{-2}), X (10^{-4} W m^{-2}) classes. In spatial scales, they can just be a compact bright spot in observation; they can also be a large-scale eruptive flare with dramatic plasma flows or coronal mass ejections (CMEs; large scale plasmoid ejections from the Sun into interplanetary space). As to flare evolution, we can

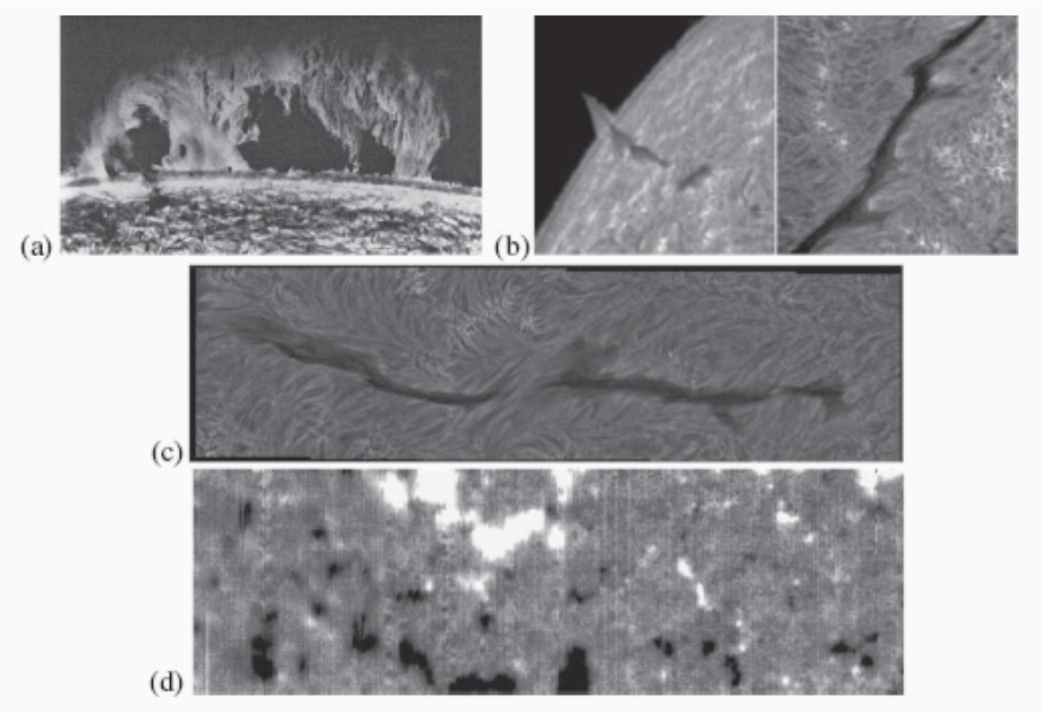

Figure 1.5: Filaments or prominences in an active region of the Sun. (a) Located at the limb, viewd from the side. (b) Located near the limb, viewed from the end and at an oblique angle, respectively. (c) Located on the disk, viewed from above. (d) The corresponding magnetogram (Dudík et al. 2008). Taken from Priest (2014).

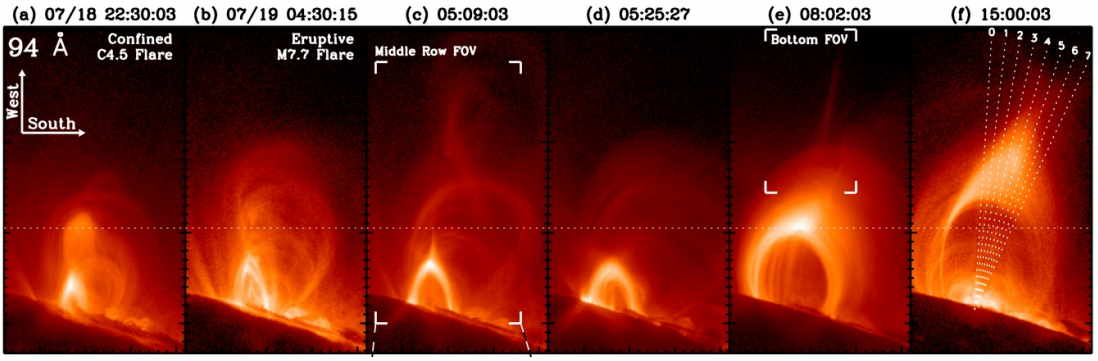

Figure 1.6: Coronal structures in solar flares observed by SDO/AIA in 94 Å. Observational times in UT are labeled above each image. Taken from Liu et al. (2013).

mainly divide it into impulsive and gradual phases. The impulsive phase indicates the rapid hard X-ray (HXR) radiation period when bremsstrahlung from decelerated non-thermal electrons is emitted; after that, the gradual phase begins with thermal emission dominant.

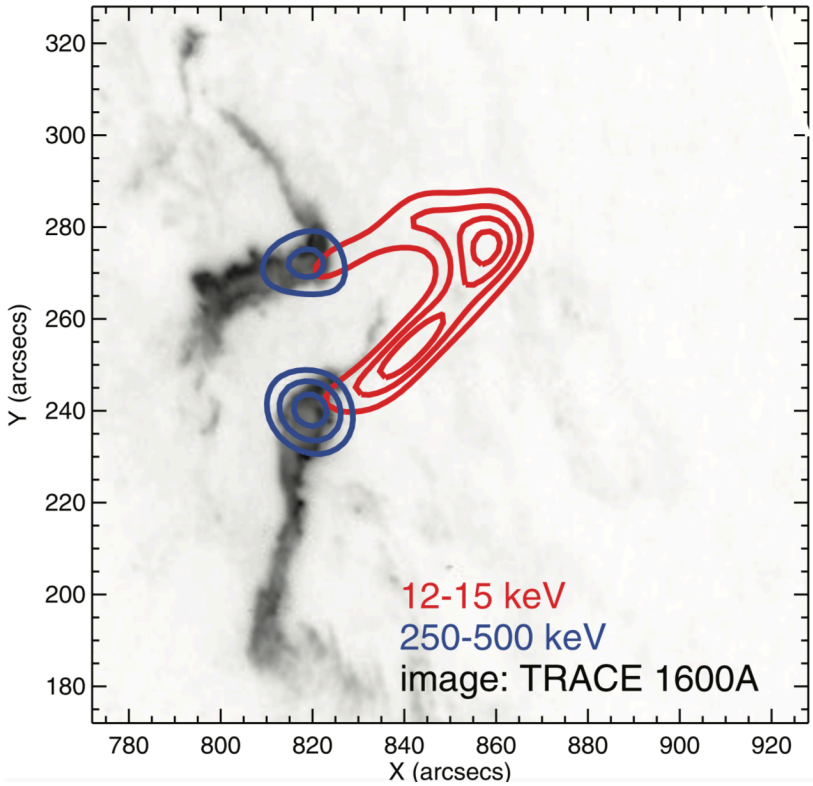

Figure 1.7: A two-ribbon flare observed in X-ray. The 12-15 keV emission is shown in red with contour levels 30%, 50%, 70% and 90%, and the 250-500 keV in blue with contour levels 50%, 70% and 90%. The background image shows the two ribbons in 1600 Å. Taken from Krucker et al. (2008).

Flares are generally believed to be caused by a sudden release of free magnetic energy stored in the preflare magnetic field of the solar corona in the form of electrical currents (McClymont & Fisher 1989; Priest & Forbes 2002). Free magnetic energy is equal to the total magnetic energy of the field with currents, minus the magnetic energy of the potential field, which is the field having the same vertical magnetic flux at the photospheric boundary but carrying no currents. It is built up by distortion of coronal magnetic field, like field line shearing or twisting driven by subphotospheric motion of plasma.

There is a wealth of models for explaining solar flares and eruptions, which can be found at the link `http://solarmuri.ssl.berkeley.edu/~hhudson/cartoons/`. We briefly introduce the standard model for two-ribbon flares (Figure 1.7), the CSHKP model (Carmichael 1964; Sturrock 1966; Hirayama 1974; Kopp & Pneuman 1976), which is mainly used and discussed in this thesis. The model is illustrated in

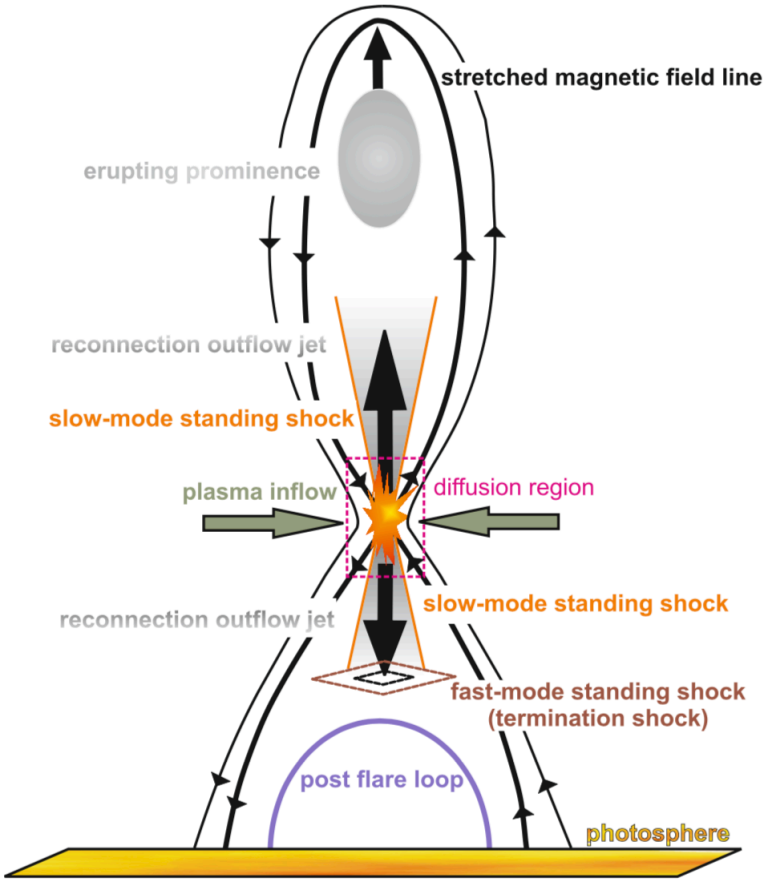

Figure 1.8: The standard CSHKP model of two-ribbon flares. Taken from Mann et al. (2009).

Figure 1.8. As the erupting prominence stretches the arcade field upward, the two legs of the arcade field converge towards the central diffusion region in which the field reconnects. The newly formed plasmoid above the diffusion region after the reconnection erupts outward, while the cusp-shaped field below contracts downward due to the enhanced tension at the cusp. Meanwhile, high energy non-thermal particles produced in the diffusion region or in the newly-reconnected loops can propagate along these shrinking loops down to the chromosphere, and are then decelerated via strong Coulomb collisions with dense plasma there to heat the plasma and produce hard X-ray emission by bremsstrahlung. The heated chromosphere expands upward to fill the loops and radiate in soft X-rays via thermal bremsstrahlung emission.

As to the initial prominence eruption, its triggering mechanism is still unclear so far. Non-equilibrium and MHD instabilities have been proposed to be responsible

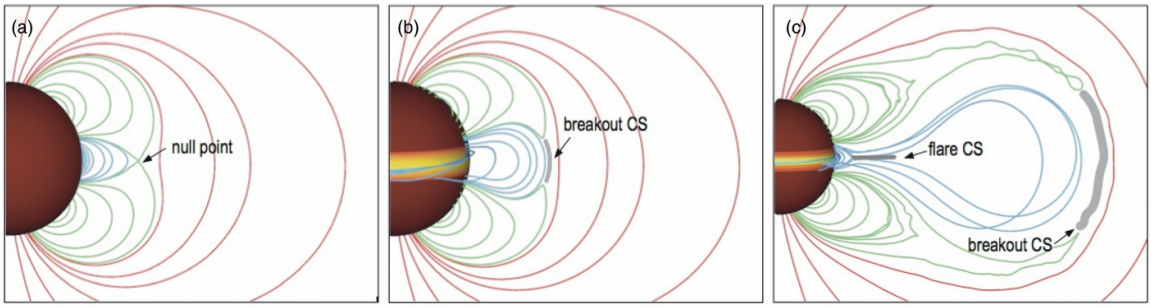

Figure 1.9: The breakout model of solar flares. Taken from Karpen et al. (2012).

for the activation of the eruptive process. As the coronal field evolves, driven by subphotospheric motions or perturbed by nearby events, a critical point may be approached where the field could not be in equilibrium or stable (though it is still in equilibrium). Then a catastrophic eruption of the field to a lower energy state may happen. Kink or torus instabilities are commonly invoked in literature. Kink instability (Hood & Priest 1979) can occur when the involved flux rope suspending the prominence has been twisted so much that it erupts, transferring the twist to the writhe of the axis of the flux rope. Torus instability (Kliem & Török 2006) is an expansion instability (or a lateral kink instability, uniformly distributed over the flux rope). It would happen when the overlying field constraining the flux rope decays significantly, compared to the decrease of the hoop force (a self-repulsive force of a current ring because of the more intense magnetic pressure at the inner edge of the torus) of the flux rope as it expands. These non-equilibrium or instabilities can be induced by processes like flux emergence (newly emerged magnetic field reconnects with pre-existing field), tether-cutting reconnection (sheared arcade field reconnects with each other), shearing or twisting of the footpoints at the photosphere, or reconnection above the flux rope as in the breakout model (Antiochos et al. 1999) shown in Figure 1.9.

1.3 Coronal Implosions

1.3.1 The Implosion Conjecture

Solar eruptions and flares are two main manifestations of magnetic energy release in the corona, possibly triggered by magnetic instabilities or reconnection. The means to track the onset of the instability, the movement of free energy through the

corona, and the location of energy transfer or conversion would significantly assist to understand and predict the conditions leading to a flare or eruption.

The conjecture of "implosion", first proposed by Hudson (2000), may help in this effort. It reads that "during a transient, the coronal field lines must contract in such a way as to reduce $\int_V (B^2/8\pi) dV$" (which is the magnetic energy within the entire coronal volume). It is based on the following three assumptions:

- Assumption A : a flare or CME gets its energy directly from the solar corona.
- Assumption B: gravitation is of no significance.
- Assumption C: low plasma β in the corona ($\beta = p/(B^2/8\pi)$, the ratio of thermal plasma pressure to magnetic pressure).

Assumption A is well accepted in the solar community because the low Alfvén speed in the photosphere cannot account for short flare timescales. Assumption B can be true for most part of the solar corona where plasma density is low, while for some regions containing dense filament material the assumption is not valid (discussed later in detail in Section 3.3.4). Assumption C is reasonable for a large fraction of the solar corona but it can fail for the outer corona where magnetic field strength is reduced significantly and for cusped loops where temperature is high besides low magnetic field strength. For the region that satisfies all the three assumptions, as the equation of motion for the plasma in the corona (Priest 2014) is

$$\rho \frac{d\boldsymbol{v}}{dt} = -\nabla p + \boldsymbol{j} \times \boldsymbol{B} - \rho \boldsymbol{g} \tag{1.1}$$

the assumptions imply that coronal dynamics on large scale is dominated by magnetic Lorentz force. The Lorentz force can be decomposed into two components (Priest 2014)

$$\boldsymbol{j} \times \boldsymbol{B} = \frac{(\boldsymbol{B} \cdot \nabla)\boldsymbol{B}}{\mu} - \nabla(\frac{B^2}{2\mu}) \tag{1.2}$$

the first term on the right hand side is magnetic tension force, and the second one magnetic pressure force. Their components parallel to the magnetic field cancel out with each other, only leaving the components perpendicular to the field. Also Alfvén's frozen flux theorem applies under the condition of magnetic Reynolds number $R_m \gg 1$ ($R_m = \frac{l_0 V_0}{\eta}$, where l_0 and V_0 are the typical plasma length scale and speed, respectively, and η the magnetic diffusivity) in the corona, which means that

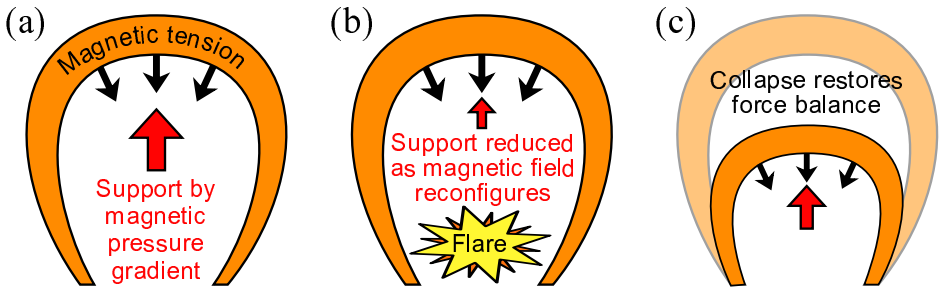

Figure 1.10: Peripheral implosion modeled as a one-loop harmonic oscillator. Taken from Russell et al. (2015).

the magnetic field changes as if it moves with the plasma. Based on these, Russell et al. (2015) illustrated the implosion conjecture in a one-loop system in Figure 1.10. Before the flare or eruption in Figure 1.10(a), the loop is static as the downward magnetic tension force is balanced with the upward magnetic pressure force. In Figure 1.10(b) during a flare or eruption (we emphasise here that the eruption should be sideways relative to the overlying loop in order not to "destroy" it), the magnetic energy is released locally in the flare or removed from the original position via the eruption, then because of the equivalence of magnetic energy and pressure (they are both equal to $\frac{B^2}{2\mu}$), the magnetic pressure underneath is reduced and leaves the magnetic pressure force decreased, thus the overlying loop would contract downward under the net force of magnetic tension force and the reduced magnetic pressure force. With the loop shrinking in Figure 1.10(c), its curvature becomes smaller and reduces the tension force, thus the net force would diminish. Finally the loop would reach a new equilibrium state with a shorter length and the forces balanced.

Hudson (2000) also emphasised that this implosion process should be most pronounced during the impulsive phase when the energy release rate reaches its maximum. The implosion picture seems to conform to logic and intuition, and could be possible in reality, but we should notice that the conjecture is based on the three assumptions, which have not been conclusively confirmed in observation and may be important in future discussion. Regions not meeting these assumptions may not exhibit implosion behaviours. One particular case we will discuss in Chapter 3.

The understanding and study of the implosion idea is still in its infancy, and so far we are not able to fully comprehend it. Later in Section 1.3.4, we will discuss some other branches of implosions. Right now we call the scenario illustrated in

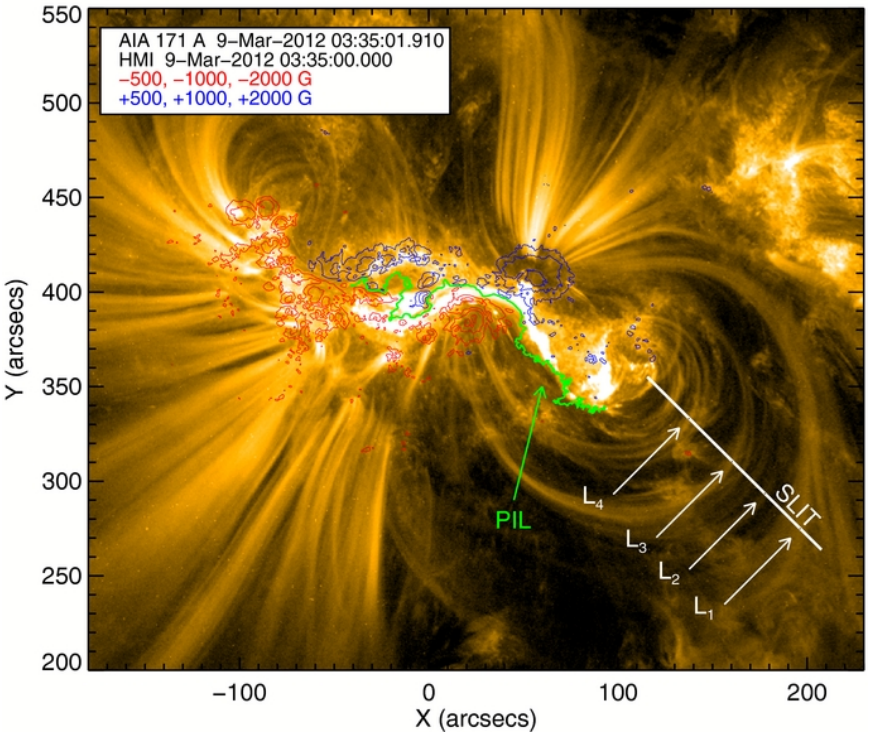

Figure 1.11: The active region in which peripheral implosions are observed in the event SOL2012-03-09T03:53 (M6.4). Taken from Simões et al. (2013).

Figure 1.10 "peripheral implosion", as the peripheral loops implode towards the central energy release site.

1.3.2 Observations of Peripheral Implosions

Though the implosion conjecture was proposed almost two decades ago, only a few implosions in peripheries of ARs are observed, compared to numerous eruptions and flares detected. From 2009 to 2012, Liu and other collaborators reported a series of events showing coronal loop contractions in the extreme ultraviolet (EUV) (Liu & Wang 2009; Liu et al. 2009b; Liu & Wang 2010; Liu et al. 2012a). These events range from GOES class B to X with contraction speeds from tens to hundreds of km/s, happening in the preflare phase, during the impulsive phase or in the gradual phase. It seems that implosion is possible in all flare classes and during the entire flare process. Some authors observed loop contractions accompanying erupting filaments or bubbles (Liu & Wang 2009; Liu et al. 2012a; Simões et al. 2013; Yan et al. 2013; Shen et al. 2014; Kushwaha et al. 2015). Simões et al. (2013) in an M6.4 flare

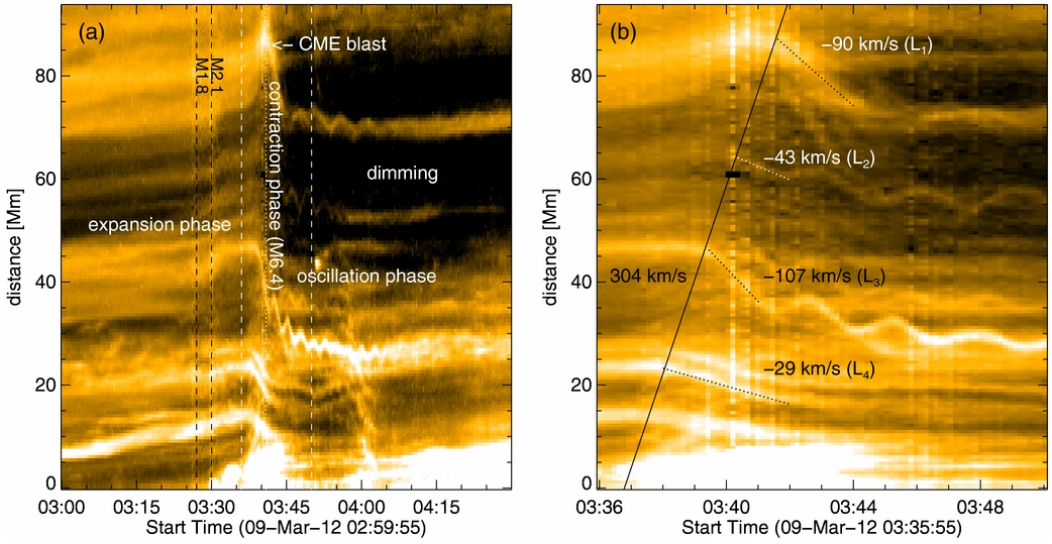

Figure 1.12: Peripheral implosion dynamics for the event SOL2012-03-09T03:53 (M6.4). (a) Timeslices for the slit in Figure 1.11. (b) Zoomed in for the interval between the two white dashed lines in (a) during the impulsive phase. Taken from Simões et al. (2013).

found that the loop contraction speed correlates well with the hard X-ray (HXR) and microwave (MW) radiation, with faster contraction corresponding to more intense radiation.

In some of the events above, dramatic oscillations were noticed during or after the loop contractions (Liu & Wang 2010; Gosain 2012; Liu et al. 2012a; Sun et al. 2012; Simões et al. 2013). One good example is shown in Figures 1.11 and 1.12. Russell et al. (2015) considered a one-loop system as a harmonic oscillator, showing that the contracting and oscillating behaviours can be reproduced by the change in loop equilibrium position due to magnetic energy release underneath, in agreement with the implosion conjecture. Pascoe et al. (2017) included a displacement term for the changing equilibrium position from Russell et al. (2015) for coronal seismology analysis, and only the fundamental kink mode exists associated with the loop contraction in Simões et al. (2013). Liu & Wang (2010) suggested that the interaction between the contracting loops and surrounding ones may also make them oscillate. The model of an isolated simple harmonic oscillator in Russell et al. (2015) cannot properly describe the dynamics of a continuum medium, where many magnetic strands will interact with each other if not in phase, so a full magnetohydrodynamic (MHD)

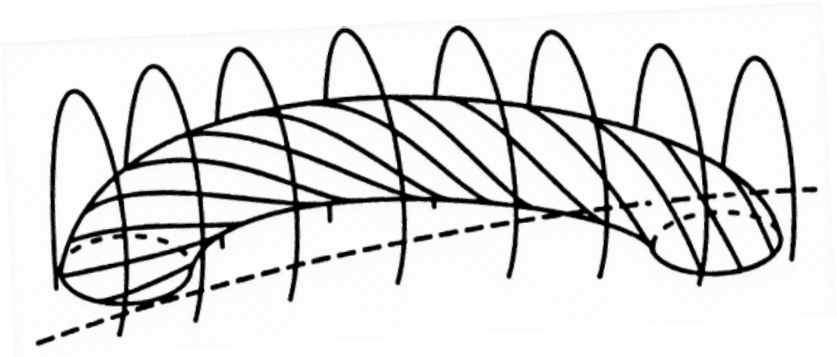

Figure 1.13: A twisted flux rope anchored below an overlying arcade. Taken from Sturrock et al. (2001).

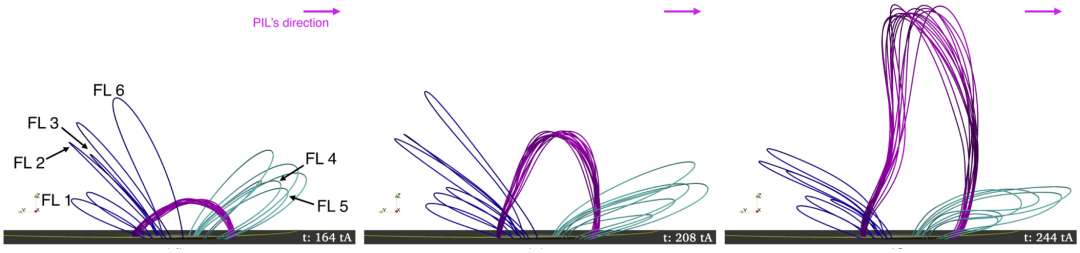

Figure 1.14: Peripheral implosions during the central flux rope eruption in the MHD simulation of Zuccarello et al. (2017).

treatment may be needed for a more accurate description of the dynamics observed.

1.3.3 Peripheral Implosions in Simulations

The implosion conjecture links flare energy release with field contraction, and is apparently at odds with many flares in which eruptions are seen. The Aly-Sturrock hypothesis (Aly 1984, 1991; Sturrock 1991), which states that the energy of any simply-connected and closed force-free field is less than the energy of the corresponding completely opened field with the same vertical flux at its boundary, implies that energy must be added to erupt the field, rather than being liberated by the process, as is required to explain the flare. One solution is the partial opening of the field in a three-dimensional (3D) configuration. Magnetohydrodynamic (MHD) simulations utilising the 3D metastable eruption model (Sturrock et al. 2001), which has a twisted flux rope anchored below a magnetic arcade (Figure 1.13), have shown that during the flux rope eruption, some unopened overlying arcade loops in the

periphery could finally contract to a shorter length compared to their initial states (Roussev et al. 2003; Aulanier et al. 2005; Gibson & Fan 2006; Fan & Gibson 2007; Rachmeler et al. 2009). A good example can be seen in Figure 1.14: as the central flux rope erupts upward, some of the peripheral unopened loops on both sides could contract towards the erupting structure, but depending on the location of the arcade field, the field would (i) expand, incline and contract (e.g., FL 2 and FL 6), or (ii) incline and contract (e.g., FL 3). These simulations are the manifestations of peripheral implosions accompanying the central energy release manifested by the flux rope eruption.

Sarkar et al. (2017) recently carried out the first simulation focused on implosions, and found that oscillations of both kink and sausage modes can exist when the loops contract, and that loops in different plasma β regimes may exhibit different dynamic behaviours.

1.3.4 Generalisation of the Implosion Idea

The establishment of scientific concepts is difficult, and its evolution is slow and gradual, so is the implosion idea. First, we need to understand the spirit of the implosion idea, that is, when an energy-releasing event happens in the corona, there should be an implosion behaviour which makes the field more compact around the energy release site.

Then, we argue that implosion does not necessarily only mean contraction of field lines in the peripheral region as in Figures 1.15(a) and (b), which are separately driven by underlying magnetic energy transfer in the eruption and magnetic energy dissipation in the flare. We can imagine that in principle when the energy release site is local and high in the corona, the surrounding plasma and entrained field would converge toward this region where magnetic pressure correspondingly reduces; specifically, overlying loops would contract as in Figures 1.15(a) and (b); underlying loops, if they exist, may show expansion up toward the energy release site; and lateral field would incline toward the region. However, in practice we need to consider realistic magnetic topologies and processes. For example, in the standard "CSHKP" model of two ribbon flares shown in Figure 1.15(c), if the energy is liberated in the central diffusion region or current sheet, the inflow toward this site can be regarded as the lateral field inclining, but because of the magnetic tension of the newly

reconnected field upward and downward from the diffusion region, the loops there would instead expand outward and contract downward the solar surface, respectively. Similar processes also happen in the break-out model (Figure 1.9(b)), but the inflow there is vertical (the loops below the reconnection site thus show expansion), and the contraction of the newly reconnected field lines (called dipolarisation) is transverse near the diffusion region. Thus, in these reconnection-related energy-releasing events, the inflow toward the diffusion region is a type of implosion based on the spirit described above, and is inclining of the loops, not necessarily contraction of the field lines. We can call this kind of implosion "inflow-type implosion". The key difference between the inflow-type implosion and the peripheral ones is that the imploding field in the former type will participate in reconnection in the current sheet or diffusion region. We also need to mention that even if the magnetic energy is released in the newly reconnected loops when they contract downward as argued by some authors (e.g., Fletcher & Hudson 2008; Veronig et al. 2006) instead of exactly in the diffusion region, the inflow can still be taken as a kind of implosion because in this scenario it is just like a peripheral implosion as the newly reconnected loops transferring magnetic energy out of the diffusion region when they contract (Figure 1.15(c)) would create a magnetic sink (low magnetic energy and pressure) around the current sheet. This is shown in Figures 1.16(e) and (f) from Zuccarello et al. (2017), where the blue dotted lines indicate that magnetic pressure around the diffusion region is significantly lower than that in the surrounding area.

Let us consider the dipolarisation of the newly reconnected loops in Figure 1.15(d). Could we regard this motion as an implosion? We ask this because contraction of field lines generally indicates reduction of magnetic energy. In the original paper of Hudson (2000), he argued that increasing magnetic energy in the solar corona usually corresponds to expansion or inflation of the magnetic field (e.g., see Dahlburg et al. 1991 and Sturrock et al. 1994 in simulation of twisting up footpoints of magnetic field lines), thus the opposite process, releasing the coronal magnetic energy, may lead to magnetic field contraction or deflation. Also the Aly-Sturrock hypothesis (Aly 1984, 1991; Sturrock 1991) implies that energy should be added to open the field, thus more compact field is of lower energy state. Moreover, Ji et al. (2007) demonstrated that unshearing motion of the field line which makes the field more potential and thus releases magnetic energy would lead the field to shrink. The energy released in the shrinkage of newly reconnected field lines could heat or accelerate particles

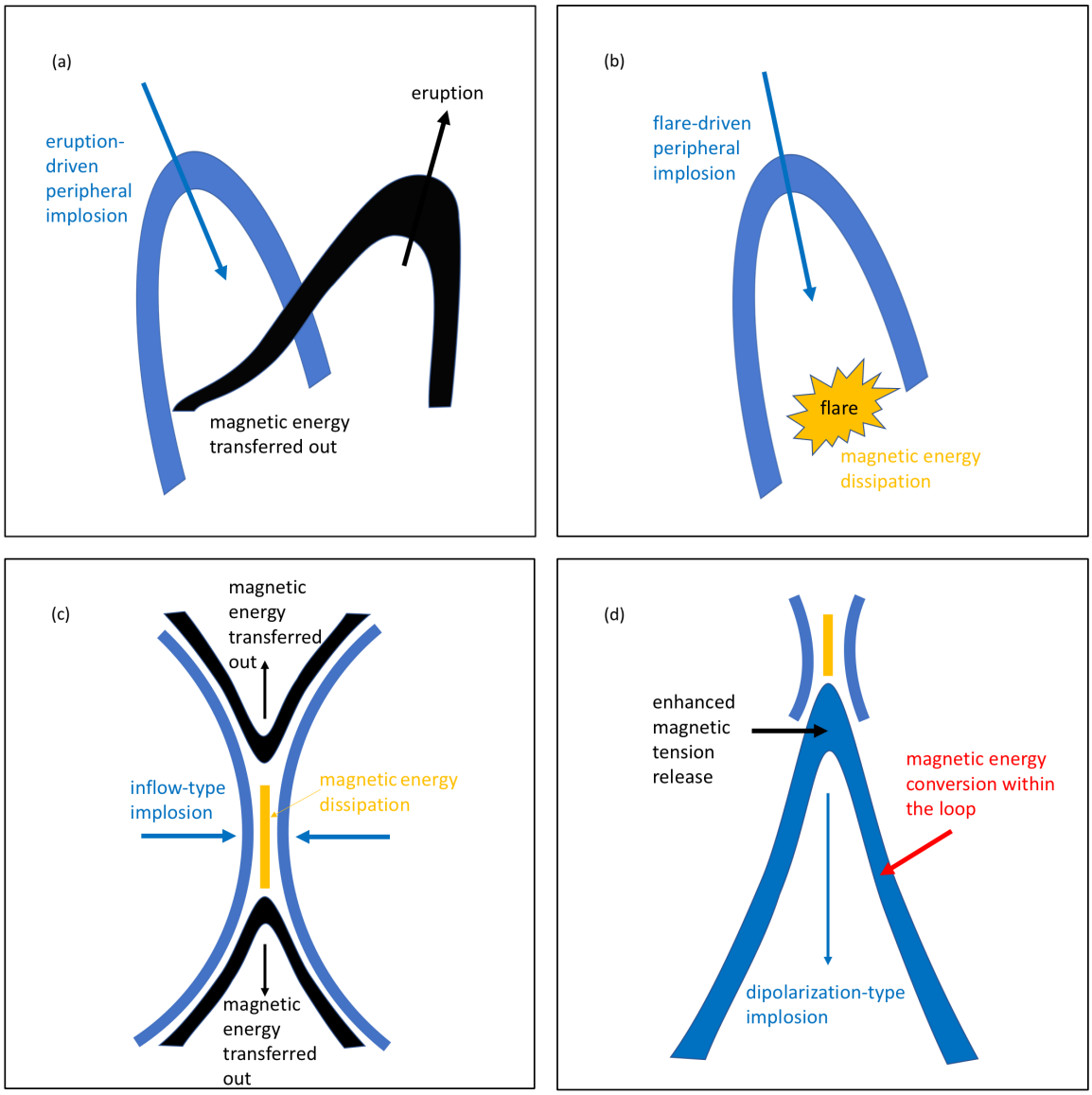

Figure 1.15: Different implosion types identified. (a) Eruption-driven peripheral implosion. (b) Flare-driven peripheral implosion. (c) Inflow-type implosion. (d) Dipolarization-type implosion.

within via, e.g., a collapsing magnetic trap (Veronig et al. 2006), shocks (Longcope et al. 2009), or Alfvén waves (Fletcher & Hudson 2008). Thus, during this kind of contraction of field lines, the contracting field itself releases energy, which is unlike the peripheral and inflow-type implosions where the contraction or inclining of surrounding field lines is caused by the central energy liberation. In this case, the region where magnetic energy liberates shrinks itself, thus we call this motion

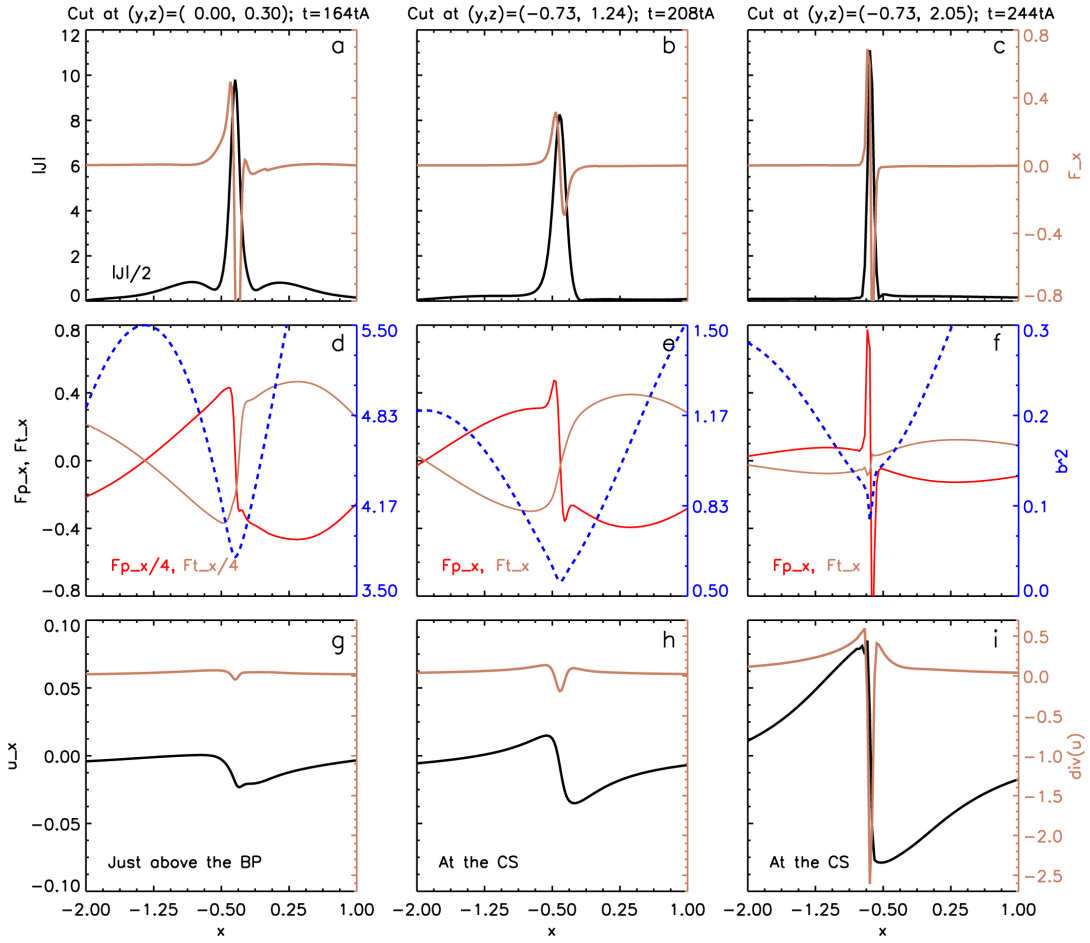

Figure 1.16: In (e) and (f), the blue dashed lines show the magnetic energy/pressure ($\propto B^2$) distribution across the current sheet in the 3D MHD simulation of Zuccarello et al. (2017) at times $t = 208$ and 244 t_A.

of the region "core implosion". In principle, we can still understand it based on the spirit of the implosion idea. Imagine that the magnetic energy is released in a substantial volume simultaneously, rather than in a local space as discussed above. The volume is the core for providing energy for the event, and as the energy and corresponding magnetic pressure decrease there, surrounding plasma and entrained field would collapse inward and compress the core region, leading to a core implosion. However, in the specific dipolarization case, the core which occupies a volume is the shrinking loops, and the shrinkage is mainly caused by the strong magnetic tension force of newly reconnected field lines at the cusp, rather than reduced magnetic pressure invoked as an argument in the original implosion paper of Hudson (2000)

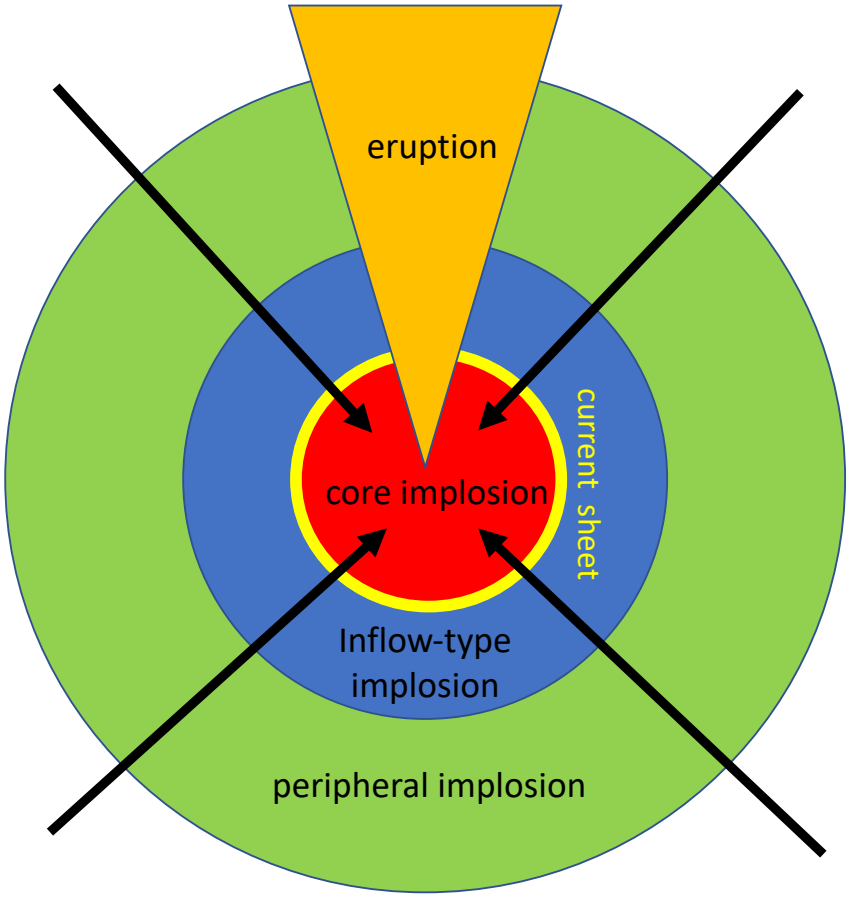

Figure 1.17: The suggested united picture of the implosion idea.

(which may also play a role to make the dipolarising field more compact). In other words, liberation of magnetic energy does not only mean reduction of magnetic pressure in the core, but also decrease of magnetic tension of the core in some cases, which can lead to contraction of the associated field lines if their footpoints are line-tied at the photosphere. Finally, if we want to further generalise the concept of implosion, dipolarisation of newly reconnected field lines can be regarded as one of the core implosion types, where the energy-releasing field shrinks itself as a result of gradually releasing magnetic tension. We can call it "dipolarization-type implosion".

Figure 1.17 summarizes our unification of the different implosion types, with the core implosion, the inflow-type implosion and the peripheral implosion happening in a hierarchy structure. The process can/cannot have an acompanying eruption because both eruptive or non-eruptive flares have been observed so far. The core

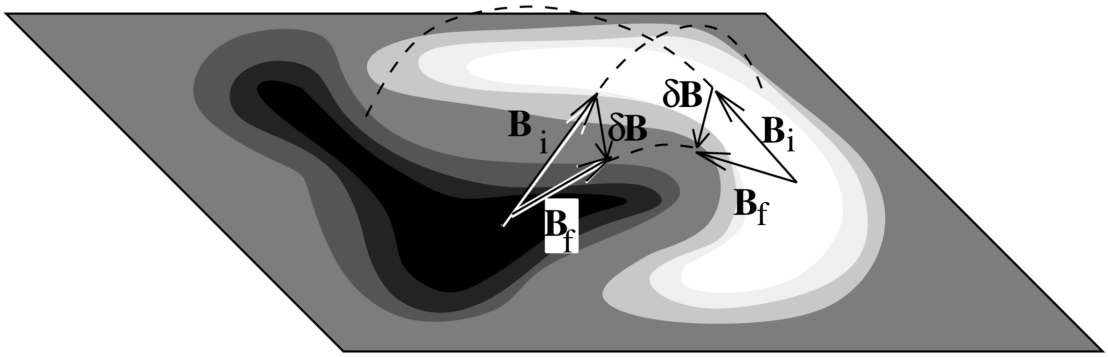

Figure 1.18: Field lines become more horizontal near the PIL after reconnection. $\mathbf{B}_i$ is the initial field vector, $\mathbf{B}_f$ the final field vector, and $\delta\mathbf{B}$ the change of the field vector. Taken from Hudson et al. (2008).

implosion is located in the center as the energy-releasing core field shrinks itself, which can be a dipolarization type or other types yet to be discovered or identified for specific magnetic topology and process. The inflow-type implosion and the peripheral one both converge towards the core region because of the reduction of magnetic pressure in the core, but the former one would convect the field into the current sheet where reconnection occurs to generate the shrinking core field. The scenario in Figure 1.17 can be imagined as a star formation process where the surrounding molecular cloud collapses to form the central star. The generalization of the implosion idea makes us unite and explain different phenomena in the dynamic solar corona using only one principle, that is, magnetic energy release would make magnetic field more compact. It conforms to the art of simplicity of science.

1.3.5 Implosions as a Possible Driver of Helioseismic Waves

On the basis of the implosion conjecture, Hudson et al. (2008) further predict that the photospheric magnetic field should become more horizontal because of field line contraction when the coronal magnetic field restructuring disturbance transmits to the photosphere (Emslie & Sturrock 1982), which would produce a downward Lorentz force and give rise to a seismic wave. This can be a valuable application of the implosion idea. To the first order, the force per unit area (Fisher et al. 2012) can be expressed as,

$$\delta f_z = (B_z \delta B_z - B_x \delta B_x - B_y \delta B_y)/4\pi \tag{1.3}$$

where δ means the change of that magnetic field component at the photosphere. However, we need to point out here that the speculation of more horizontal field after implosions is not necessarily true, which can be clearly seen in Figure 1.10. It depends on the specific magnetic dynamic processes. For example, the dipolarisation-type implosion illustrated in Figure 1.18 near the PIL would generate more horizontal field, but the peripheral implosion in Figure 1.10 which could happen far from the PIL may make the field more vertical if the field does not contract too much. Thus different areas at the photosphere may experience forces with different directions and also magnitudes, leading to a complex mix of seismic waves.

A longitudinal field decrease or horizontal field enhancement near the polarity inversion line in the photospheric magnetograms has been detected during many events, especially eruptive flares (Sudol & Harvey 2005; Petrie & Sudol 2010; Wang & Liu 2010; Gosain 2012; Petrie 2012; Sun et al. 2012, 2017). The phenomenon is often explained by the authors exploiting the prediction above. However, interestingly, the non-eruptive X3.1 flare in the famous active region 12192 did not show significant changes in its photospheric horizontal field (Sun et al. 2015b; Jiang et al. 2016b).

1.4 Observational Instruments and Analysis Methods

1.4.1 Solar Dynamics Observatory

The *Solar Dynamics Observatory*, abbreviated SDO (Figure 1.19), launched to a geosynchronous orbit on 2010 February 11, is part of the NASA's *Living With a Star* (LWS) Program (Pesnell et al. 2012). Its main goal is to help us understand solar activity and its influences on space weather that impact on Earth's life and technological systems. It has three instruments on board, the *Atmospheric Imaging Assembly* (AIA; Lemen et al. 2012), *Extreme Ultraviolet Variability Experiment* (EVE; Woods et al. 2012), and *Helioseismic and Magnetic Imager* (HMI; Schou et al. 2012). Images from AIA and magnetic field data obtained by HMI are used in this thesis.

AIA consists of four telescopes to record 4096×4096 images with every pixel corresponding to $0.6''$, thus in total having a field of view $41' \times 41'$. It has a two-pixel resolution $\sim 1.5''$, and a cadence 12 s with an exposure time 0.5 – 3 seconds. The Sun can be observed by AIA in ten wavebands, including seven in EUV (94, 131, 171, 193, 211, 304, and 335 Å), two in UV (1600 and 1700 Å), and one visible (4500 Å). 94 Å

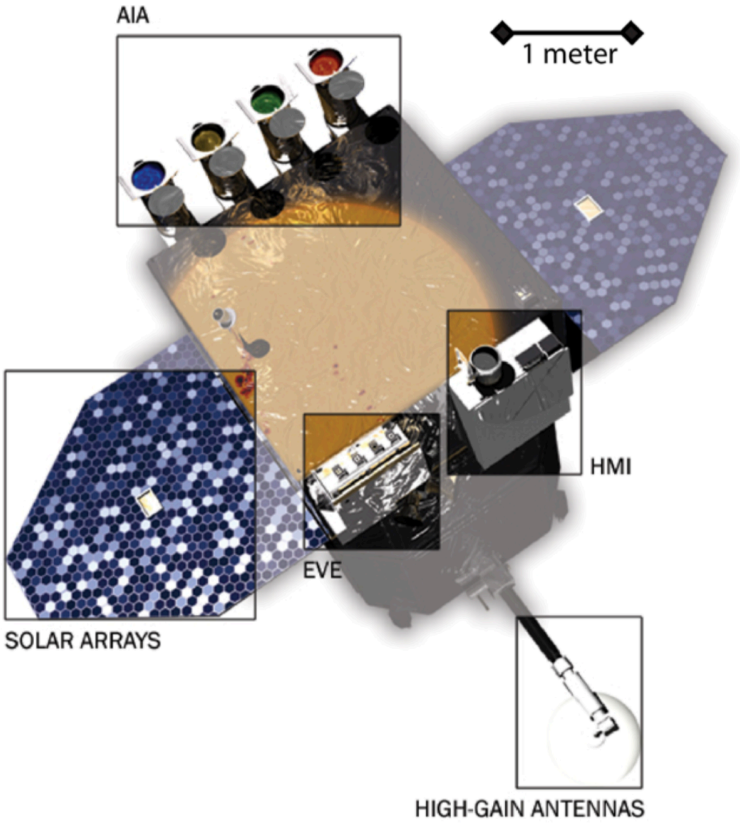

Figure 1.19: The SDO and its onboard instruments AIA, EVE, and HMI. Taken from Pesnell et al. (2012).

is contributed by the ion Fe XVIII at a characteristic temperature ~ 6.3 MK; 131 Å by both Fe VIII and Fe XXI at ~ 0.4 and ~ 10 MK separately; 171 Å by Fe IX at ~ 0.6 MK; 193 Å by both Fe XII and Fe XXIV at ~ 1.6 and ~ 20 MK separately; 211 Å by Fe XIV at ~ 2.0 MK; 304 Å by He II at ~ 50000 K; 335 Å by Fe XVI at ~ 2.5 MK; 1600 Å by both C IV and continuum at ~ 0.1 MK; both 1700 and 4500 Å by continuum at ~ 5000 K. The detailed temperature response functions for six EUV filters (94, 131, 171, 193, 211, and 335 Å) can be seen in Figure 1.20. These six EUV passbands are mainly responsible for high temperature corona observations, while 304 Å for chromosphere, and 1600, 1700 and 4500 together for photosphere. The transition region between chromosphere and corona can be investigated through 131, 171, 304 and 1600 Å.

HMI is designed to study photospheric oscillations and magnetic field, and can provide Dopplergrams, continuum intensity, longitudinal and vector magnetic field at the solar surface. The magnetic field data are employed for context or coronal

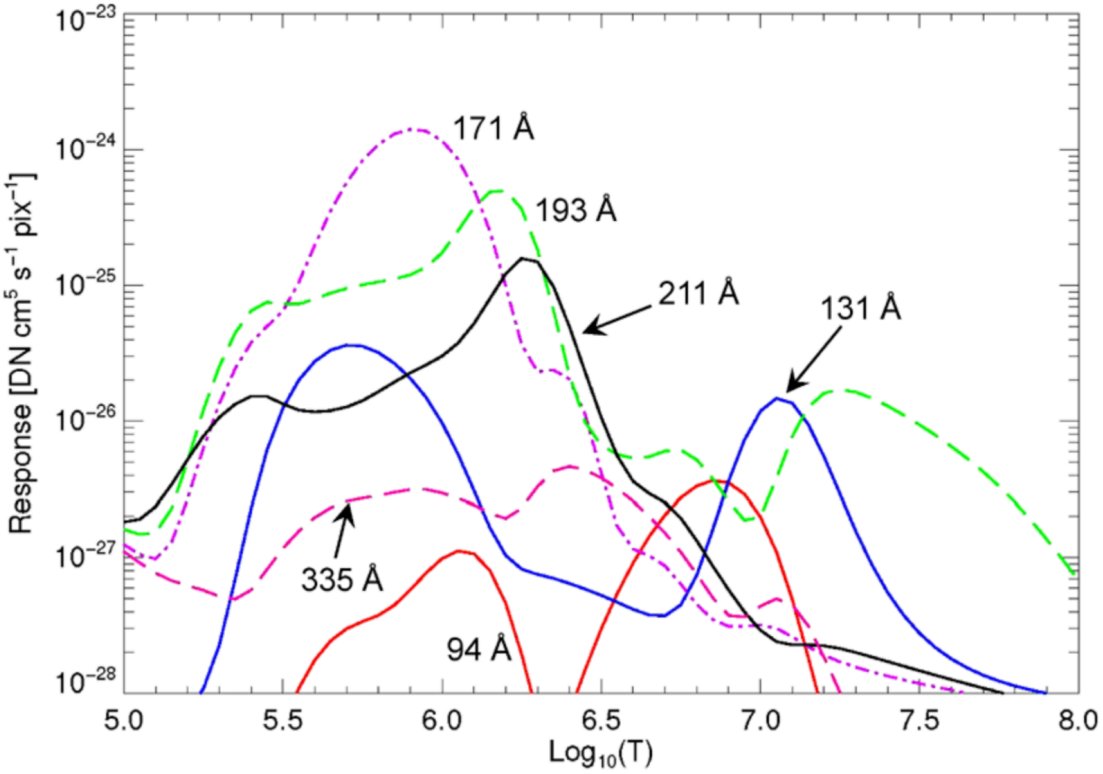

Figure 1.20: AIA temperature response functions for six EUV passbands. Taken from Boerner et al. (2012).

field modelling in this thesis. Similar to AIA, HMI also produces 4096×4096 images, but has 1″ spatial resolution with 0.5″ per pixel. For line-of-sight magnetograms, the temporal cadence is 45 s, while the vector field is generated every 90 or 135 s but ordinarily averaged in 12 min in order to reduce noise. The instrument observes the Sun at six wavelengths across the Fe I 6173 Å absorption line, and records Stokes parameters, which are then transformed to vector magnetograms through a Milne-Eddington inversion code, the Very Fast Inversion of the Stokes Vector (VFISV; Borrero et al. 2011). As the direction of the transverse component of the inverted field cannot be determined by the Stokes parameters, an improved version of the "Minimum Energy" method is then applied, which minimizes $\sum |\nabla \cdot \boldsymbol{B}|^2 + |\boldsymbol{J}|^2$ where $\boldsymbol{J}$ is the total current density (Metcalf 1994; Metcalf et al. 2006; Leka et al. 2009).

1.4.2 Reuven Ramaty High Energy Solar Spectroscopic Imager

The Reuven Ramaty High Energy Solar Spectroscopic Imager (RHESSI; Lin et al. 2002) is a Fourier-transform imaging telescope using modulated signals through nine rotating collimators, each of which consists of a pair of separated grids with equally-spaced opaque slats and transparent slits for X-rays. Launched on 2002 February 5, it is designed to investigate particle acceleration and energy release processes in solar flares. It observes the Sun from 3 keV to 17 MeV, with energy resolution $\lesssim 1$ keV at 3 keV, increasing to ~ 5 keV at 5 MeV. The field of view is around 1°, covering the full solar disk, with a high spatial resolution for X-ray observations, i.e., 2.3″ from 3 keV to 100 keV, then 7″ to 400 keV, and 36″ to 15 MeV. A high temporal resolution is also achieved at 2 s. In the thesis we mainly use the count rate recorded by RHESSI for context and its imaging capability to locate X-ray sources, though it can provide very valuable spectroscopic information.

To reconstruct RHESSI images, various algorithms have been created, e.g., Clean (Högbom 1974), Maximum Entropy Methods (Sato et al. 1999), Forward-Fitting (Aschwanden et al. 2002; Schmahl et al. 2007), and Pixon (Puetter 1995; Metcalf et al. 1996; Alexander & Metcalf 1997). An introduction to all of these imaging methods can be found in Hurford et al. (2002). Here we only briefly describe the Clean method which is employed in this thesis. The Clean algorithm assumes that the image is constructed by a convolution of point sources with instrument Point Spread Functions (PSFs). It uses the basic back-projection map as the initiation, and iteratively finds the highest flux and subtracts the PSF normalized to a proportion of the flux there, until a certain number of iterations is reached, or until the negative peak is larger than the positive one. The final image is the normalized flux convolved with a Clean PSF (which is a gaussian profile whose FWHM is called the Clean beam width, indicating the effective resolution of the corresponding collimator), adding the residual map subtracted as noise.

1.4.3 Solar TErrestrial RElations Observatory

Solar TErrestrial RElations Observatory (STEREO) was launched on 2006 October 25, comprised of two nearly identical spacecraft circling around the Sun near the Earth orbit. One is traveling ahead of the Earth, called STEREO-A, and the other, named STEREO-B, trailing behind the Earth, which together provides stereoscopic

observations of the Sun. The instrument, Sun-Earth-Connection Coronal and Heliospheric Investigation (SECCHI; Howard et al. 2008), onboard both STEREO-A and -B is designed to study the evolution of CMEs from the solar surface to the Earth orbit. It consists of five telescopes, the Extreme Ultraviolet Imager (EUVI), the Inner Coronagraph (COR1), the Outer Coronagraph (COR2), and two Heliospheric Imager (HI1 and HI2). EUVI, which is employed in this thesis for a stereoscopic view of solar events, is responsible for observing the chromosphere and low corona out to 1.7 $R_\odot$. It is a normal incidence telescope, and records 2048×2048 pixel images with 1.6″ per pixel. It observes the Sun in four EUV emission lines, i.e., He II 304 Å, Fe IX 171 Å, Fe XII 195 Å, and Fe XV 284 Å, covering 0.1 – 20 MK temperature response, with variable cadences up to 2.5 min.

1.4.4 Hinode

Launched on 2006 September 22, the Hinode mission is designed to study energy transfer from solar photosphere through chromosphere to corona, and energy release responsible for flares and CMEs (Kosugi et al. 2007). It comprises three instruments, the EUV Imaging Spectrometer (EIS; Culhane et al. 2007), the Solar Optical Telescope (SOT; Suematsu et al. 2008; Tsuneta et al. 2008), and the X-Ray Telescope (XRT; Golub et al. 2007). EIS, used in the thesis, has a FOV 360″ × 512″, with a spatial resolution 2″ (1″ per pixel). It can record emission lines in the wavelength ranges 170 – 210 Å and 250 – 290 Å, with a spectral resolution ∼ 60 mÅ (Brown et al. 2008), covering the temperature range $5 \times 10^4 - 2 \times 10^7$ K, for upper transition region and corona observations. Two slits (1″ and 2″) are employed for spectroscopy, and two slots (40″ and 266″) for imaging. The slits can perform in two modes, rastering/scanning, or sit-and-stare/fixed. The rastering mode scans across a region, offset in an amount of time (can be adjusted to less than 1 s) by a step (0.123″ at a minimum), and taking successive exposures (< 1 s – ∼ 10 s for each). The exposure time for monochromatic imaging using the slots can be 3 – 10 s.

1.4.5 Coronal Magnetic Field Extrapolation

The coronal magnetic field is not so readily obtained as for the photophere via Zeeman splitting. For the corona, the higher temperature broadening spectral lines, the weaker magnetic field narrowing the splitting, and the lower line intensity reducing

the signal-to-noise ratio would make the line splitting difficult to distinguish. Moreover, the non-local thermodynamic equilibrium and the optically thin condition in the corona add more difficulties in the interpretation of spectral line observations (Guo et al. 2017). To study coronal magnetic field, routinely observed photospheric magnetograms are used to extrapolate into the corona. In magnetohydrostatic conditions with Lorentz force dominating plasma pressure gradient and gravity, the plasma in the corona experience no force (force-free) with

$$\boldsymbol{j} \times \boldsymbol{B} = 0 \tag{1.4}$$

from Equation 1.1. Using Ampère's Law

$$\boldsymbol{j} = \nabla \times \boldsymbol{B}/\mu \tag{1.5}$$

we obtain

$$(\nabla \times \boldsymbol{B}) \times \boldsymbol{B} = 0 \tag{1.6}$$

or

$$\nabla \times \boldsymbol{B} = \alpha \boldsymbol{B} \tag{1.7}$$

where α is a scalar function of position. Then take the divergence of Equation 1.7 and use the law that magnetic monopoles do not exist

$$\nabla \cdot \boldsymbol{B} = 0 \tag{1.8}$$

it follows that

$$(\boldsymbol{B} \cdot \nabla)\alpha = 0 \tag{1.9}$$

which implies that α is constant along magnetic field lines. Equations 1.7 and 1.9 set a system of partial differential equations that a force-free field has to satisfy. When $\alpha = 0$, it is called a potential field, with no current. If α is constant in the entire space, the set of equations is linear, and the field is called linear force-free field. In the most general case that α varies in space, which is expected to conform more to realistic coronal magnetic field, the field is referred to as nonlinear force-free field (NLFFF) because the set of equations is nonlinear. Their analytic solutions have not been found in general cases.

Numerical methods are then developed to construct the force-free magnetic field in the corona, which exploit photospheric magnetogram observations as the bottom boundary. They include the vertical integration method (Nakagawa 1974;

Demoulin & Priest 1992; Amari et al. 1998), Grad-Rubin method (Grad & Rubin 1958; Sakurai 1981; Wheatland 2004), MHD relaxation method (Mikic & McClymont 1994; Roumeliotis 1996; Wiegelmann & Neukirch 2003), and optimization method (Wheatland et al. 2000; Wiegelmann 2004; Wiegelmann et al. 2006; Wiegelmann & Inhester 2010). The optimization method will be used in this thesis and discussed as below. A functional L is defined as,

$$L = \int_V w(x,y,z)\, B^2\, (\Omega_a^2 + \Omega_b^2)\, d^3x \tag{1.10}$$

with

$$\boldsymbol{\Omega_a} = B^{-2}\, [(\nabla \times \boldsymbol{B}) \times \boldsymbol{B}] \tag{1.11}$$

$$\boldsymbol{\Omega_b} = B^{-2}\, [(\nabla \cdot \boldsymbol{B})\, \boldsymbol{B}] \tag{1.12}$$

where w (chosen to be > 0) is a weighting function, and the integral covers the volume of interest. If L equals to zero, the force-free and divergence-free conditions in Equations 1.6 and 1.8 can be satisfied simultaneously. Thus numerically, to obtain a force-free field $\boldsymbol{B}$ is equivalent to finding a minimum of L. To achieve this purpose, take the derivative of L with respect to an iteration step t,

$$\frac{1}{2}\frac{dL}{dt} = -\int_V \frac{\partial \boldsymbol{B}}{\partial t} \cdot \tilde{\boldsymbol{F}}\, d^3x - \int_S \frac{\partial \boldsymbol{B}}{\partial t} \cdot \tilde{\boldsymbol{G}}\, d^2x \tag{1.13}$$

where

$$\tilde{\boldsymbol{F}} = w\boldsymbol{F} + (\boldsymbol{\Omega_a} \times \boldsymbol{B}) \times \nabla w + (\boldsymbol{\Omega_b} \cdot \boldsymbol{B})\, \nabla w \tag{1.14}$$

$$\tilde{\boldsymbol{G}} = w\boldsymbol{G} \tag{1.15}$$

$$\boldsymbol{F} = \nabla \times (\boldsymbol{\Omega_a} \times \boldsymbol{B}) - \boldsymbol{\Omega_a} \times (\nabla \times \boldsymbol{B}) + \nabla(\boldsymbol{\Omega_b} \cdot \boldsymbol{B}) - \boldsymbol{\Omega_b}(\nabla \cdot \boldsymbol{B}) + (\Omega_a^2 + \Omega_b^2)\boldsymbol{B} \tag{1.16}$$

$$\boldsymbol{G} = \hat{\boldsymbol{n}} \times (\boldsymbol{\Omega_a} \times \boldsymbol{B}) - \hat{\boldsymbol{n}}(\boldsymbol{\Omega_b} \cdot \boldsymbol{B}) \tag{1.17}$$

where $\hat{\boldsymbol{n}}$ is the inward unit vector on the surface of the volume. If within the computational box the magnetic field is chosen to change with the iteration step as,

$$\frac{\partial \boldsymbol{B}}{\partial t} = \mu \tilde{\boldsymbol{F}} \tag{1.18}$$

with $\mu > 0$, and $\boldsymbol{B}$ is fixed at the boundaries, it follows that $\frac{dL}{dt} < 0$ from Equation 1.13. It indicates that L will decrease monotonically, finally its minimum and thus a force-free field can be found.

Before implementing numerical NLFFF extrapolations, we also need to first preprocess the vector magnetograms observed at the photosphere. The photospheric

magnetic field is not necessarily force-free, because the plasma β there is close to one, implying that apart from Lorentz force the plasma pressure takes a non-negligible role in controlling the plasma flow. The forced photospheric field thus needs to be driven to mimic the force-free chromospheric one. The optimization method of Wiegelmann et al. (2006) for preprocessing is used in this thesis. It is to minimize the functional,

$$L = \mu_1 L_1 + \mu_2 L_2 + \mu_3 L_3 + \mu_4 L_4 \tag{1.19}$$

where

$$L_1 = (\sum_p B_x B_z)^2 + (\sum_p B_y B_z)^2 + (\sum_p B_z^2 - B_x^2 - B_y^2)^2 \tag{1.20}$$

$$L_2 = (\sum_p x(B_z^2 - B_x^2 - B_y^2))^2 + (\sum_p y(B_z^2 - B_x^2 - B_y^2))^2 + (\sum_p yB_xB_z - xB_yB_z)^2 \tag{1.21}$$

$$L_3 = \sum_p (B_x - B_{xobs})^2 + \sum_p (B_y - B_{yobs})^2 + \sum_p (B_z - B_{zobs})^2 \tag{1.22}$$

$$L_4 = \sum_p (\triangle B_x)^2 + (\triangle B_y)^2 + (\triangle B_z)^2 \tag{1.23}$$

μ_n are weighting functions, which are chosen to be $\mu_1 = \mu_2 = 1$, $\mu_3 = 0.001$, and $\mu_4 = 0.01$ for HMI data (Wiegelmann et al. 2012). p indicates grid nodes at the bottom boundary. L_1 represents the force-balance conditon, L_2 the torque-free condition, L_3 the agreement between the processed data and the observational one, and L_4 the smoothness. The iteration is conducted by the Newton scheme,

$$(B_x)_q \leftarrow (B_x)_q - \mu \frac{dL}{d(B_x)_q} \tag{1.24}$$

$$(B_y)_q \leftarrow (B_y)_q - \mu \frac{dL}{d(B_y)_q} \tag{1.25}$$

$$(B_z)_q \leftarrow (B_z)_q - \mu \frac{dL}{d(B_z)_q} \tag{1.26}$$

with $\mu > 0$, which can realize the monotonic decrease in L and achieve its minimum. The preprocessing and extrapolation codes for the optimization method are written and distributed by Dr. Wiegelmann.

The NLFFF extrapolation is particularly suited for investigating magnetic field of active regions in the low corona with strong currents. In Chapter 4, we also use the potential-field source-surface (PFSS) model (Schatten et al. 1969; Altschuler & Newkirk 1969) to reconstruct the more potential-like coronal field in large (or global)

scale. It assumes a spherical "source surface" located at 2.5 $R_\odot$ with field there in the radial direction driven by solar wind propagating ourward. By definition the potential field has no current, then it follows that from Equation 1.28,

$$\nabla \times \boldsymbol{B} = 0 \,. \tag{1.27}$$

Thus the magnetic field can be represented by a scalar potential,

$$\boldsymbol{B} = -\nabla \phi \,. \tag{1.28}$$

Substitute it into the divergence-free Equation 1.8, we get the Laplace equation,

$$\nabla^2 \phi = 0 \,. \tag{1.29}$$

The solution to the Laplace equation can be expanded into spherical harmonics,

$$\phi(r,\theta,\varphi) = R_\odot \sum_{l=0}^{N} \sum_{m=0}^{l} f_l(r) P_l^m(\theta)(g_l^m \cos m\varphi + h_l^m \sin m\varphi) \tag{1.30}$$

where

$$f_l(r) = \frac{(r_w/r)^{l+1} - (r/r_w)^l}{(r_w/R_\odot)^{l+1} - (R_\odot/r_w)^l} \tag{1.31}$$

P_l^m the Legendre polynomials, and $r_w = 2.5 R_\odot$. The function then satisfies the radial-field constraint at the upper boundary. g_l^m and h_l^m can be determined by numerical fitting up to a specified order N to comply with the photospheric magnetogram at the bottom boundary,

$$-\boldsymbol{l} \cdot \nabla \phi = B_l(\theta,\varphi) \tag{1.32}$$

where $\boldsymbol{l}$ is the unit vector in the line-of-sight direction. The description of the software package for the PFSS model can be found at the link http://www.lmsal.com/~derosa/pfsspack/.

1.4.6 Differential Emission Measure

Differential emission measure (DEM) is a description of plasma distribution over temperature. For a column of plasma of a unit base area, it is defined as $\xi(T) = n_e^2 \frac{dz}{dT}$, where n_e is the electron density at temperature T, and z the column length for the plasma at this temperature. The definition of DEM can be derived as follows (Aschwanden 2005). The emission coefficient for an atomic spectral line of wavelength

λ_{ij} (corresponding frequency ν_{ij}) produced via a jump of an electron from a higher energy level j to a lower one i is,

$$\epsilon_{ji} = \frac{h\nu_{ij}}{4\pi} N_j(X^{+m}) A_{ji} \ \ (\mathrm{erg\ s^{-1}\ cm^{-3}\ ster^{-1}}) \tag{1.33}$$

where $N_j(X^{+m})$ is the number density of the ion X^{+m} at the higher energy level j, and A_{ji} the Einstein coefficient for spontaneous emission, reflecting the transition probability. For an optically thin plasma, i.e., ignoring light absorption and scattering, the intensity of this spectral line over a distance is

$$\begin{aligned} I(\lambda_{ij}) &= \int \epsilon_{ji}\, dz \\ &= \frac{h\nu_{ij}}{4\pi} \int N_j(X^{+m}) A_{ji}\, dz \ \ (\mathrm{erg\ s^{-1}\ cm^{-2}\ ster^{-1}}) \end{aligned} \tag{1.34}$$

where the integration is along the line-of-sight. $N_j(X^{+m})$ can be written as a series of hierarchy ratios

$$N_j(X^{+m}) = \frac{N_j(X^{+m})}{N(X^{+m})} \frac{N(X^{+m})}{N(X)} \frac{N(X)}{N(H)} \frac{N(H)}{n_e} n_e \tag{1.35}$$

where the first term is the excitation ratio, the second one the ionization ratio, the third one the elemental abundance relative to hydrogen, and the last one the ratio of hydrogen to electron densities. We define a contribution function as

$$G(T, \lambda_{ij}) = \frac{h\nu_{ij}}{4\pi} \frac{A_{ji}}{n_e} \frac{N_j(X^{+m})}{N(X^{+m})} \frac{N(X^{+m})}{N(X)} \frac{N(X)}{N(H)} \frac{N(H)}{n_e} \tag{1.36}$$

which is determined by atomic physics and can be calculated using the CHIANTI atomic database (Dere et al. 1997; Landi et al. 2013). It is strongly peaked in temperature, but only has little dependence on electron density. And in the solar corona, $N(H) : n_e \approx 0.83$ for completely ionized H and He with abundances $10 : 1$, and $N(X) : N(H)$ is assumed as the coronal abundance. Then substitute Equation 1.35 into Equation 1.34 and utilize the definition of the contribution function, it follows that

$$I(\lambda_{ij}) = \int G(T, \lambda_{ij}) n_e^2\, dz \tag{1.37}$$

Then define a DEM equation (a more general form can be found in Craig & Brown (1976)),

$$\xi(T) = n_e^2 \frac{dz}{dT} \ \ (\mathrm{cm^{-5}\ K^{-1}}) \tag{1.38}$$

The intensity Equation 1.37 can be transformed into being integrated over temperature T,

$$I(\lambda_{ij}) = \int_0^\infty G(T, \lambda_{ij})\xi(T)\, dT \tag{1.39}$$

and also the total emission measure (EM) can be obtained,

$$\mathrm{EM} = \int_0^\infty \xi(T)\, dT \tag{1.40}$$

or

$$\mathrm{EM} = \int n_e^2\, dz \tag{1.41}$$

Sometimes, to measure the EM over a finite temperature interval $\triangle T$, the concept of emission measure distribution (EMD; Del Zanna et al. 2002) is also exploited,

$$\mathrm{EM}(T) = \int_{T-\triangle T/2}^{T+\triangle T/2} \xi(T)\, dT \tag{1.42}$$

The DEM is an effective way to have knowledge about the plasma distribution in the emitting source, which can be compared with theoretical models of plasma heating or acceleration. In practice, to derive the DEM we also need to consider the influence of instruments on observables (Boerner et al. 2012). The pixel value of the detector at the position $\boldsymbol{x}$ after removing the flat field is

$$g(\boldsymbol{x}) = \int_0^\infty R(\lambda)I(\lambda, \boldsymbol{x})d\lambda \tag{1.43}$$

where $R(\lambda)$ is the instrumental response funtion. Then substitute Equation 1.39 into Equation 1.43 and exchange the integration order, to get

$$g(\boldsymbol{x}) = \int_0^\infty K(T)\xi(T, \boldsymbol{x})dT \tag{1.44}$$

where $\xi(T, \boldsymbol{x})$ is the DEM along the line-of-sight with the position $\boldsymbol{x}$ as its base, and

$$K(T) = \int_0^\infty G(\lambda, T)R(\lambda)d\lambda \tag{1.45}$$

is called the kernel function or temperature response function, synthesizing both atomic physics and instrumental response. The AIA temperature response functions for different wavebands can be found in Figure 1.20.

Given observables g_i (also their error δg_i) for the ith filter ($i = 1, ..., N$) and corresponding temperature responses $\boldsymbol{K}_{i,j}$, we need to solve the following inverse problem to obtain the DEM information $\xi(T_j)$ of the emitting source (Hannah & Kontar 2012),

$$g_i = \boldsymbol{K}_{i,j}\xi(T_j) + \delta g_i\ . \tag{1.46}$$

It is equivalent to address the least square problem,

$$\|\frac{\boldsymbol{K}\xi(T)-\boldsymbol{g}}{\delta\boldsymbol{g}}\|^2 = \min\,. \tag{1.47}$$

However, without any constraint, the least square problem is ill-posed as the errors in the observables and temperature response functions will be significantly amplified in the inversion process. Hannah & Kontar (2012) apply linear constraints $\|\boldsymbol{L}(\xi(T)-\xi_0(T))\|^2 \leq$ const. to the problem and can get a solution with errors both in DEM and temperatures provided. The problem is then transformed into,

$$\|\tilde{\boldsymbol{K}}\xi(T)-\tilde{\boldsymbol{g}}\|^2 + \lambda\|\boldsymbol{L}(\xi(T)-\xi_0(T))\|^2 = \min \tag{1.48}$$

with a regularization parameter λ utilized, $\tilde{\boldsymbol{K}} = (\delta\boldsymbol{g})^{-1}\boldsymbol{K}$, $\tilde{\boldsymbol{g}} = (\delta\boldsymbol{g})^{-1}\boldsymbol{g}$, L the constraint matrix, and $\xi_0(T)$ the "guess" solution. λ is related to the χ^2 of the fit, and can be controlled as desired. The simplest form of $\boldsymbol{L}$, which is also commonly used, is the unit matrix $\boldsymbol{I}$, called zeroth-order constraint. And $\xi_0(T)$ can be chosen to be zero in the initial iteration step and changed to the first run result $\xi(T)$ in the second run, or chosen to be the minimum of the EM loci curves $\approx g_i/K_i$ (which are the emission measures for isothermal plasma) for high resolution spectroscopic observations, which reflects the maximum amount of plasma that can be obtained at a particular temperature. The solution to the minimization problem in Equation 1.48 is solved via the method of Generalized Singular Value Decomposition (GSVD; Hansen 1992). The rigorous technical detail can be refered to in Hannah & Kontar (2012).

Chapter 2

Peripheral Arcade Implosion Caused by a Central Filament Eruption

This work can be found in the publication Wang et al. (2016).

2.1 Introduction to the Chapter

Before this study, previous observations of peripheral implosions (Liu & Wang 2009; Gosain 2012; Liu et al. 2012a; Sun et al. 2012; Simões et al. 2013; Yan et al. 2013; Shen et al. 2014; Kushwaha et al. 2015) are doubted in the solar community and even by this author. These observations mainly show loops in the periphery of ARs contracting in a face-on state. Inclining of these face-on loops can lead to an illusion where we think it is contraction. Especially, these events all possess violent eruptions in the centre of ARs, which can easily push surrounding loops to incline. Some authors argue that these apparently contracting loops do not restore to their original positions, thus the motion could not be caused by the erupting structures, because if it was, the loops should come back when the eruption finishes. However, what is meant by "eruption finishes"? If the erupting flux rope does not reconnect and just stretches outward and inflates, or it reconnects with nearby structures and obtains more energy from this process, then the legs of the flux rope can hold the peripheral loops at their positions without restoration in place. Thus the argument used by previous authors is not adequate. In addition, they usually thought that the apparent contraction of these loops results from the magnetic energy dissipated in the flare, which was not properly demonstrated either.

In the work of this chapter, we report on the analysis of a well-observed peripheral implosion in the form of an arcade contraction associated with a filament eruption, during the C3.5 flare SOL2013-06-19T07:29. As will be shown, the reality of contraction of the loops is supported by three pieces of evidence from both observations and nonlinear force-free field extrapolations. A sequence of events including magnetic flux-rope instability and distortion, followed by filament eruption and arcade implosion, lead us to conclude that the implosion arises from the transfer of magnetic energy from beneath the arcade as part of the global magnetic instability, rather than due to local magnetic energy dissipation in the flare. This event shows that, in addition to resulting in expansion or eruption of overlying field, flux-rope instability can also simultaneously implode unopened field due to magnetic energy transfer. It demonstrates the "partial opening of the field" scenario, which is one of the ways in 3D to produce a magnetic eruption without violating the Aly-Sturrock hypothesis. In the framework of this observation we also propose a unification of three main concepts for active region magnetic evolution, namely the metastable eruption model, the implosion conjecture, and the standard "CSHKP" flare model.

In Section 2.2, the observations of the entire event are described. In Section 2.3, magnetic field extrapolations are exploited to reveal the implosion and possible reconnection between the filament and other AR field in the form of an extended "arm-like" structure. Discussion including possible scenarios for the evolution is presented in Section 2.4 and conclusions in 2.5.

2.2 Observations

2.2.1 Overview of the Event

On 2013 June 19, AR 11776 (N10W00) was located near the solar disk center (Figure 2.1). We focus our analysis around the period of the flare SOL20130619T07:29, GOES class C3.5. It was observed by the Reuven Ramaty High Energy Solar Spectroscopic Imager (RHESSI, Lin et al. 2012a) and by the Solar Dynamics Observatory (SDO, Pesnell et al. 2012) instruments: Atmospheric Imaging Assembly (AIA, Lemen et al. 2012) and Helioseismic and Magnetic Imager (HMI, Scherrer et al. 2012; Schou et al. 2012; Hoeksema et al. 2014). The AIA images have been processed using standard software (Boerner et al. 2012), and also rotated to 07:00 UT via the

drot_map.pro procedure, in order to compensate for the solar differential rotation. RHESSI images were reconstructed using the CLEAN algorithm (Hurford et al. 2002), with detectors 2 to 8 and the `clean_beam_width` set to 1.5 (Schmahl et al. 2007; Simões & Kontar 2013). No CMEs associated with the event were reported, while a type III radio burst was detected[1] (for a review of type III radio bursts, see Sinclair Reid & Ratcliffe 2014), as well as an EUV wave, which will be briefly presented in Section 2.2.2.1. We note that earlier on the same day a C2.3 flare was produced in this AR and studied by Zheng et al. (2015).

As the AR evolves, different features are identified, and we select two images in Figure 2.2 to illustrate. As can be seen, a bright arcade overlies a sheared filament in the core region, and in the south, there is a curved frontal structure. These three features are visible clearly before the flare-associated evolution of the AR. Flare I, Flare II and low-lying loops in Figure 2.2 appear during the following flare evolution, which will be discussed in the sections below. In the northeast, there is a large J-shaped arcade and some complex features underlying, but they are not involved in the activity in an apparent way, and thus will not be studied.

The main C3.5 flare was preceded by a microflare B6.0 (for a review of microflares see Hannah et al. 2011), also associated with this AR, as evidenced by the AIA 1600 Å ribbons and HXR emission imaged by RHESSI at 9-26 keV, as shown in Figure 2.2(a). Hereafter, we call this B6.0 microflare Flare I, and the subsequent C3.5 flare in Figure 2.2(b) Flare II.

From ~ 07:10 UT to 07:30 UT, the above features produce a rich sequence of phenomena. Figure 2.3 illustrates the dynamical evolution of the filament in 304 Å. The filament positions obtained from Figure 2.3 are then overlaid on the contemporary 171 Å images in Figure 2.4, which allows us to simultaneously track the evolution of the filament and the overlying arcade. Here we use the informative Figure 2.4 to briefly summarise the main phenomena and their evolution, which are also listed in Table 2.1. More detailed information about the evolution will be described in the following subsections. Firstly, in Figure 2.4(a), the filament located near the site of Flare I is disrupted at the time when Flare I peaks (~ 07:15:40 UT). It then brightens and starts to distort, and a bump or bend in the filament moves from west to east (Figure 2.4(b) to (d)). This appears to push the overlying arcade upward and aside. When most of the bump suddenly escapes from beneath the overlying arcade (~

[1] http://secchirh.obspm.fr/survey.php?hour=0600&dayofyear=20130619&survey_type=4

07:22 UT, Figure 2.4(e)), the filament's eastern part erupts and the overlying arcade starts to contract. Almost at the same time, Flare II happens. From Figure 2.4(f) to (h), the inner loops of the overlying arcade continue contracting until when the GOES 1-8 Å derivative reaches its peak (~ 07:25:45 UT; GOES lightcurves can be derived later in Figure 2.6(e)). Finally, the entire overlying arcade disappears in AIA 171 Å (Figure 2.4(i)). Figure 2.5 combines different wave bands (171, 211, 304 and 94 Å) to illustrate the main events happening during the impulsive phase of Flare II for readers' convenience.

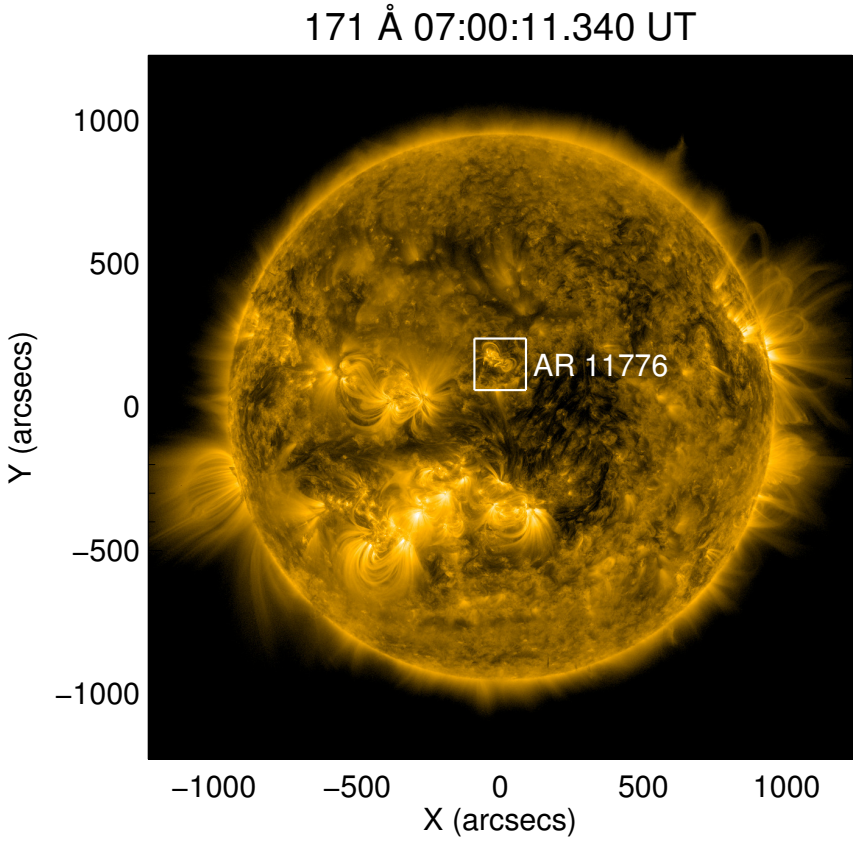

Figure 2.1: Full Sun image shows the AR 11776 on 2013 June 19 in AIA 171 Å. The white square region is the field of view (FOV) used in Figure 2.2.

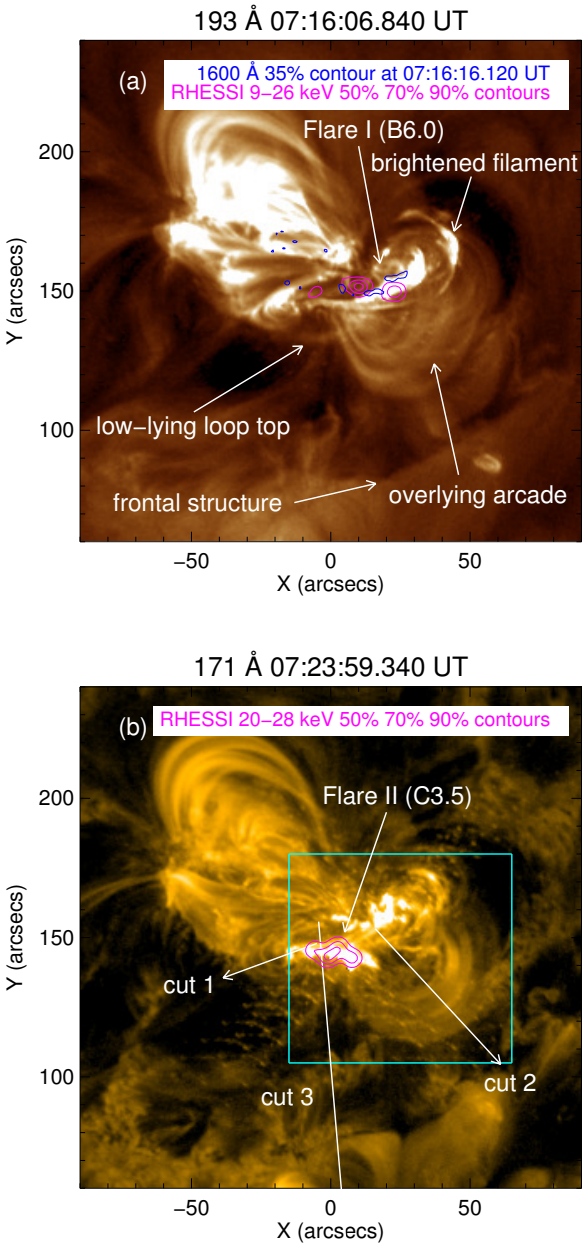

Figure 2.2: Main features and processes identified in the 193 and 171 Å passbands. (a) 193 Å. The magenta contours for the 9-26 keV RHESSI HXR emission are integrated from 07:15:00 UT to 07:16:12 UT. (b) 171 Å. The magenta contours for the 20-28 keV RHESSI HXR emission are integrated from 07:22:00 UT to 07:24:36 UT. Cut 1 is used to make the timeslices for the filament's eastern part in Figure 2.6(a) (the filament's eastern and western parts are denoted in Figure 2.3(a) with the same FOV); cut 2 for the filament's western part and the overlying arcade in Figure 2.6(b); cut 3 for the low-lying loop top and the frontal structure in Figure 2.6(c). The arrowhead of cut 3 is beyond the image edge. The cyan rectangular region is used to make AIA lightcurves in Figure 2.6(f).

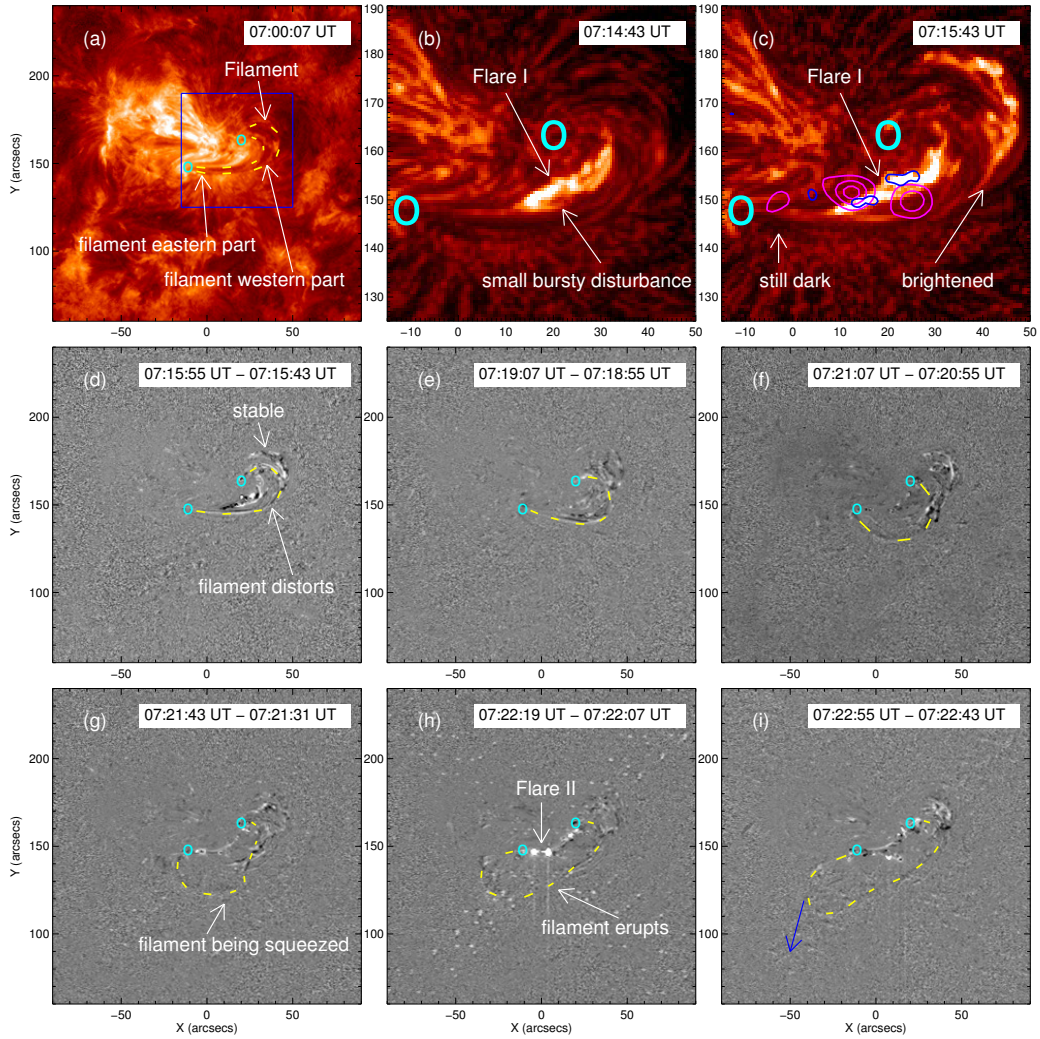

Figure 2.3: Dynamical evolution of the filament in 304 Å. (a) Denotes the position of the filament. The two cyan circles indicate the rough locations of the footpoints of the filament. The blue square region is the FOV used in (b) and (c). (b) Zoom in to show Flare I and its produced small bursty disturbance. (c) Zoom in to show the brightening filament's western part and still dark eastern part around the peak of Flare I. The blue contours are in 1600 Å at ~ 07:15:52 UT. The magenta contours are the same as in Figure 2.2(a). (d)-(i) Running difference images show the subsequent distortion and eruption of the filament. The yellow dashed line represent the shape and position of the filament in each image, which are determined by examining the multi-scale Gaussian normalisation (MGN; Morgan & Druckmüller 2014) processed running difference image in 304 Å. The filament after (i) cannot be seen in the images, but still can be tracked on the animation of the running difference. The blue arrow in (i) indicates the erupting direction of the filament's eastern part, and its head points to the rough location of the filament top when it disappears. It should be noted that (b) and (c) have been processed using the MGN procedure; the (d)-(i) running difference images are created after being processed using the MGN procedure. An animation is available in Wang et al. (2016) at the link http://iopscience.iop.org/article/10.3847/1538-4357/833/2/221/meta.

In Figure 2.2(b), we select three cuts to make timeslices for demonstrating the dynamical evolution of the filament's eastern part (cut 1), the overlying arcade and the filament's western part (cut 2), and the frontal structure and the low-lying loops (cut 3). The obtained timeslices, along with RHESSI HXR, GOES soft X-ray (SXR) and AIA lightcurves are collected in Figure 2.6. In the subsections below, combined with the information in Figure 2.6, we describe the processes in detail in order to give readers a more complete picture of the event.

2.2.2 Flare I and Filament Eruption

After analysing RHESSI images, we note that the gradual increase at 3-6 keV and 6-12 keV from 07:00 UT to about 07:15 UT in Figure 2.6(d) is contributed by a limb event (no HXR source can be detected). Only the small bump around 07:15:40 UT (indicated by "A" in Figure 2.6(d)) is the Flare I considered here, most prominent at RHESSI 12-25 keV and AIA lightcurves in Figure 2.6(d) and (f), respectively. Its two ribbons in AIA 1600 Å and RHESSI HXR contours can be clearly seen in Figure 2.2(a) and Figure 2.3(c), just encircled by the nearby filament.

Figure 2.3 presents the activities in 304 Å. At ~ 07:00 UT, the filament has a sheared appearance, with its bump pointing to the west (Figure 2.3(a)). Then Flare I occurs, and at ~ 07:14:43 UT, it seems to produce a small bursty disturbance, pointing to the filament's western part (Figure 2.3(b)). Around 1 min later, at 07:15:43 UT when Flare I peaks (revealed by the RHESSI 12-25 keV lightcurve and indicated by "A" in Figure 2.6(d)), the filament's western part suddenly brightens, with some plasma flowing to its northern footpoint (seen in the 304 Å animation in Figure 2.3), though the eastern part is still dark (Figure 2.3(c)). Subsequently, the filament becomes distorted, with its bump propagating from west to east, though there is still part of the filament remaining relatively stable (Figure 2.3(d)-(f)). The dark trajectory and the bright path denoted by "filament eastern part" and "filament western part" in Figure 2.6(a) and (b) just show the filament's eastern and western parts sweeping across cut 1 and 2 of Figure 2.2(b) during the distortion, respectively (an exponential line is overlaid in Figure 2.6(a) to approximate the trajectory). When the bump propagates close to the filament's eastern end, the western part contracts, which appears squeezed and highly energised, and the entire filament expands more outward (Figure 2.3(g)). Then in Figure 2.3(h) the eastern part erupts dramatically

and nonradially, as a cool, extending feature at ~ 07:22 UT (see the 304 Å animation in Figure 2.3), and almost simultaneously, Flare II happens (indicated by "B" in Figure 2.6(d)). Such an eruption can be categorised as a whipping-like asymmetric filament eruption (Liu et al. 2009a; Joshi et al. 2013). Because during the eruption the filament is too weak and vague, even in the running difference images, and Flare II produces strong flashes, we are not able to select a cut to describe the following movement of the filament after ~ 07:22 UT. Thus the trajectory in Figure 2.6(a) for cut 1 mainly demonstrates the kinematics of the filament's eastern part in the previous distortion phase before ~ 07:22 UT, but the 304 Å animation in Figure 2.3 (and also its running difference version) can be taken as a reference for the following eruption of the filament's eastern part because of its moving nature. The bright path denoted by "filament western part" in Figure 2.6(b) shows that the filament's western part expands again after ~ 07:22 UT when the filament's eastern part erupts. The entire filament in Figure 2.3(h) seems relaxed from the squeezed state in Figure 2.3(g), like an elastic tube which can be stretched. The arrow in Figure 2.3(i) denotes the erupting direction of the filament's eastern part, and its head indicates the rough location of the filament top when it disappears.

2.2.2.1 Other Structures Associated with the Filament Eruption

An interesting development is that an eastern arm-like structure also brightens and expands outwards with the filament (see Figure 2.5(d) and Figure 2.7), which can only be clearly seen in 94 Å. We again overlay the positions of the contemporary filament obtained from the 304 Å running difference images like in Figure 2.3 onto the 94 Å images in Figure 2.5(d) and Figure 2.7. The final projected positions of the expanding portion of this arm-like structure and of the filament's erupting top seem near to each other before they disappear, around the southeastern corner of Figure 2.7(i) (the arrow in Figure 2.5(d) and Figure 2.7(h) denote the erupting direction of the filament's eastern part, and its head indicates the rough location of the filament top when it disappears, like in Figure 2.3(i)). This might make a reconnection between the arm-like structure and the filament possible, which will be discussed in Section 2.3.2.

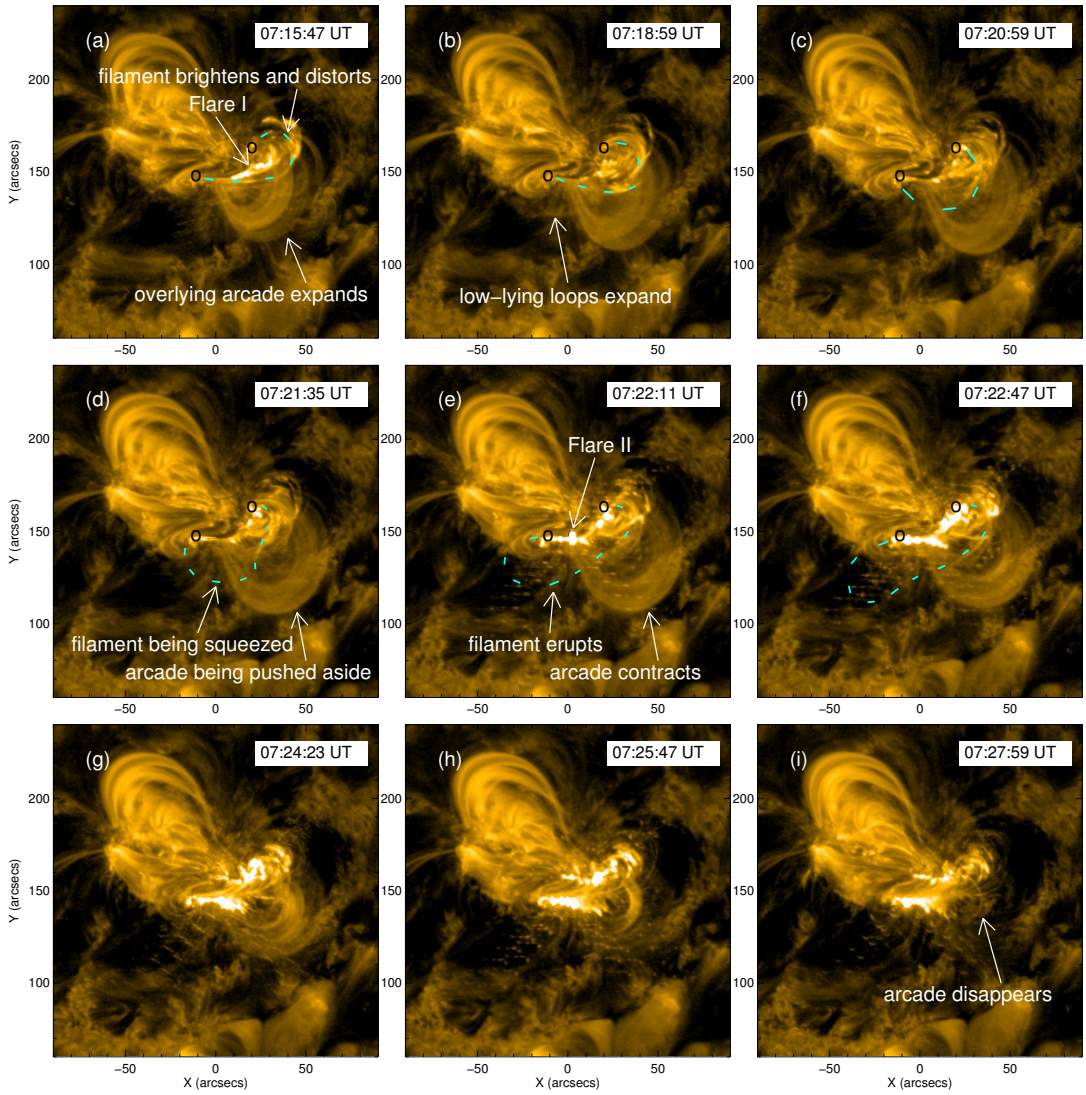

Figure 2.4: Dynamical evolution of the overlying arcade in 171 Å. The contemporary position of the filament obtained via the 304 Å running difference image as in Figure 2.3 is overlaid in each image, if possible. The filament after (f) is too weak to be located, but still can be seen in the 304 Å animation in Figure 2.3 because it is moving. An animation is available in Wang et al. (2016) at the link http://iopscience.iop.org/article/10.3847/1538-4357/833/2/221/meta.

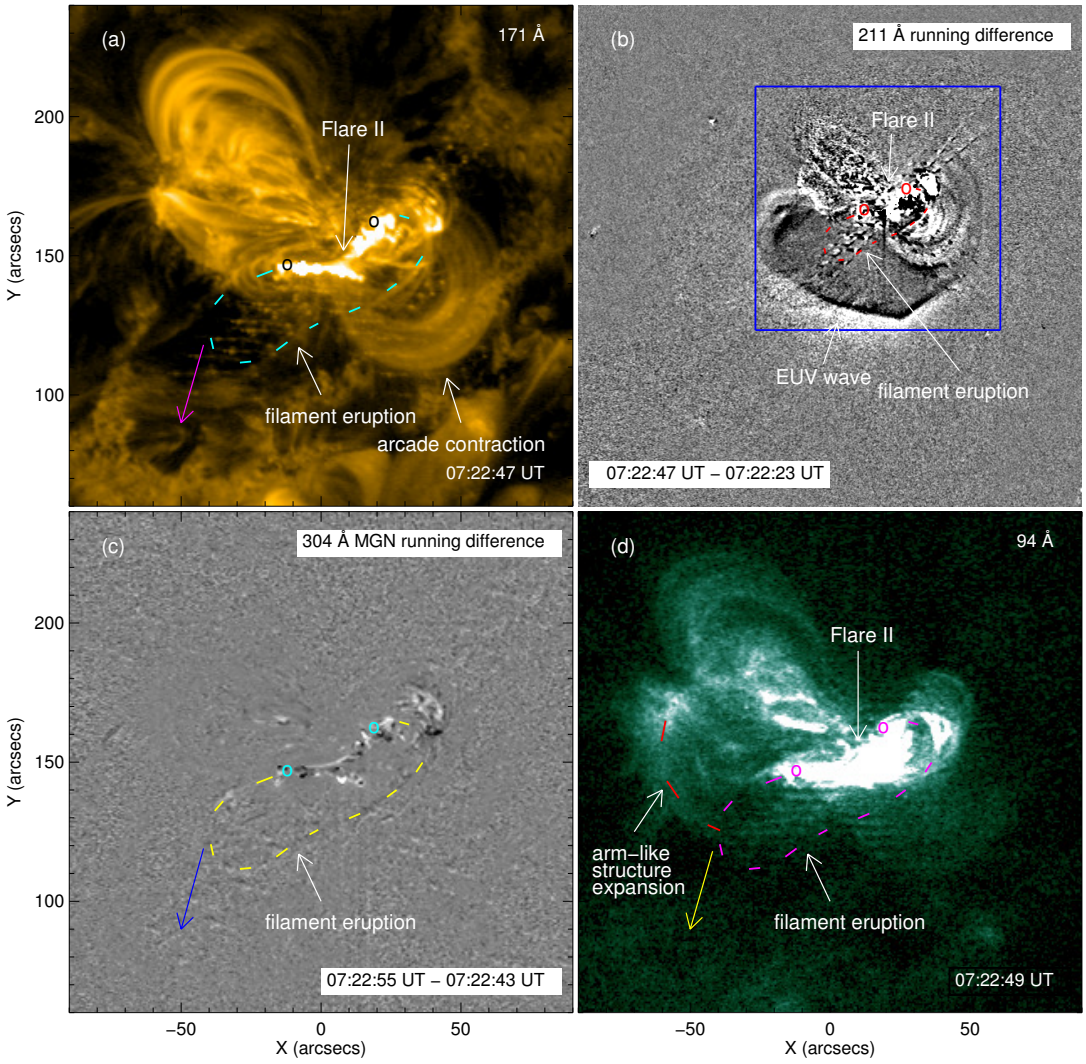

Figure 2.5: Different wave bands show the main events simultaneously during the impulsive phase of Flare II. (a) Arcade contraction in 171 Å, same as Figure 2.4(f). (b) EUV wave showed by 211 Å running difference. The blue square region is the FOV of the other three. (c) Filament eruption showed by 304 Å MGN running difference, same as Figure 2.3(i). (d) Arm-like structure expansion in 94 Å, same as Figure 2.7(h). The contemporary position of the filament obtained via the 304 Å running difference image as in Figure 2.3 is overlaid in each image. The arrow located around (-50, 100) in (a), (c) and (d) indicates the erupting direction of the filament's eastern part, and its head points to the rough location of the filament top when it disappears. An animation is available in Wang et al. (2016) at the link http://iopscience.iop.org/article/10.3847/1538-4357/833/2/221/meta.

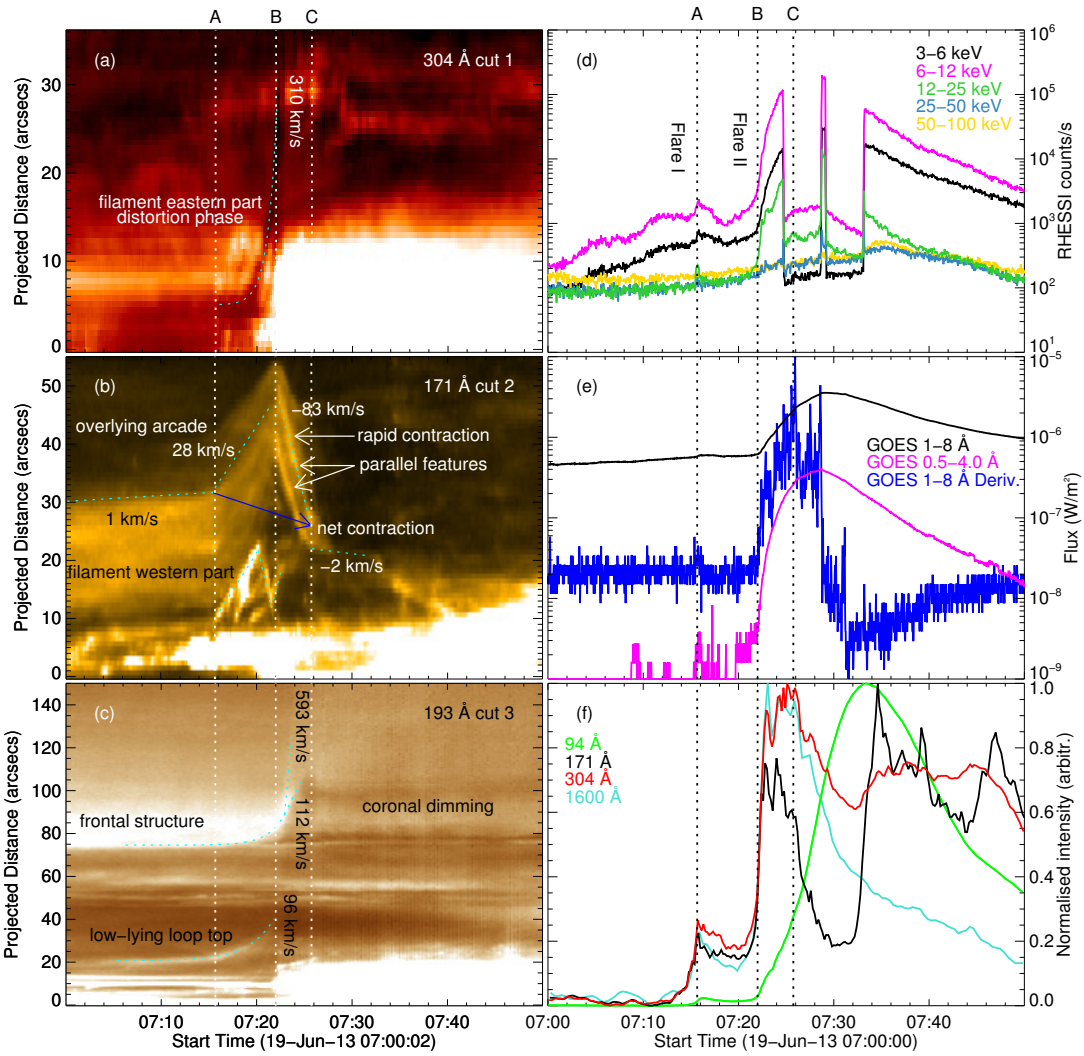

Figure 2.6: Evolution of the flare. The cuts for the timeslices in (a)-(c) are shown in Figure 2.2(b). Different wavebands are used for cut 1, 2 and 3, because some features studied can only be clearly seen in specific wavebands. The letters A, B and C above the figures are used to denote the main event timings in Table 2.1. (a) The timeslices in 304 Å for cut 1 only show the distortion phase of the filament's dark eastern part. Its following dramatic eruption after 07:22 UT, unfortunately, cannot be tracked, because it is too weak (see the text in Section 2.2.2 for detailed explanation), but it still can be seen in the 304 Å animation in Figure 2.3 because it is moving. (b) The timeslices in 171 Å for cut 2 show the expansion and contraction of both the overlying arcade and the filament's western part. (c) The timeslices in 193 Å for cut 3 show the expansion of both the frontal structure and the top of the low-lying loops. (d) RHESSI lightcurves in different wave bands. Note that the gradual increases at 3-6 keV and 6-15 keV from 07:00 UT until the small bump around Flare I are contributed by a limb event rather than this AR considered here. (e) GOES lightcurves. The GOES 1-8 Å derivative has been normalised to fit the panel. (f) Normalised AIA lightcurves within the cyan rectangular region of Figure 2.2(b).

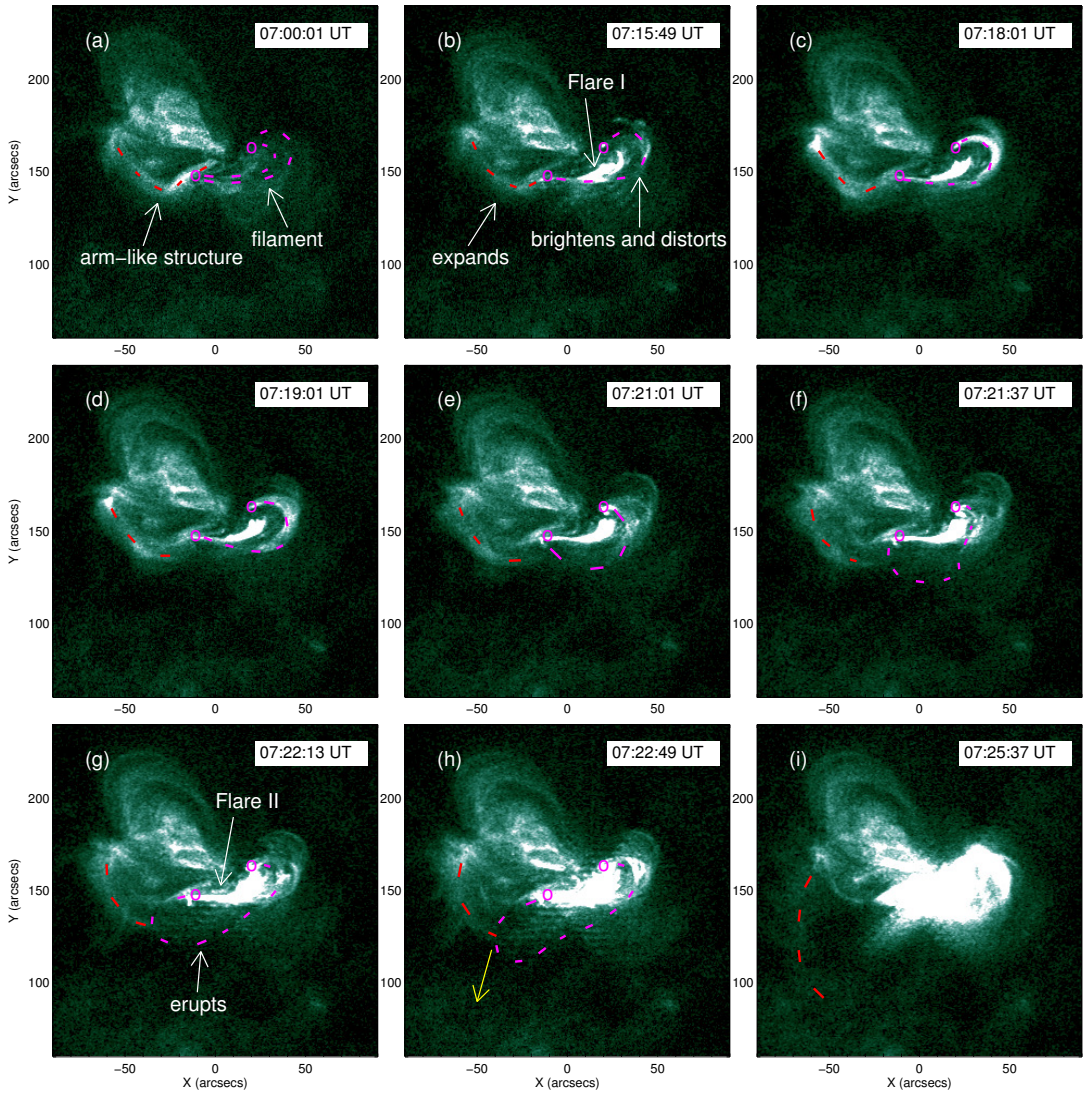

Figure 2.7: Evolution of the arm-like structure in 94 Å. The contemporary position of the filament obtained via the 304 Å running difference image as in Figure 2.3 is overlaid in each image, if possible. The yellow arrow in (h) indicates the erupting direction of the filament's eastern part, and its head points to the rough location of the filament top when it disappears, as in Figure 2.3(i). An animation of the 94 Å evolution can be found in Wang et al. (2016) at the link http://iopscience.iop.org/article/10.3847/1538-4357/833/2/221/meta.

In Figure 2.2(a), far to the south of the filament, there is a frontal structure, most prominent in 193 and 211 Å. It exists even before the two flares, and could be a stable cavity edge as described in Hudson et al. (1999). This global structure is similar to

that of a CME with a filament at the bottom, a cavity in the middle and a frontal loop at the top. From the timeslices in Figure 2.6(c) for cut 3 of Figure 2.2(b), it can be seen that the frontal structure also starts expanding exponentially at ~ 07:15:40 UT when Flare I peaks. At ~ 07:22:40 UT, it begins to diffuse with a leading edge ~ 593 km/s and a trailing edge ~ 112 km/s. And behind the trailing edge, a coronal dimming appears. This may be consistent with the hybrid EUV wave model, with a fast-mode wave component ahead of a CME-driven compression front (see Liu & Ofman 2014, and references therein). In addition, in the 211 Å running difference animation in Figure 2.5, we also note that there are quasi-periodic wave trains accompanying the EUV wave (see Liu & Ofman 2014, and references therein). Here we just point out that an EUV wave with quasi-periodic wave trains exists in this event, which is associated with the expanding frontal structure, and also suggest that it should be added in the list at the link `http://www.lmsal.com/nitta/movies/AIA_Waves/oindex.html` for future study. No further discussion will be presented because it is beyond the scope of this thesis.

Table 2.1: The main evolution in SOL2013-06-19.

Time	Events
~ 07:15:40 (A)	Flare I peaks; filament's western part brightens and starts to distort; overlying arcade starts to expand.
~ 07:22:00 (B)	filament's eastern part erupts; Flare II starts; overlying arcade starts to contract.
~ 07:25:45 (C)	inner loops of the overlying arcade contract to a relatively stable position; GOES 1-8 Å derivative reaches its peak

Note that the letters A-C are used in Figure 2.6 to indicate the event timings.

2.2.3 Overlying Arcade Expansion & Contraction

Figure 2.4 illustrates the dynamical evolution of the overlying arcade, overlaid by the contemporary positions of the filament. The timeslices in Figure 2.6(b) for cut 2 of Figure 2.2(b) show that the overlying arcade has a small increase in height from 07:00 UT to ~ 07:15:40 UT. Then at ~ 07:15:40 UT when Flare I peaks and the filament starts to distort, it accelerates to expand at a nearly uniform apparent

speed of ~ 28 km/s (Figure 2.4(a) to (d)). In the 171 Å animation in Figure 2.4, it also seems to be pushed aside and incline towards the solar disk during the end of this expansion phase (see also Figure 2.4(d)). The low-lying loops (Figure 2.2(a) and Figure 2.4(b)) overlying the filament's eastern part appear and also start to expand (revealed by the timeslices in Figure 2.6(c) for cut 3 of Figure 2.2(b)). At ~ 07:22:00 UT when the filament's eastern part erupts and Flare II occurs, the overlying arcade motion turns to a rapid contraction at a nearly constant apparent speed of ~ 83 km/s (Figure 2.4(e)). Figure 2.4(e) to (h) show that a moderate inclination of the arcade seems to accompany the rapid contraction (also see the 171 Å animation in Figure 2.4 after ~ 07:22 UT). Shown in Figure 2.6(b), the inner loops of the arcade contract rapidly by about a half with respect to the starting position of cut 2 until ~ 07:25:45 UT (the starting position of cut 2 is around the middle of the two footpoints of the contracting arcade, as can be seen in Figure 2.2(b)), which also can be seen by comparing Figure 2.4(e) with (h). As the rapid contraction of the inner loops stops, the derivative of GOES 1-8 Å flux peaks (indicated by "C" in Figure 2.6(e)). Thus the rapid contraction may only happen during the rise stage of the impulsive phase (Neupert effect; Neupert 1968). The projected net contraction of the arcade indicated by the blue arrow (which connects the beginning of the rapid expansion to the ending of the rapid contraction) in Figure 2.6(b) is ~ 4.5 arcsecs. At the end, the entire overlying arcade disappears (Figure 2.4(i)).

2.3 Magnetic Field Extrapolation

We employ a NLFFF model approach (Section 1.4.5) in order to explore the coronal magnetic field configuration before and after the C3.2 flare. The field extrapolation was conducted by Julia Thalmann in Institute of Physics, University of Graz. Photospheric vector magnetograms obtained by SDO/HMI between 06:00 UT and 09:00 UT (excluding the one at 07:24 UT when the violent C3.2 flare happens, because the quasi-equilibrium state required for NLFFF extrapolation will not be satisfied), with a 12 minute cadence (the vector data is also averaged in a 12-minute period) and a ~ 1.0 arcsec spatial resolution, are used as input to our modeling. The extension of our model volume is $\approx 331 \times 258 \times 129$ arcsec, i.e., $\approx 244 \times 190 \times 95$ Mm, centered around solar $(x, y) = (-28.2, 137.9)$ arcsec. This proximity of the considered area to the disk center allows us to neglect eventual projection (foreshortening) effects. The

vertical magnetic flux within the area is balanced to within $\approx 10\%$.

Using standard IDL mapping software, we de-rotate the measured magnetic field vector maps to the flare peak time and project the data to a local coordinate system (following Gary & Hagyard 1990). The observed non-force-free photospheric data is driven to a more force-free consistent field configuration, following Wiegelmann et al. (2006), which is then supplied to the NLFFF modeling scheme as a lower boundary condition (for details of the method see Wiegelmann & Inhester 2010; Wiegelmann et al. 2012; and Section 2.2.1 of DeRosa et al. 2015).

In order to quantify the goodness of the obtained NLFFF model solutions we use some of the metrics introduced in Wheatland et al. (2000). First, we test the success of recovering a force-free solution using the current-weighted average of the sine of the angle between the model magnetic field and the electric current density, where we find σ_j on the order of 10^{-1} (note that for a perfectly force-free solution one would find $\sigma_j = 0$). Second, we calculate a measure for the solenoidality of the model solution, in the form of the volume-averaged fractional flux, and find $\langle |f_i| \rangle$ on the order of 10^{-4} (for a perfectly solenoidal solution one would find $\langle |f_i| \rangle = 0$). That indicates that our NLFFF models are force-free and solenoidal to a necessary degree in order to validly approximate the pre- and post-flare coronal magnetic field.

2.3.1 Overlying Arcade Contraction

In order to picture the flare-associated magnetic field evolution, we trace model magnetic field lines from certain locations at the NLFFF model lower boundary. Since the photospheric field (used as input to the modelling) is evolving in time, the same coordinates at different times may correspond to physically different structures. Therefore, we use a group of field lines occupying a large region, and study their statistics, which can diminish the above influence. We choose the area Po (5×5 arcsecs, comparable to the overlying arcade footpoint area in the positive polarity region in AIA 171 Å; see Figure 2.8) as the leading footpoint region, that is the footpoint region from which the extrapolated field lines are calculated (Wiegelmann et al. 2013). The area No defines the region where the arcade connects at the negative magnetic polarity. We take all the calculated field lines from Po to No as the overlying arcade at different times. By visually comparing the arcades of considered model field lines between 07:12 UT and 07:36 UT in Figure 2.8, it appears

that the number of longer (red or yellow) field lines decreases and that of shorter (blue) ones increases (the total numbers of the field lines at these two times are comparable, thus the comparison is valid). This is more obvious from the normalised histograms of lengths of field lines in Figure 2.9(a), with the fraction of longer field lines decreasing and that of shorter ones increasing after the flare. Globally, the histogram is shifted to shorter length. In addition, in Figure 2.9(b), we construct normalised histograms of the field strengths at all pixels along all of the individual field lines in the reconstructed overlying arcade. They show that with the contraction, the magnetic field strength of the arcade is globally enhanced after the flare.

From AIA 171 Å images it is not possible to detect the lower and shorter field lines in Figure 2.8(b) and (e). Thus in order to compare the extrapolations with AIA observations, we choose the field lines with lengths larger than average, and calculate the average projected distances of the midpoints of the field lines to the midpoints of the lines connecting their conjugate footpoints at both 07:12 UT and 07:36 UT. Their difference reflects the average projected contraction distance. The obtained value is ~ 4.7 arcsecs, which is in good agreement with the net projected contraction ~ 4.5 arcsecs observed in AIA 171 Å (the blue arrow in Figure 2.6(b)).

The evolution of lengths (and strengths) of the model field lines in the reconstructed arcade from 06:00 UT to 09:00 UT are further explored. We use the same "timeslices" technique as in the time-distance diagrams in Figure 2.6, but here in Figure 2.10 each timeslice represents a colour-coded normalised *cumulative* histogram. The black gap at 07:24 UT is when Flare II and arcade contraction happen, thus the extrapolation data is not used. The idea of this figure is to show how the distribution of lengths (and strengths) evolves in time. The black regions at the top and bottom mean that there are no field lines of those lengths there, and the field lines exist in those blue, green and red regions. As we can see, before the flare most of the field lines have lengths between $\sim$ 40-80 Mm, and after the flare this range shifts down to $\sim$ 30-70 Mm. In addition, before the flare the general trend of the field line lengths is increasing (though a relatively strong activity at $\sim$ 06:30 UT, compared to slow evolution in the rest time from 06:00 UT to 07:00 UT, may affect the reliability of the extrapolations at 06:24 UT and 06:36 UT), whereas after the flare it turns to decreasing. The evolution of the field strength of the model arcade in Figure 2.10(b) shows an opposite trend.

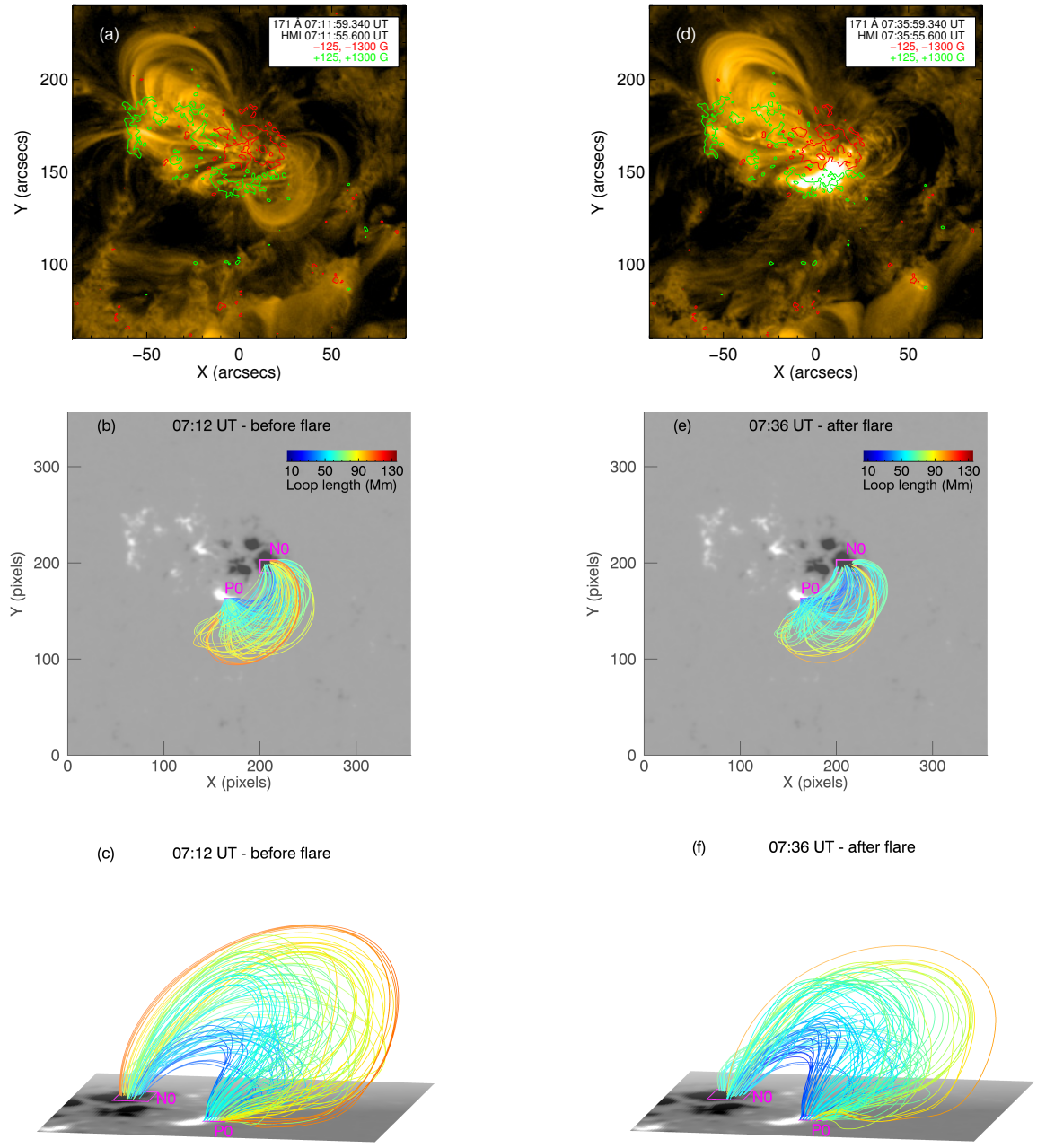

Figure 2.8: Overlying arcade contraction found in the extrapolation. (a) Longitudinal magnetogram overlaid on AIA 171 Å image at around 07:12 UT (before flare) for comparison with extrapolation. (b) The overlying arcade in extrapolation at around 07:12 UT. Po and No are the areas used to select the field lines. The FOV is approximately the same as in (a). 1 pixel ≈ 0.5 arcsecs. (c) 3D view of the overlying arcade at 07:12 UT. (d)-(f) Same as (a)-(c), but at 07:36 UT (after flare).

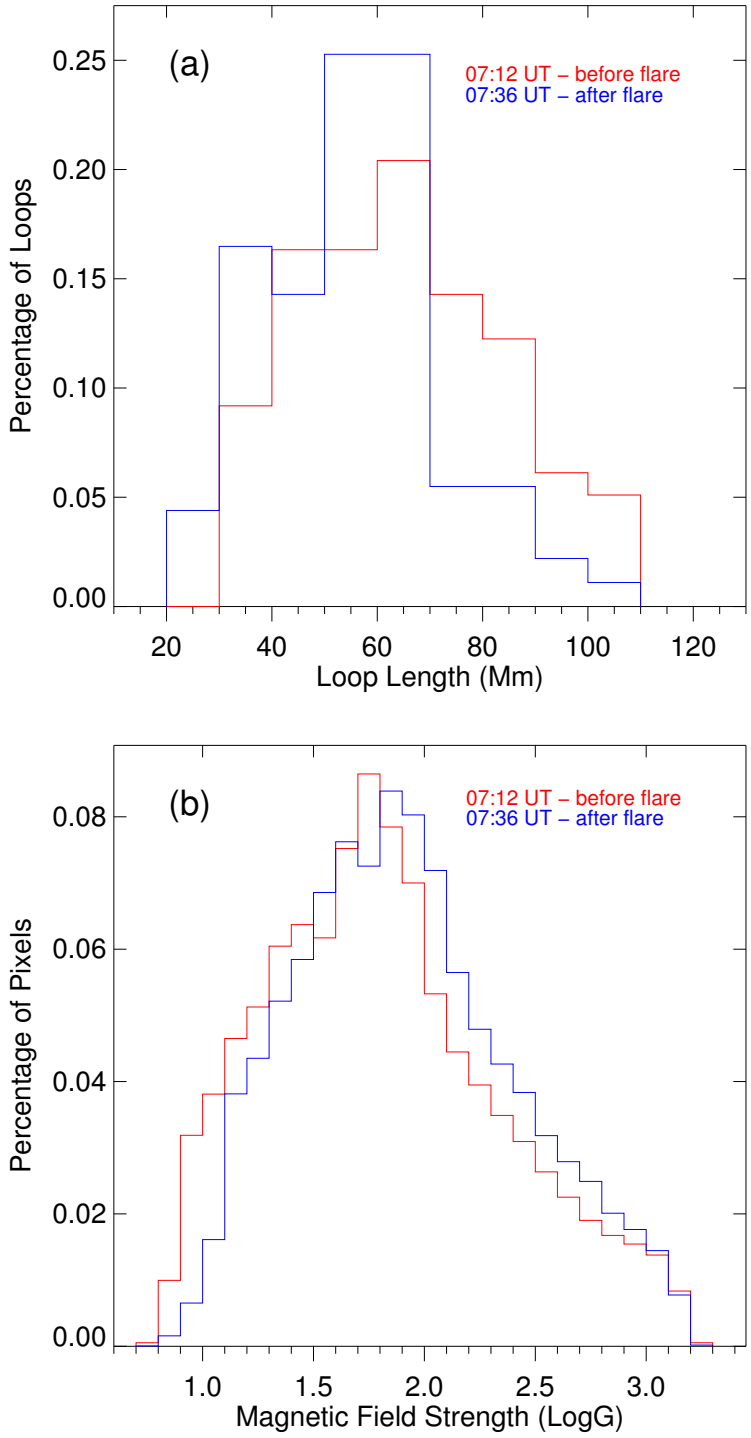

Figure 2.9: Lengths and magnetic field strengths of the extrapolated overlying arcade field lines shown in Figure 2.8 between before and after flare. (a) Normalised histograms of the lengths of the arcade field lines. (b) Normalised histograms of the magnetic field strengths of all pixels of the extrapolated arcade.

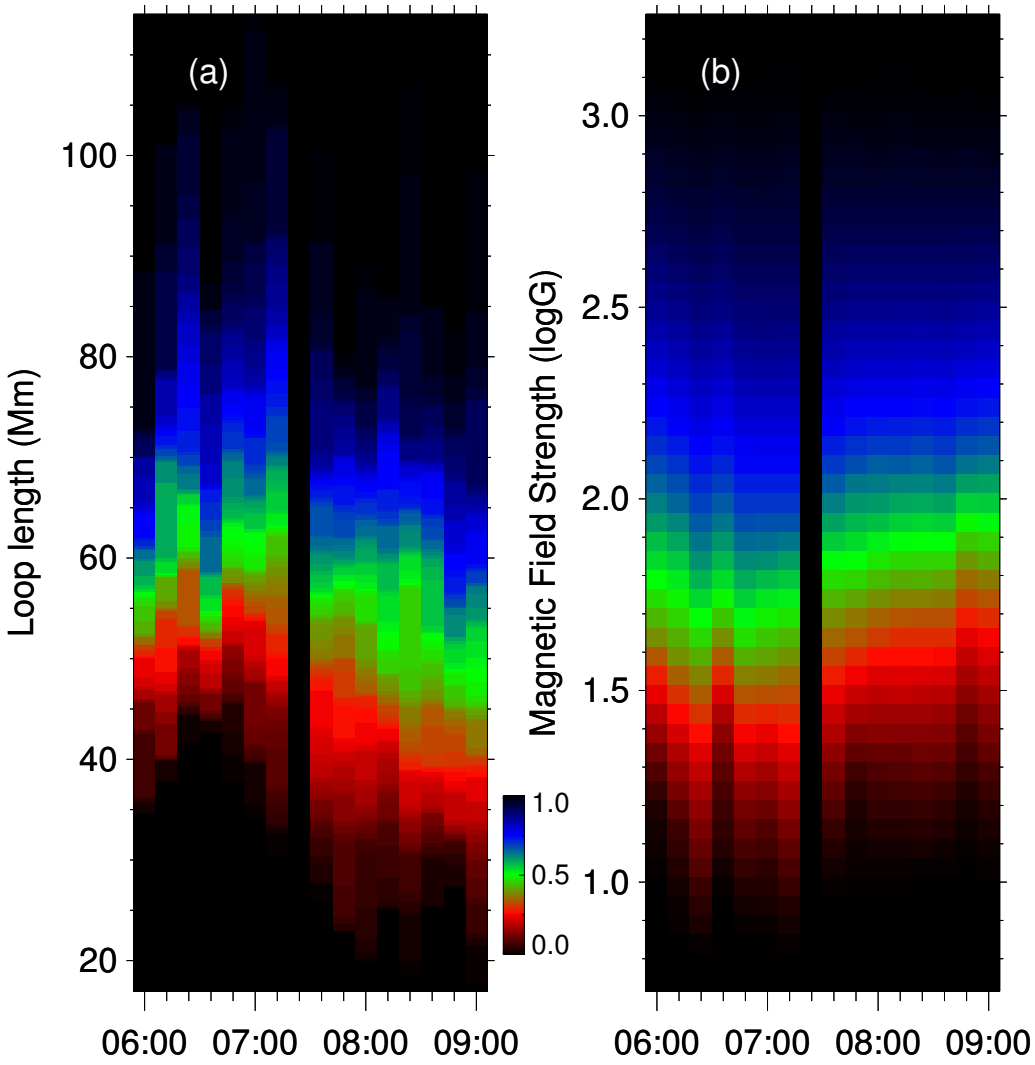

Figure 2.10: Evolutions of the lengths and magnetic field strengths of the extrapolated arcade field lines from 06:00 UT to 09:00 UT. (a) Color coded timeslices of normalised cumulative histograms of the lengths of the arcade field lines. The black gap at 07:24 UT is when Flare II happens, whose extrapolation data is not used. The timeslices at 06:24 UT and 06:36 UT are less reliable (see the text in Section 2.3.1 for the explanation). (b) Color coded timeslices of normalised cumulative histograms of the magnetic field strengths of all pixels of the extrapolated arcade field lines.

2.3.2 Flux Rope and Connectivity Changes

As the overlying arcade and the filament western part share the same expansion and contraction speeds, which can be seen in Figure 2.6(b), the overlying arcade dynamics

may be controlled by the filament underneath, or more correctly by its magnetic flux rope. The filament also seems to be the driver of the subsequent flare evolution. Thus it is important to study the change of the filament. As the extrapolation only applies to quasi-equilibrium evolution, we then infer its behaviour from the initial and final extrapolated states.

At 07:00 UT, before the flare, we find the possible flux rope involved in the activity (blue clustered field lines in Figure 2.11(b)) in an area P1 of positive polarity and strong vertical currents, seen in Figure 2.11(a). The rope is very sheared and connected to an area N1 which is just south of the overlying arcade footpoints in the northern negative polarity region. In orientation and size it is very similar to, and could be, the filament seen in AIA 304 Å (Figure 2.3(a)). At 07:48 UT, after the flare, we use the same flux rope footpoints in Figure 2.11(b) at 07:00 UT as the leading footpoints to calculate the new field line connectivities. Figure 2.11(e) shows that the field lines from P1 are now connected to a closer negative polarity area N2 while those from N1 now connect to the far eastern positive polarity region P2. These two new magnetic systems both become less sheared compared to the original flux rope in Figure 2.11 (b). The vertical current densities in P1 and N1 meanwhile decrease whereas that in N2 increases.

To further investigate the change in connectivity, we use the footpoints obtained above in P2 and N2 as leading footpoints, and calculate their connection states before the flare at 07:00 UT. The result in Figure 2.11(b) - not including the blue clustered flux rope field lines - shows that P2 and N2 are mostly connected by the yellow field lines before the flare, whose profile in the south is very similar to the shape of the expanding arm-like structure seen in AIA 94 Å in Figure 2.7. Hereafter we call these yellow field lines arm-like field lines. As exhibited in Figure 2.5(d) and Figure 2.7, the arm-like structure in 94 Å and the erupting filament in 304 Å accompany each other during the eruption, and they both disappear off the edge of Figure 2.7(i). Thus it may be possible that they reconnect and exchange footpoints during the eruption, leading to a change in the field configuration from that in Figure 2.11(b) to that in Figure 2.11(e).

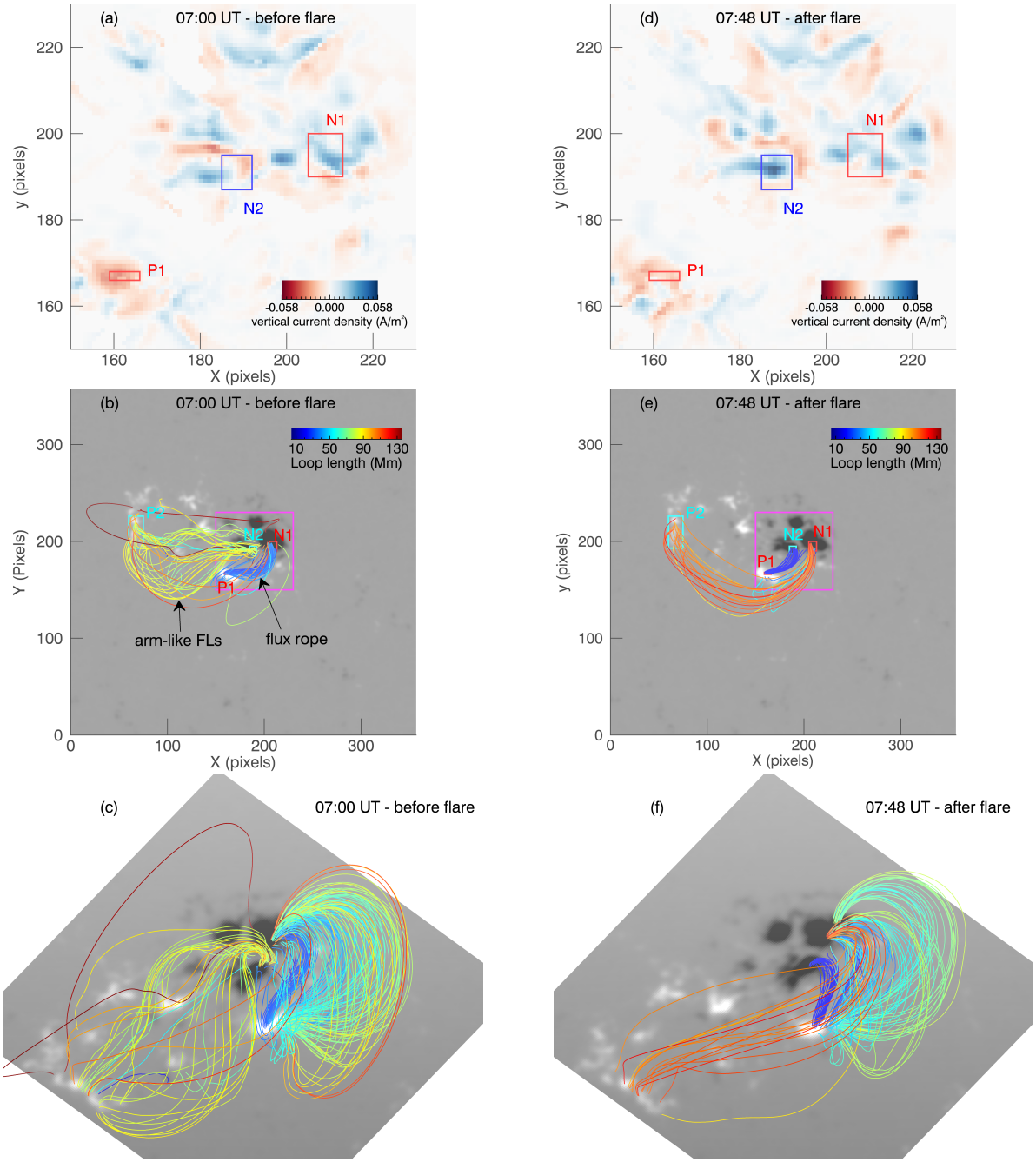

Figure 2.11: Possible flux rope reconnection scenario. (a) Photospheric vertical current density diagram in the magenta square region in (b) at 07:00 UT (before flare). (b) Connectivities at 07:00 UT (before flare). The FOV is approximately the same as in Figure 2.2. 1 pixel ≈ 0.5 arcsecs. (c) 3D view of the connectivities in (b). (d)-(f) Same as (a)-(c), but at 07:48 UT (after flare). The overlying arcade is added in (c) and (f) appearing on the right to show its relative position and the accompanying implosion.

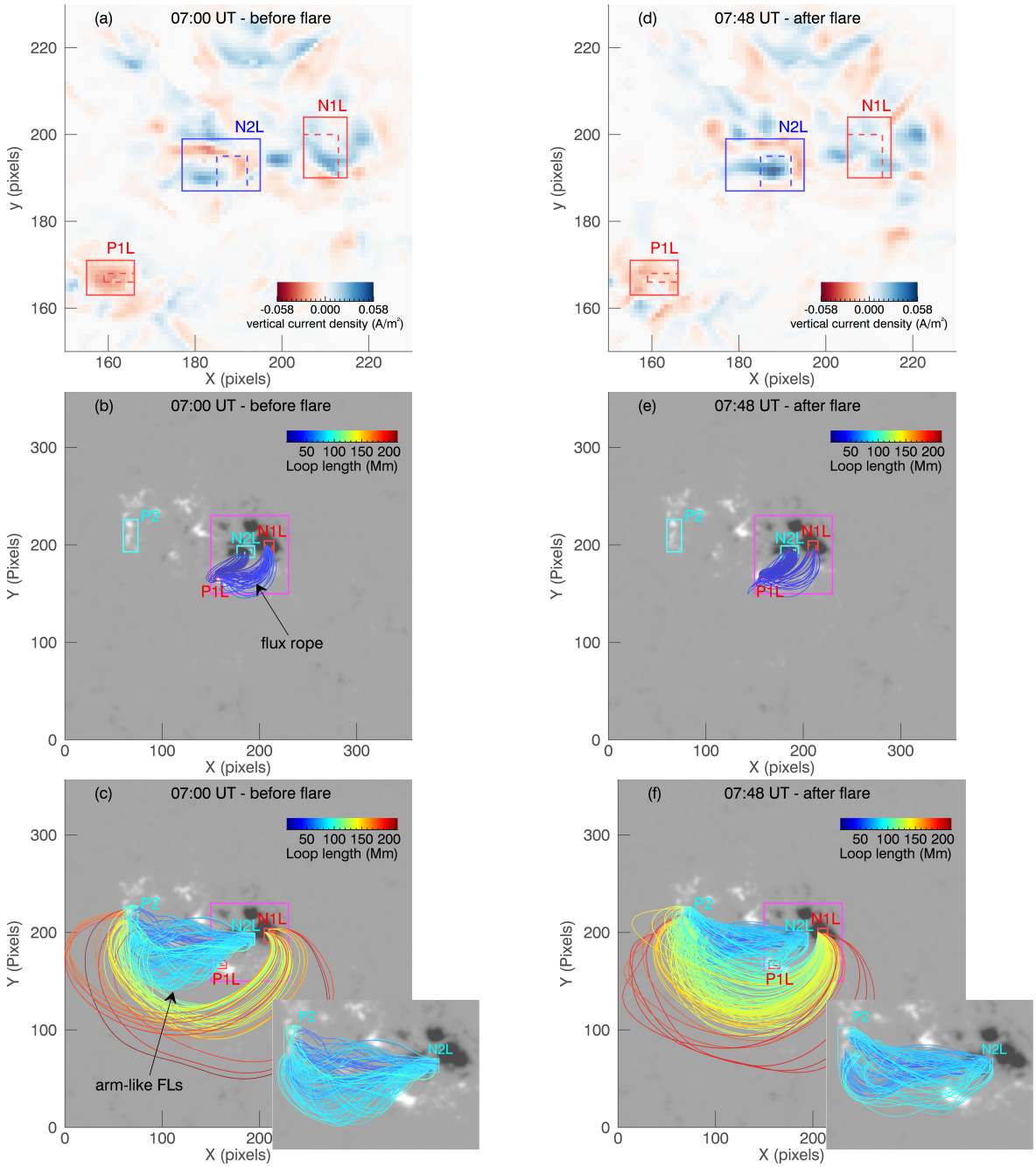

Figure 2.12: Connectivity states between the four regions, P1L, N1L, P2, N2L, before and after the flares. (a) Photospheric vertical current density diagram in the magenta square region in (b) at 07:00 UT (before flare). The solid larger boxes are chosen to reduce the influence of possible photospheric magnetic field evolution. The dashed smaller boxes are the original ones in Figure 2.11. (b) Connectivities from P1L to N1L and N2L at 07:00 UT (before flare). (c) Connectivities from P2 to N1L and N2L at 07:00 UT (before flare). The arm-like field lines are cyan now because the color table scale is changed. (d)-(f) Same as (a)-(c), but at 07:48 UT (after flare). As the connectivities from P2 to N2L in (f) are obscured, we plot them in the inset at the corner of (f), same as in (c).

In the above analysis, we have only used some specific footpoints in areas P1, N1, P2 and N2 for field line calculation. However, as stated in Section 2.3.1, the footpoint identity may change due to photospheric field evolution. Thus in order to make the result more robust, we choose larger areas P1L, N1L and N2L (the solid rectangular regions in Figure 2.12(a) and (d) which are chosen to accommodate similar structures in the photospheric vertical current density diagrams at 07:00 UT and 07:48 UT). We then study the connections between these three regions and P2, calculating all the field lines from P1L to N1L, P1L to N2L, P2 to N1L, and P2 to N2L. Comparing Figure 2.12(b) with Figure 2.12(e) shows that after the flare, the number of connections[2] between P1L and N1L decreases, but increases between P1L and N2L. Most of the disappearing connections are the flux rope field lines. In Figure 2.12(c) and (d), a similar situation happens with the area P2. The arm-like field lines from P2 to N2L disappear after the flare while the connectivities between P2 and N1L are considerably enhanced. These connectivity changes could be realised by the above proposed possible reconnection between the flux rope and the arm-like field lines. We quantify these changes using the method in Wiegelmann et al. (2013) to calculate the connected magnetic flux between these four regions at both times. In this method, the flux linking two sources is calculated as the mean of the values obtained taking each source in turn as the leading footpoint region, with the error given by the half of the difference of these values. Before the flare at 07:00 UT the magnetic flux between P1L and N1L is 585.3 ± 26.3 GWb, while after the flare at 07:48 UT it reduces to 192.8 ± 58.0 GWb. The flux between P2 and N2L also declines, from 336.5 ± 16.9 GWb before the flare to 302.2 ± 13.7 GWb after the flare (the reason for this small decrease $\sim 10\%$ might be that the arm-like field may only account for a small part of the entire connectivities between P2 and N2L, as can be seen by comparing the two insets in Figure 2.12(c) and (f), which could result in a relatively small percentage of the total magnetic flux between the two regions). However, the flux between P1L and N2L, and between P2 and N1L, are both enhanced after the flares, from 301.0 ± 46.2 GWb to 787.7 ± 97.5 GWb, and from 251.6 ± 55.7 GWb to 462.8 ± 66.2 GWb, respectively. These flux changes reflect that the connectivity

[2]The number of field lines is generally believed to be a non-physical quantity in a continuous magnetic field. However, as here the measured magnetogram is discrete and only one field line is plotted in one pixel of an area $\approx 0.5 \times 0.5$ arcsec, the number of field lines in this situation in fact reflects the bottom boundary area that contributes to the connection between the two regions.

between P1L and N1L and that between P2 and N2L are both reduced after the flare, whereas the connectivity between P1L and N2L and the one between P2 and N1L both increase. This could be resulted from the above proposed reconnection between the flux rope and the arm-like structure. This more robust argument increases the likelihood of this scenario.

2.4 Discussion

2.4.1 Evidence for the Implosion

The observed overlying arcade motion shown between "B" and "C" in Figure 2.6(b) is a contraction without obvious oscillations[3], consistent with a theoretical implosion evolution in which the reduction of magnetic pressure underneath the arcade is slow compared to the arcade loop oscillation period (see Figure 4(b) of Russell et al. (2015)). The evidence that this apparent contraction is a real implosion comes from three aspects.

(i) In Figure 2.6(b), the cyan dotted line between "B" and "C" shows that the arcade apparently contracts by about a half of its original projected height during this period (which can also be seen by comparing Figure 2.4(e) with (h)). An apparent contraction could also be due to a change in loop inclination from a face-on state. However, in this event, if the change were caused only by inclination of the arcade towards the solar disk, the arcade plane would need to incline by about 60° towards the solar disk in order to satisfy the observed contraction. As the event is close to the disk centre (see Figure 2.1), this is quite an unlikely situation (unless the arcade loops can submerge into the photosphere). Thus, inclination only could not account for the observed apparent contraction of the overlying arcade.

(ii) The two downwards-moving features between "B" and "C" in Figure 2.6(b) are nearly parallel to each other during ~ 4 mins. The simplest explanation is that during this period, as the overlying arcade moves as a whole, its individual loops mostly contract with similar speeds and no dramatic change in inclination

[3]The impression of oscillations in the 171 Å animation in Figure 2.4 might be caused by the gradual brightening of outer contracting loops, which may generate an illusion of the loops bouncing back.

(too much change in inclination would cause the two downwards-moving features to converge or diverge). The movement of the arcade in the 171 Å animation in Figure 2.4 after 07:22 UT ("B" in Figure 2.6(b)), which appears to be a moderate inclination superimposed on a major contraction, supports this explanation. Consecutive brightening of the arcade loops at constant projected distance within 4 mins could also give the appearance of the two parallel downwards-moving features, but this would be an unlikely coincidence.

(iii) Coronal magnetic field extrapolation provides us with further evidence. As illustrated in Figures 2.8 and 2.9, the lengths of the overlying arcade field lines are globally shifted to shorter values after the flare. The calculated average projected contraction of the higher and longer field lines of the extrapolated arcade is $\sim$ 4.7 arcsecs, which is in good agreement with the apparent net contraction $\sim$ 4.5 arcsecs seen in AIA 171 Å (indicated by the blue arrow in Figure 2.6(b)). In addition, Figure 2.10 shows that before the flare the arcade field line lengths are tending to lengthen, whereas after the flare the trend is decreasing and the global arcade field lengths decrease substantially without restoration for a long time. More compact field after flares has also been found in Sun et al. (2012) and Thalmann et al. (2016).

Even though reported magnetic field implosions are still rare, implosions could in fact happen frequently. Sometimes it may be their relatively small displacements in small flares, compared to nearly simultaneous violent eruptions or CMEs, that make them hard to recognise. As in our event, if it were not for the first expansion phase that inflates the overlying arcade, the final apparent net contraction $\sim$ 4.5 arcsecs would be relatively difficult to discover. However, as the released flare energy increases, implosion could be more noticeable, as in the M6.4 flare where a displacement of $\sim$ 25 arcsecs has been seen (Simões et al. 2013) and the X2.2 flare $\sim$ 40 arcsecs (Gosain 2012; Liu et al. 2012a; Sun et al. 2012). Moreover, Figure 2.13 implies that the maximum contraction speed may also correlate with the released energy level.

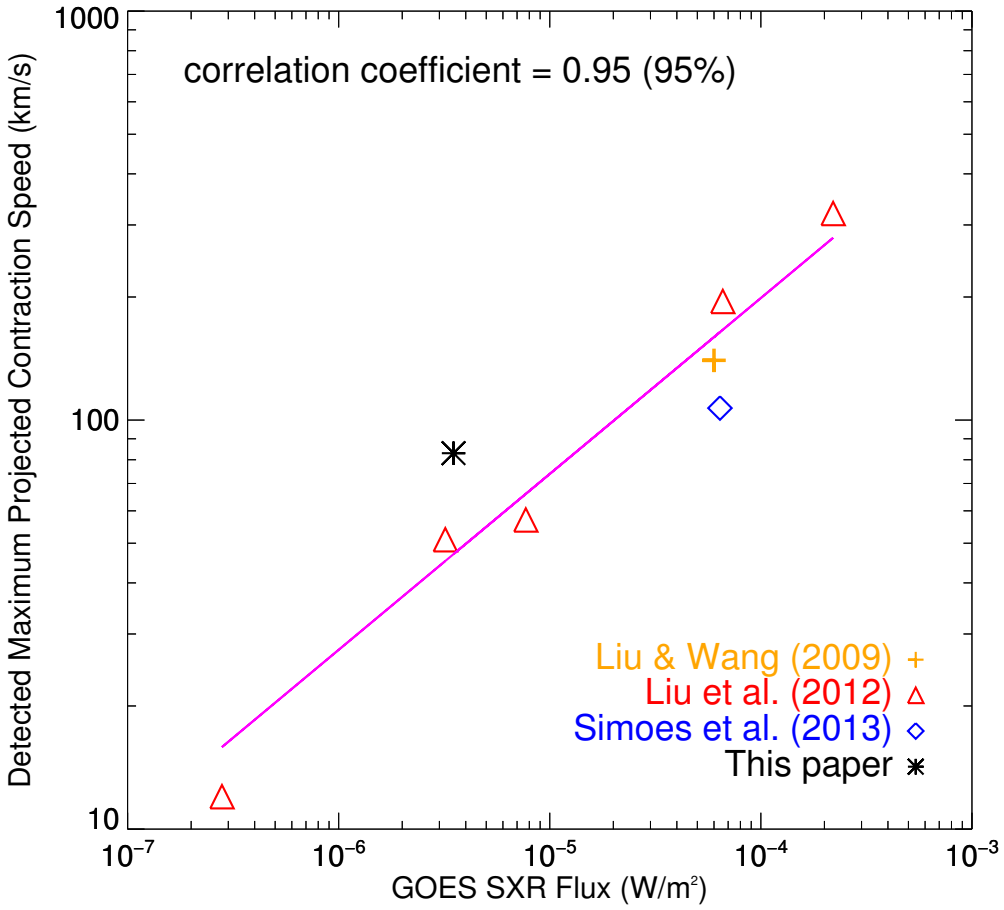

Figure 2.13: Correlation between the detected maximum projected contraction speed and the SXR flux for 8 disk AR flares, an updated version of Liu et al. (2012a). The magenta line represents the linear regression. The correlation coefficient is 0.95 with a 95% confidence level.

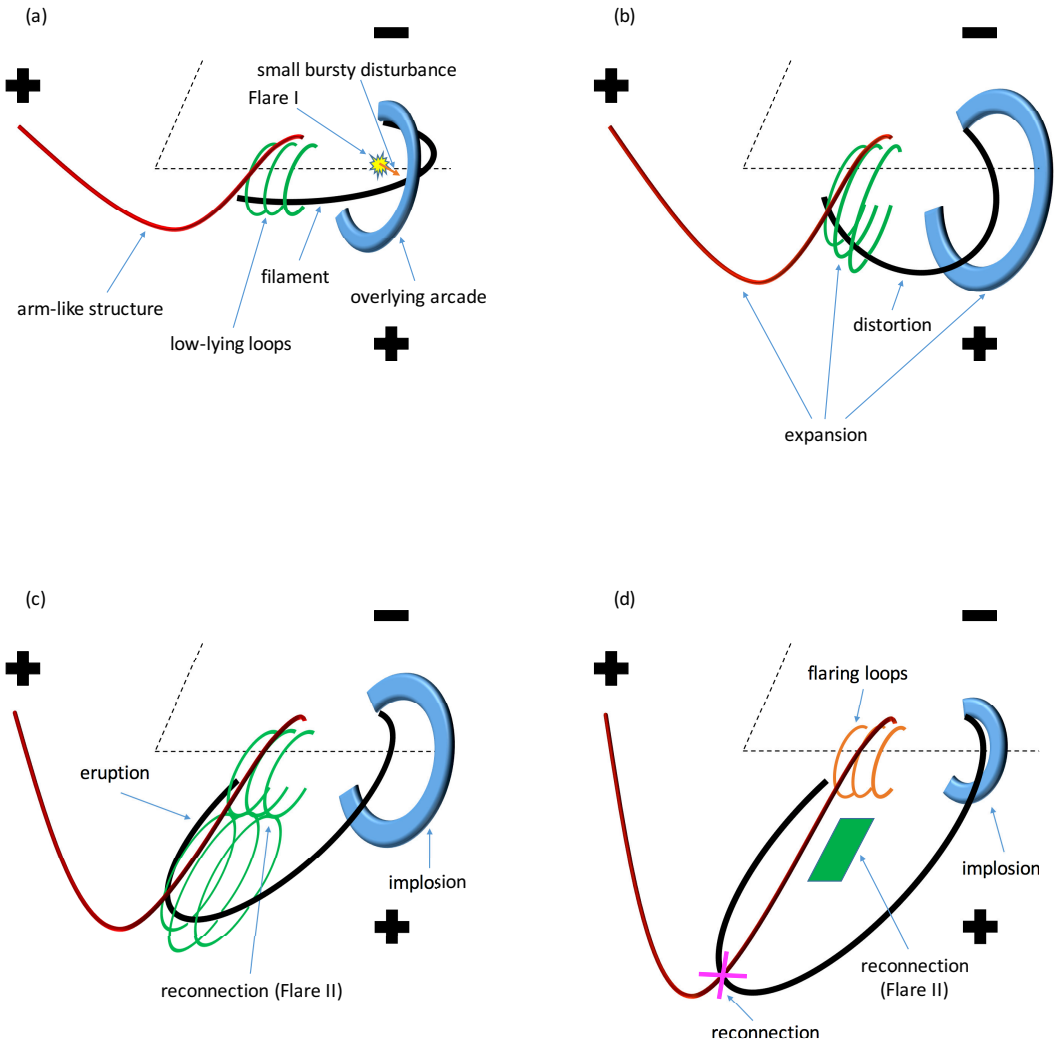

Figure 2.14: Cartoons show our understanding of the flare evolution. The large bold "+" and "-" signs in each image represent positive and negative polarity regions, respectively. (a) Flare I disturbs the filament's western part. (b) Filament distortion phase (with the overlying arcade expansion). (c) Filament eruption phase (with Flare II and the overlying arcade implosion). (d) Further eruption of the filament (with Flare II, the overlying arcade implosion, and the possible reconnection between the filament and the arm-like structure). The green rectangular region in (d) represents that there is still a current sheet reconnection beneath the erupting filament, like in (c), which is used to make the image easier to see.

2.4.2 Possible Scenario for the Overall Evolution

Table 2.1 shows that the observed evolution consists of four main processes: Flare I, the filament distortion and eruption, Flare II, and the overlying arcade expansion and contraction. As described in Section 2.2, they exhibit intimate relationships both in time and space. After synthesising the observations and extrapolation results in Section 2.2 and 2.3, in Figure 3.9 we illustrate our understanding of the event evolution, mainly in the framework of the metastable eruption model (Sturrock et al. 2001), the implosion conjecture (Hudson 2000), and the standard "CSHKP" model of two-ribbon flares (Carmichael 1964; Sturrock 1966; Hirayama 1974; Kopp & Pneuman 1976). Possibly due to the perturbation produced by Flare I, the initially metastable filament brightens and becomes unstable (Figure 2.14(a)). The overlying arcade restricts the filament from erupting, so it has to distort, with a bump propagating from west to east (Figure 2.14(b)) representing transport of free magnetic energy from an environment with a stronger surrounding field, to a weaker one. When the bump (free energy) propagates through the arcade plane, the arcade expands as a consequence (Figure 2.14(b)). As the bump propagates further to the east, the filament's eastern part suddenly erupts nonradially, possibly due to an ideal MHD instability (Figure 2.14(c)). This simultaneously causes the overlying arcade to contract according to the implosion conjecture, and Flare II to happen through reconnection (Figure 2.14(c)). As the filament continues to erupt, the arcade contracts further (Figure 2.14(d)). In the following, we will explain the scenario in more detail.

2.4.2.1 Scenario for Flare I, the Filament Distortion and Eruption, and Flare II

A twisted flux rope anchored below a magnetic arcade can stay in a metastable state, but following a large disturbance, e.g., produced by a nearby flare, could become unstable and rupture through the arcade, leading the system to a lower energy state (Sturrock et al. 2001). At the beginning of our event the magnetic system may be in a metastable state which is then disrupted, possibly by Flare I at the filament's western part (Figure 2.14(a) shown in Figure 2.3(b) and (c)). The disturbed and brightened western part of the filament is restrained against erupting outwards by the overlying arcade field. The filament instead distorts and a bump or bend in the field, which we associate with free energy, propagates from west to

east (Figure 2.14(b)) where the field is weaker as shown by extrapolations. As the free magnetic energy is transported through the arcade plane, the arcade is pushed upwards due to the enhanced underlying magnetic pressure. This could account for the synchronism of the start of expansion of the filament's eastern and western parts, and the overlying arcade at ~ 07:15:40 UT, revealed by the timeslices in Figure 2.6(a) and (b). As the bump propagates further, close to the filament's eastern footpoint, and sweeps across cut 1 and 2 of Figure 2.2(b) we expect that the filament's western part would contract while the eastern part expands, corresponding to their observed dynamics in Figure 2.6(a) and (b) between ~ 07:20 UT and 07:22 UT [4]. The arcade would meanwhile be pushed aside by the filament's western part, and incline more towards the solar disk. At the end of this distortion, the filament's western part also appears compressed (Figure 2.4(d)), possibly caused by the strong downward tension of the overlying arcade field in the west and the weaker confinement of the low-lying loops on the growing filament's bump in the east during the persistent distortion.

The dramatic acceleration and eruption of the filament's eastern part (Figure 2.14(c), corresponding to the observation at ~ 07:22 UT in Figure 2.4(e)) may be due to the torus instability (Kliem & Török 2006) because of the weaker magnetic field in the expanding eastern low-lying loops, or the kink instability (Sakurai 1976; Rust & Kumar 1996) due to squeezing of the filament, or both. The surrounding field could then be highly stretched to form a current sheet beneath the erupting filament producing Flare II, as in the standard "CSHKP" model of two-ribbon flares.

2.4.2.2 Scenario for the Overlying Arcade Contraction

When the filament erupts at ~ 07:22 UT, the overlying arcade contraction also starts immediately, shown in Figure 2.4(e) to (i). As demonstrated in Section 2.4.1, it is very likely to be a real implosion, due to reduced magnetic energy underneath the arcade. Russell et al. (2015) theoretically demonstrate three implosion types, with two having oscillations and the third not. In our event, as shown in Figure 2.6(b), no obvious oscillations have been detected, so it belongs to the "gradual energy release"

[4] Only the filament's western part tracked by cut 2 has a contraction between ~ 07:20 UT and 07:22 UT, while part of the bump still supports the overlying arcade during this time. This can explain the delay of the start of contraction of the overlying arcade at ~ 07:22 UT instead of ~ 07:20 UT, i.e., the asynchronism of the start of contraction of the overlying arcade and the filament western part in Figure 2.6(b).

situation (see Figure 4(b) of Russell et al. 2015) in which the underlying magnetic energy is released slowly compared to the loop's oscillation period. After carefully inspecting Figure 2.4(d) to (f) and the 171 Å animation in Figure 2.4 between ~ 07:21 UT to 07:25 UT, we propose two reasons why the energy release is gradual. Both reflect magnetic energy transfer out of the arcade plane.

(i) The filament erupting outwards from beneath the arcade would enhance the magnetic field to the east of the arcade, which creates a larger magnetic pressure that pushes the arcade to incline towards the solar disk. The relative positions of the filament and the arcade would change, and the interface between the filament's western end and the arcade's southern leg would gradually slip from in the arcade plane to above it (see Figure 2.14(b) to (d)), which means that the component of the magnetic pressure exerted by the filament's western leg in the loop plane would be gradually reduced.

(ii) As the filament stretches outwards, its magnetic energy is transformed into kinetic and gravitational energy of the erupting plasma (Schmieder et al. 2015). The magnetic energy per unit length would then decrease, manifested by reduced magnetic twist per unit length (see equation 2.2 of Sturrock et al. 2001). This can further reduce the component of the magnetic pressure parallel to the loop plane provided by the filament's western leg.

The timescale for these two effects could be such that the overlying loops do not oscillate. The final net contraction seen in both observation (Figure 2.6(b)) and extrapolation (Figure 2.8 and 2.9) means that finally the field underneath the arcade has a lower magnetic energy density/pressure.

The rapid contraction of the inner arcade loops occurs only during the rise of Flare II's impulsive phase (between "B" and "C" in Figure 2.6), as seen in other two events reported by Simões et al. (2013) (see its Figure 4), and by Gosain (2012) and Sun et al. (2012). This also indicates that the contraction is indeed not directly caused by the flare energy release/conversion, otherwise we would expect a comparable contraction in the declining part of the impulsive phase when the energy dissipated, as the energy content of non-thermal particles producing the HXR flux is comparable. However, the contraction is still related to the flare in that the impulsive phase is associated with the filament eruption out of the AR core.

2.4.2.3 Scenario for the Possible Filament Reconnection

As illustrated in Figure 2.5(d) and Figure 2.7, there is also an arm-like structure accompanying the filament eruption. The extrapolation results in Section 2.3.2 show that they could reconnect with each other and exchange their footpoints during the eruption process, to form a less sheared configuration (compare Figure 2.11(b) with (e)). The cartoon of Figure 2.14(d) illustrates this possible filament reconnection scenario (the exact reconnection location is uncertain). This could contribute to Flare II to some extent in the late erupting phase, but since the filament in the late erupting phase in 304 Å is too weak to track, it cannot be confirmed by the present observations. However, the reconnection of an erupting filament to a far distant area has been observed in 304 Å in another event by Filippov (2014) (especially see their movie 3, similar to our event). Li et al. (2016) have also recently reported an erupting filament reconnecting with a nearby coronal structure.

2.5 Conclusions

AIA observations and NLFFF extrapolations point to the well-observed contraction of the overlying arcade during the filament eruption in flare SOL20130619T07:29 being a real implosion rather than an inclination effect. We interpret the implosion as due to magnetic energy transfer out of the arcade plane in the filament eruption process rather than due to local magnetic energy dissipation in the flare. The final net contraction of the arcade reflects the permanent change of magnetic pressure underneath the arcade. This event implies that filament movement or eruption can make overlying field expand or erupt as observed in many events, but also is able to simultaneously implode peripheral or unopened overlying field due to reduced magnetic pressure underneath. This event appears to demonstrate one of the ways in 3D to open the overlying field without violating the Aly-Sturrock hypothesis, that is, "partial opening of the field", which allows the field to open in one part of the region and to implode in another.

The event is interesting in terms of the diversity of processes involved and their close relationships in space and time. The proposed scenario for its evolution has two main implications: (1) the uneven confinement of a filament by overlying field can force energy transfer through the region, with filament distortion preceding a

dramatic and probably asymmetric eruption through a "weak spot". To identify such locations, measures of the field confinement such as the decay index (e.g., Liu 2008) need to be examined from point to point in the AR. (2) an implosion of peripheral field can happen simultaneously with an eruption, helping us track the magnetic energy transfer through a flaring region. MHD simulations, as in Amari et al. (2014), might profitably be used to explore the field evolution, and probe the validity of these statements.

We have emphasised the overall magnetic evolution associated with the eruption and implosion, and have not explored other aspects, such as why the filament instability happens in the first place, or why the overlying arcade disappears in AIA wavebands after its implosion. Our main conclusion is that, in this event, we can successfully unify aspects of three main ways to understand coronal magnetic instabilities, namely the metastable eruption model, the implosion conjecture, and the standard "CSHKP" flare model, with the transfer of magnetic energy within the AR being central to the process.

Chapter 3

Unambiguous Evidence of Coronal Implosions

This work can be found in the publication Wang et al. (2018).

3.1 Introduction to the Chapter

Remarkable coronal loop contractions in extreme ultraviolet at the periphery of active regions, with speeds of tens to hundreds of km/s, were reported in Chapter 2 and in a few other events ranging from Geostationary Operational Environmental Satellite (GOES) class B to X (Liu & Wang 2009, 2010; Gosain 2012; Liu et al. 2012a; Sun et al. 2012; Simões et al. 2013; Yan et al. 2013; Kushwaha et al. 2015). As these peripheral loop contractions were always observed face-on and accompanied by eruptions from central magnetic structures (like a filament or an arcade eruption), the possibility could not be ruled out that apparent contraction is a projection effect due to inclination of the loop plane pushed by the erupting structure, rather than a real contraction (from our survey experience, loop inclining is indeed more commonly observed when the loops are viewed with an edge-on state at the solar limb, and even some of them do not have a restoration back to their original locations). As far as we know, only Petrie (2016) reported edge-on loop contractions in two active regions from the perspective of Solar TErrestrial RElations Observatory (STEREO) in 195 Å, but due to the short interval of the process and the long cadence (~ 5 min), the dynamics was not persistently revealed and not clear enough to be well studied. The argument that the contracting loops do not restore to their original

positions after the eruptions (Liu et al. 2012a; Gosain 2012), and evidence from NLFFF extrapolations in the work of Chapter 2 has been used to try to substantiate the reality of the contracting motion, but the doubt that it could be a projection effect can still not be completely excluded, and the ambiguity remains.

For the mechanism of apparent contraction of loops in the periphery of ARs, Zuccarello et al. (2017) and Dudík et al. (2017) proposed an alternative explanation in their simulation, using the analogy of vortices in the hydrodynamic situation (further discussed in Section 3.3.3), which is against the implosion idea of Hudson (2000).

In this work, to prove the reality of loop contractions in the global coronal dynamics, we present four events[1] with the continuously contracting loops in an almost edge-on geometry from the perspective of SDO/AIA, which are free from the ambiguity caused by the projection effects, also supplemented by contemporary observations from STEREO for examination. In the wider context of observations, simulations and theories, we argue that the implosion conjecture of Hudson (2000) is valid in interpreting these events. Furthermore, distinct properties of the events allow us to identify two physical categories of implosion. One type demonstrates a rapid contraction at the beginning of the flare impulsive phase, as magnetic free energy is removed rapidly by a filament eruption. The other type, which has no visible eruption, shows a continuous loop shrinkage during the entire flare impulsive phase which we suggest shows the ongoing conversion of magnetic free energy in a coronal volume. Corresponding scenarios are described, which can provide reasonable explanations for the observations. We also point out that implosions may be suppressed in cases when a heavily-mass-loaded filament is involved, possibly served as an alternative account for their observational rarity.

We will present direct evidence of continuous implosion phenomena, with the observations shown in Section 3.2. Based on the main observational properties, Section 3.3 will demonstrate the validity of the implosion conjecture, and categorize the observed implosions into two types, with corresponding models proposed. Conclusions are summarized in Section 3.4.

[1]The four events are selected after a survey of around tens of thousands of solar events by randomly examining animations using the tool ISolSearch at the website http://sdowww.lmsal.com/suntoday_v2/. Thus this is not a complete survey. We select the four events because they have more significant loop contractions and more favorable perspectives than the others, which are adequate for the purpose of this work.

3.2 Observations and Analyses

We select four events, SOL2011-09-14T16:26 (C4.2), SOL2014-02-17T23:15 (C1.9), SOL2016-04-08T01:56 (B8.3), and SOL2016-11-22T23:45 (B6.0), for analysis, which are located in active regions NOAA 11290 (S17W47), 11978 (N05W89), 12529 (N09E88), and 12612 (N11E89). Hereafter, for convenience, the four events are labelled as Event I, II, III, and IV, respectively. They are all observed by both Solar Dynamics Observatory/Atmospheric Imaging Assembly (SDO/AIA) and STEREO A. The contracting arcades in these four events all have an almost edge-on geometry from the perspective of AIA, so the contributions to the loop dynamics from contraction and inclination can be clearly disentangled. The contracting loops observed by STEREO A in 195 Å are very likely the same as that viewed from AIA in 193 Å (for Event IV the contracting structures in 171 Å are similar to that in 193 Å), because these two wave bands share similar observing temperature $\sim 1.5 \times 10^6$ K. AIA images and photospheric magnetograms from Helioseismic and Magnetic Imager (HMI) for Event I have been processed by the standard software (Boerner et al. 2012), and supplementary images from STEREO A via secchi_prep.pro (Howard et al. 2008).

3.2.1 Event I: SOL2011-09-14T16:26

Event I is shown in Figure 3.1 and the accompanying animation, with both AIA and STEREO A observations. AIA observes the contracting arcade (hereafter we call it arcade I) from the side with a nearly horizontal geometry (Figure 3.1(a) and (b)), while STEREO A looks at it from the top with the loop plane having $\sim 45°$ with respect to the line of sight (Figure 3.1(e)). A filament is located low in the corona (Figure 3.1(c)). As it is destabilised and erupts outward (Figure 3.1(f)), another arcade structure (hereafter arcade II) passes from beneath arcade I and erupts (Figure 3.1(b)). Meanwhile, arcade I contracts towards the space left by the erupting filament and arcade II. The motion of contraction is unambiguous, which is evidenced by the accompanied animation. Oscillation follows and finally most of the loops of arcade I disappear.

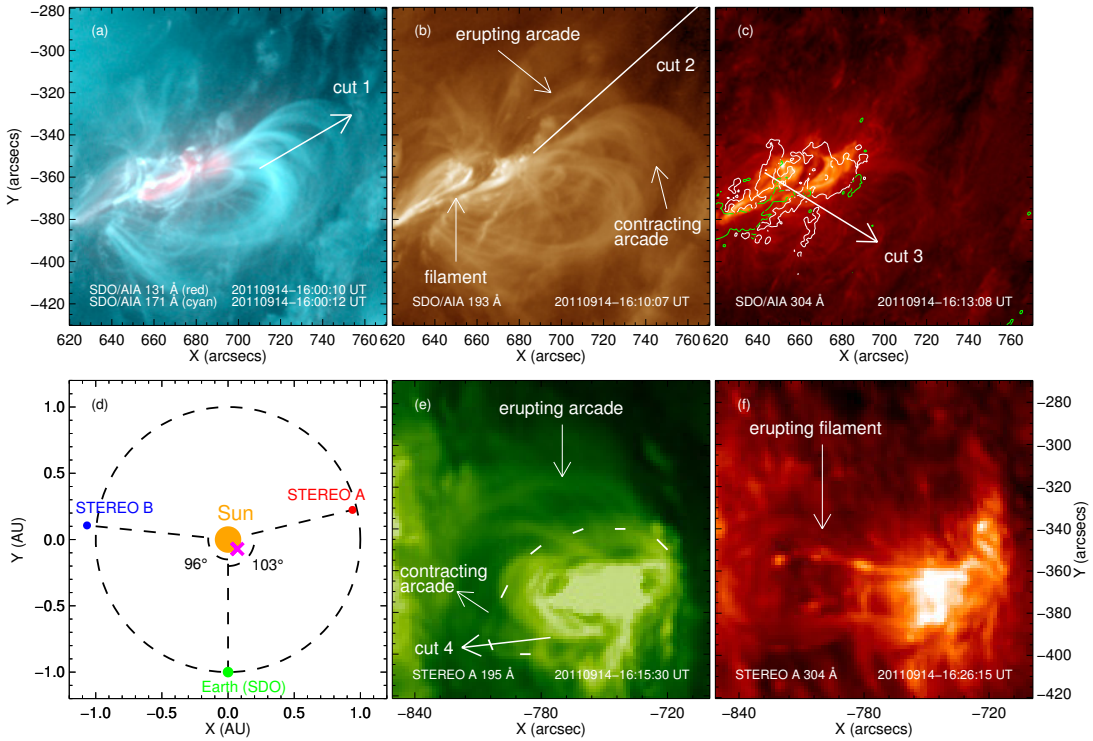

Figure 3.1: Images for Event I: SOL2011-09-14T16:26. (a)-(c) observed from the perspective of AIA. 131 Å is red, and 171 Å cyan in (a) (hereafter for composite images, cyan always represents a low temperature band, like 171 or 193 Å, and the hot 131 Å is always set to red). (d) relative positions of SDO and STEREO. The magenta cross shows the longitudinal position of the event. (e)-(f) observed from the perspective of STEREO A. The dashed line in (e) illustrates the location and shape of the contracting arcade. Cuts 1-4 are used for the timeslices in Figure 3.2. The arrowhead of cut 2 is beyond the image edge. An animation of this figure is available in Wang et al. (2018) at the link http://iopscience.iop.org/article/10.3847/1538-4357/aabcoe/meta.

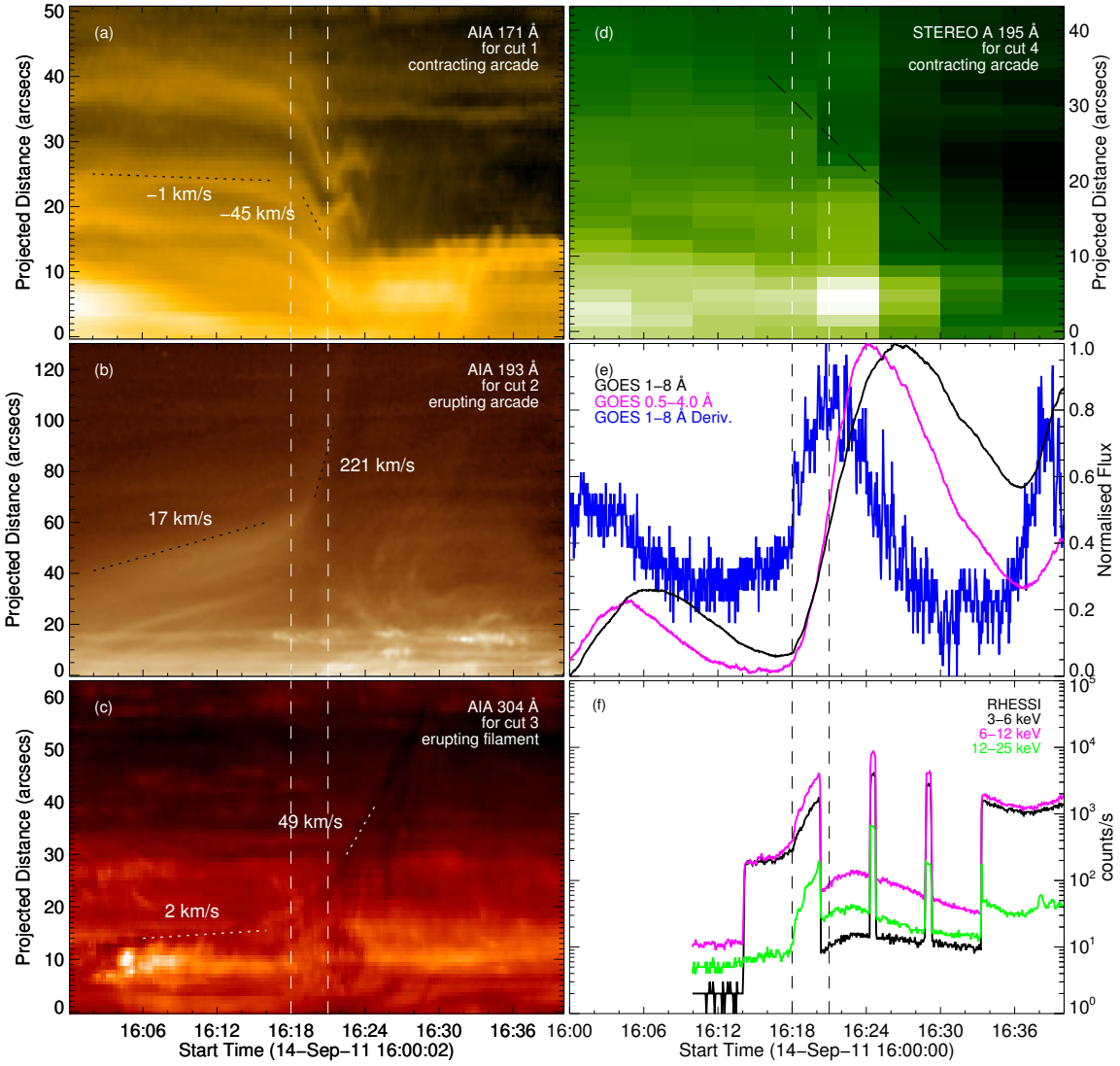

Figure 3.2: Evolution of Event I. (a)-(d) Timeslices for dynamic features in Event I. The sampling time of STEREO A 195 Å in (d) starts from the beginning of each timeslice, with an exposure duration ~ 8 s, and the long-dashed line shows the rough contraction trend but means an uncertain contraction speed because of the long sampling cadence ~ 5 min and few sampling points. (e)-(f) GOES and RHESSI light curves, respectively. The two vertical dashed lines across the figure shows the time interval of the arcade contraction.

Figure 3.2(a)-(d) show the timeslices created along the cuts 1-4 chosen in Figure 3.1, respectively, presenting the detailed dynamics of the corresponding features

along the cuts. The major contraction of arcade I (in the interval between the two dashed lines) starts as the filament and arcade II erupt, though they already have similar but weaker behaviours before this time interval. This major contraction interval also corresponds to the rise of the impulsive phase, which is illustrated by the GOES 1-8 Å derivative in Figure 3.2(e) and the light curve of RHESSI 12-25 keV in Figure 3.2(f). After the major contraction, the loops of arcade I oscillate and most of them disappear (Figure 3.2(a)), though the filament and arcade II still continue to move outward rapidly(Figure 3.2(b) and (c)). We note that the contraction speed of arcade I is always much smaller than the eruption speeds of arcade II and also the filament. The filament eruption speed is underestimated in Figure 3.2 because of projection, and can be more accurately estimated to be ~ 150 km s^{-1}, by considering the time interval between 16:18:00 UT (the start time of the filament eruption from Figure 3.2(c)) and 16:26:15 UT (Figure 3.1(f)), and the travel distance ~ 100 arcsecs in Figure 3.1(f). The final contraction distance of arcade I is also much smaller than the final eruption distances of the filament and arcade II.

3.2.2 Event II: SOL2014-02-17T23:15

Figures 3.3 and 3.4 are constructed similarly to Figures 3.1 and 3.2, respectively. Event II is located on the limb with a more favourable perspective, making the contraction of the arcade clearer. Seen from the accompanying animation, first the filament lies close to the solar surface, with the arcade overlying its northern end. Then they expand upward simultaneously up to around 23:05 UT (Figure 3.3(a)). As the filament starts to writhe along with its southwestward eruption (Figure 3.3(b)), the arcade begins to contract and the northern end of the filament seems to be pushed downward to the solar surface. In the end the arcade oscillates and gradually disappears.

Similar to Event I, the major arcade contraction coincides with the beginning of the filament eruption and the rise stage of the impulsive phase, and the arcade contracts more slowly and over a much smaller distance than the filament erupts (Figure 3.4). Event II differs from Event I in that before the major contraction, the arcade in Event II shows slow expansion rather than slow contraction as in Event I.

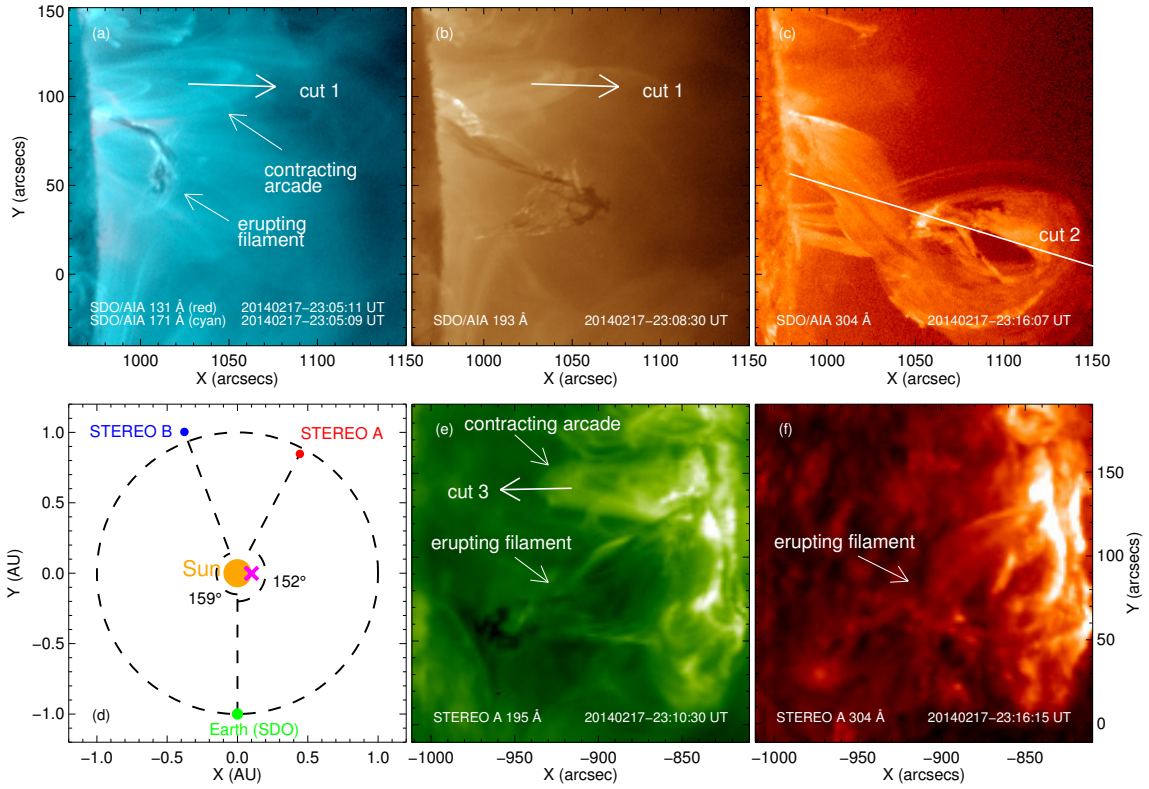

Figure 3.3: Images for Event II SOL2014-02-17T23:15. (a)-(c) observed from the perspective of AIA. 131 Å is red, and 171 Å cyan in (a). (d) relative positions of SDO and STEREO. The magenta cross shows the longitudinal position of the event. (e)-(f) observed from the perspective of STEREO A. Cuts 1-3 are used for the timeslices in Figure 3.4. The arrowhead of cut 2 is beyond the image edge. An animation of this figure is available in Wang et al. (2018) at the link http://iopscience.iop.org/article/10.3847/1538-4357/aabcoe/meta.

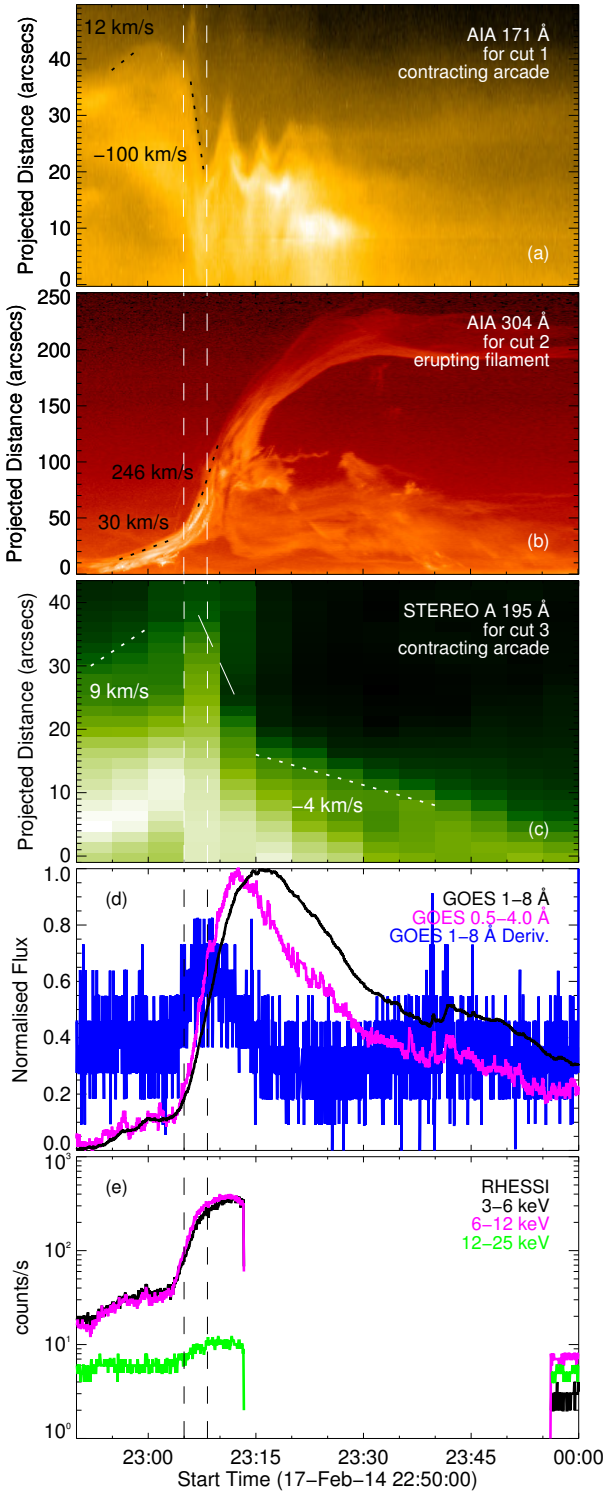

Figure 3.4: Evolution of Event II. (a)-(c) Timeslices for dynamic features in Event II. The sampling time of STEREO A 195 Å in (C) starts from the beginning of each timeslice, with an exposure duration ~ 8 s, and the long-dashed line shows the rough contraction trend but means an uncertain contraction speed because of the long sampling cadence ~ 5 min and few sampling points. (d)-(e) GOES and RHESSI light curves, respectively. The two vertical dashed lines across the figure shows the time interval of the arcade contraction.

3.2.3 Event III: SOL2016-04-08T01:56

AIA and STEREO A observe the contracting arcade in Event III from opposite sides (Figure 3.5(a), (b) and (e)). The arcade contracts as a flare underneath happens (Figure 3.5(b)). Strangely, neither AIA nor STEREO observations, which together have a wide temperature coverage (including cool 304 Å, warm 171 , 193 and 195 Å, and hot 131 Å) show any signature of violent arcade or filament eruptions as seen in Event I and II. There is only another arcade in the south expanding outward to a small extent (Figure 3.5(b)). The arcade in the north fades into the flaring region at the end with no obvious oscillation detected.

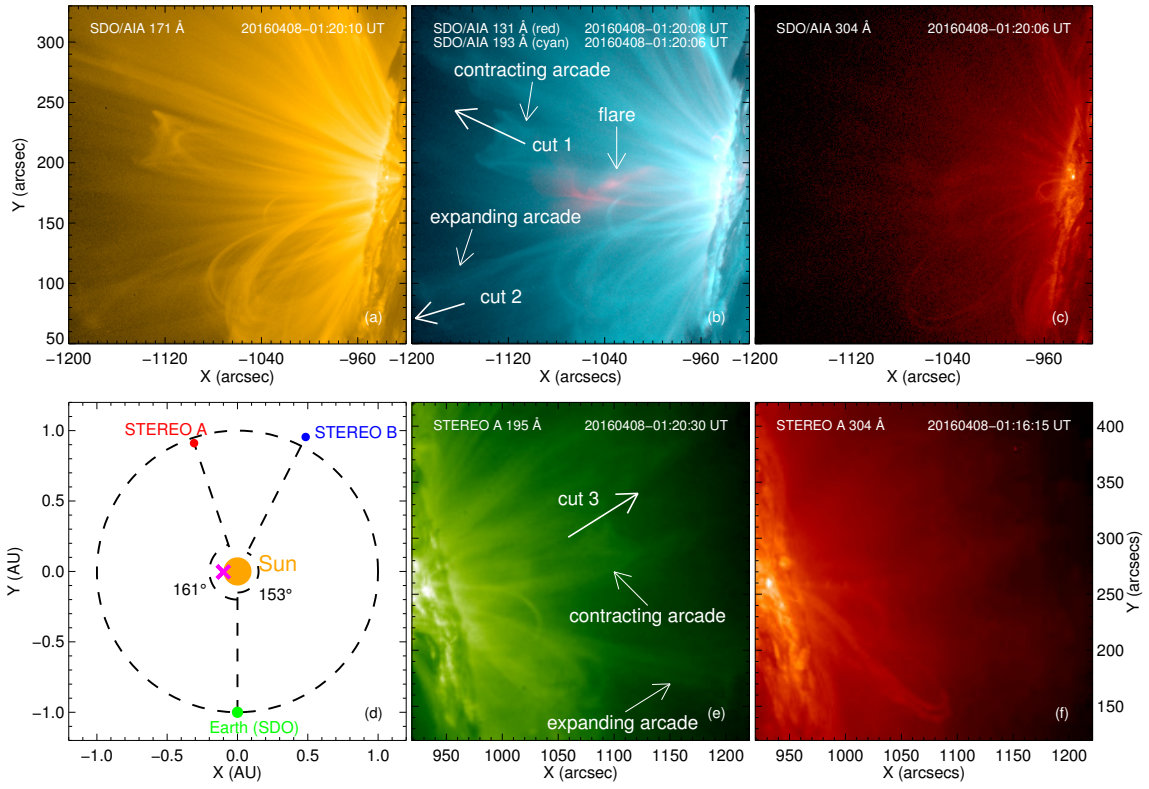

Figure 3.5: Images for Event III SOL2016-04-08T01:56 B8.3. (a)-(c) observed from the perspective of AIA. 131 Å is red, and 193 Å cyan in (b). (d) relative positions of SDO and STEREO. The magenta cross shows the longitudinal position of the event. (e)-(f) observed from the perspective of STEREO A. Cuts 1-3 are used for the time-slices in Figure 3.6. An animation of this figure is available in Wang et al. (2018) at the link http://iopscience.iop.org/article/10.3847/1538-4357/aabcoe/meta.

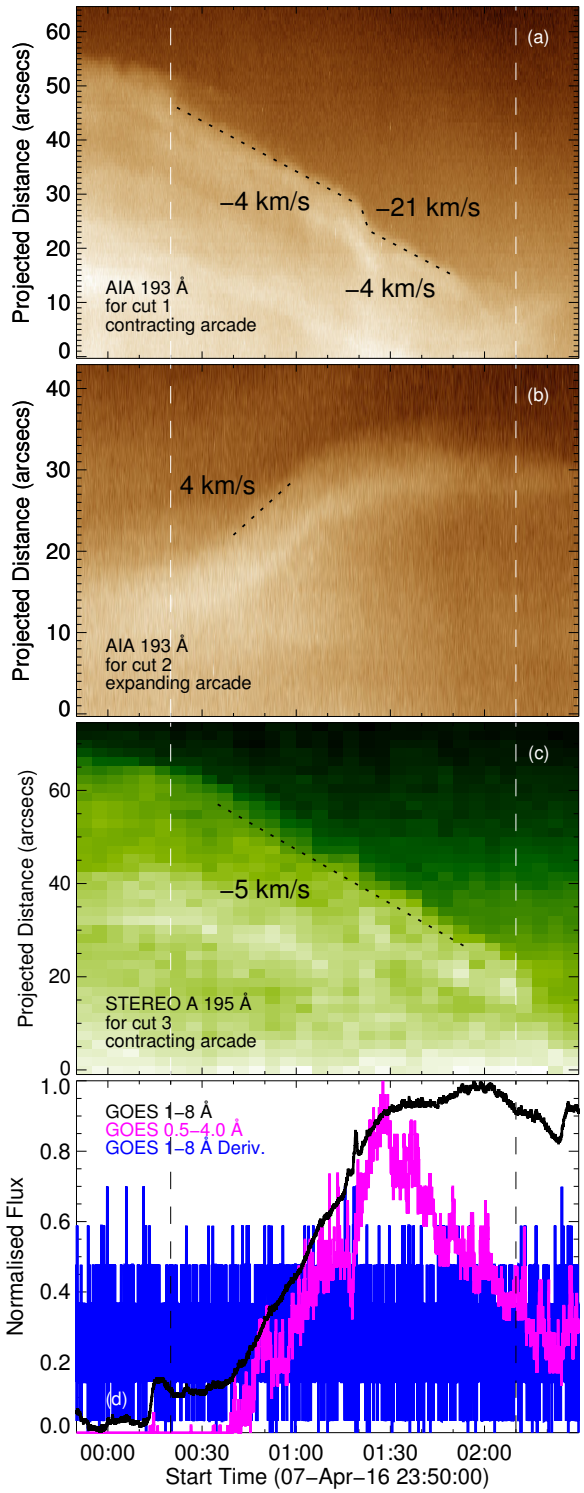

Figure 3.6: Evolution of Event III. (a)-(c) Timeslices for dynamic features in event III. The sampling time of STEREO A 195 Å in (C) starts from the beginning of each timeslice, with an exposure duration ~ 8 s. (d) GOES light curves. The two vertical dashed lines across the figure shows the time interval of the arcade contraction.

Figure 3.6(a) shows that the speed of the long-duration arcade contraction is only a few km s^{-1}, which is slow but real, rather than caused by solar rotation, because there are surrounding static loops as a reference (see the accompanying animation). And interestingly, an abrupt acceleration in the contraction occurs at around 01:20 UT, which coincides with a sudden increase or a spike in GOES 1-8 Å light curve (Figure 3.6(d)). It seems that the contraction of the arcade is quite sensitive to the flare. Though the Neupert effect is not notable here, the contraction process has already continued past the peak of the GOES 1-8 Å flux, which means that the arcade contraction spans the entire impulsive phase. This is unlike the situations in Events I and II where the contraction is localized in time to the rise of the impulsive phase. The expansion speed of the arcade in the south is also very small (Figure 3.6(b)), comparable to the contraction speed of the arcade in the north, but it only persists for about half of the contraction interval, which results in an expansion distance of around half of the contraction distance.

3.2.4 Event IV: SOL2016-11-22T23:45

In Event IV, AIA observes two contracting arcade systems with an edge-on geometry (Figure 3.7(a) and accompanied animation). Unlike the situation in Zuccarello et al. (2017) where the two peripheral arcades first diverge from each other and then contract, these arcades here directly converge towards each other and contract at the same time (Figure 3.7(b)). As they do so, it seems that two flare regions from two sides approach to the convergence location, which may imply that magnetic energy is released gradually towards the central core region. From STEREO A, we also detect the arcade contraction, with a face-on geometry (Figure 3.7(e)). The final disappearance of the contracting arcades is also found here without notable oscillation. Similar to Event III, there are no violent arcade or filament eruptions observed by the two instruments, but only a minor arcade expansion in AIA (Figure 3.7(b)). From the animation, it appears that this small expansion might be associated with a very weak invisible flux rope erupting outward, or it could also be field line opening due to magnetic reconnection.

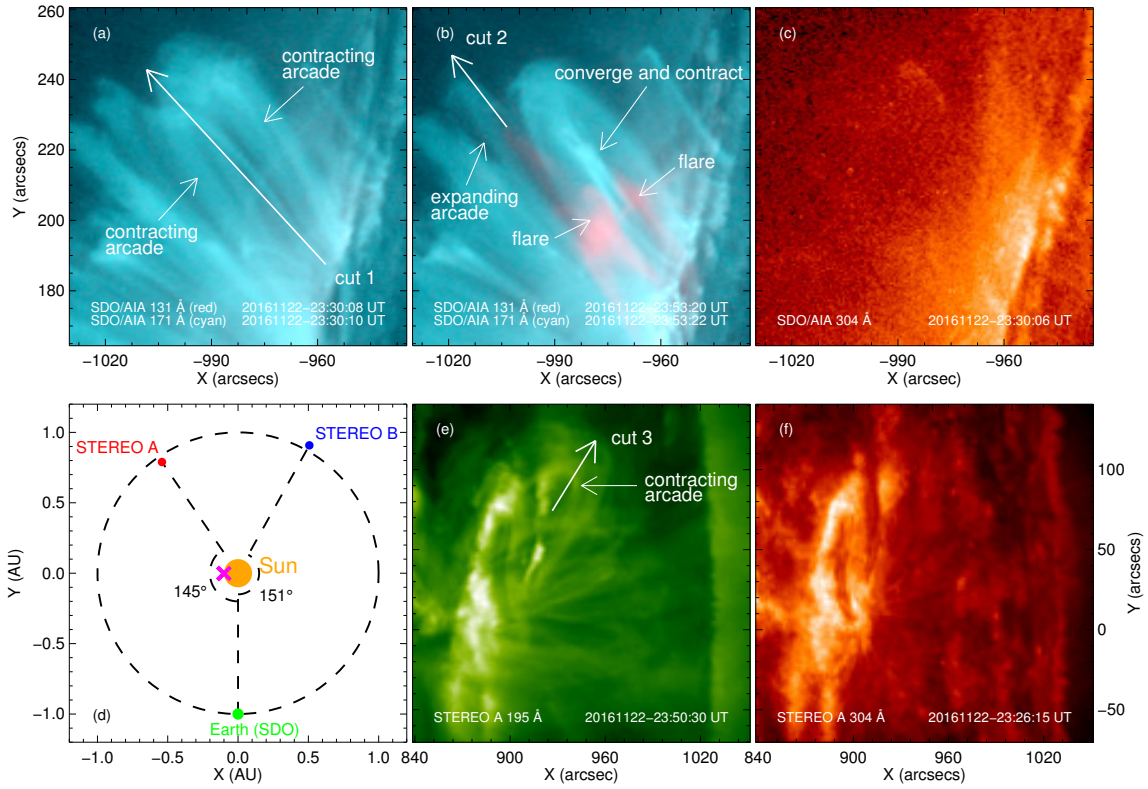

Figure 3.7: Images for Event IV SOL2016-11-22T23:45 B6.0. (a)-(c) observed from the perspective of AIA. 131 Å is red, and 171 Å cyan in (a) and (b). (d) relative positions of SDO and STEREO. The magenta cross shows the longitudinal position of the event. (e)-(f) observed from the perspective of STEREO A. Cuts 1-3 are used for the timeslices in Figure 3.8. An animation of this figure is available in Wang et al. (2018) at the link http://iopscience.iop.org/article/10.3847/1538-4357/aabcoe/meta.

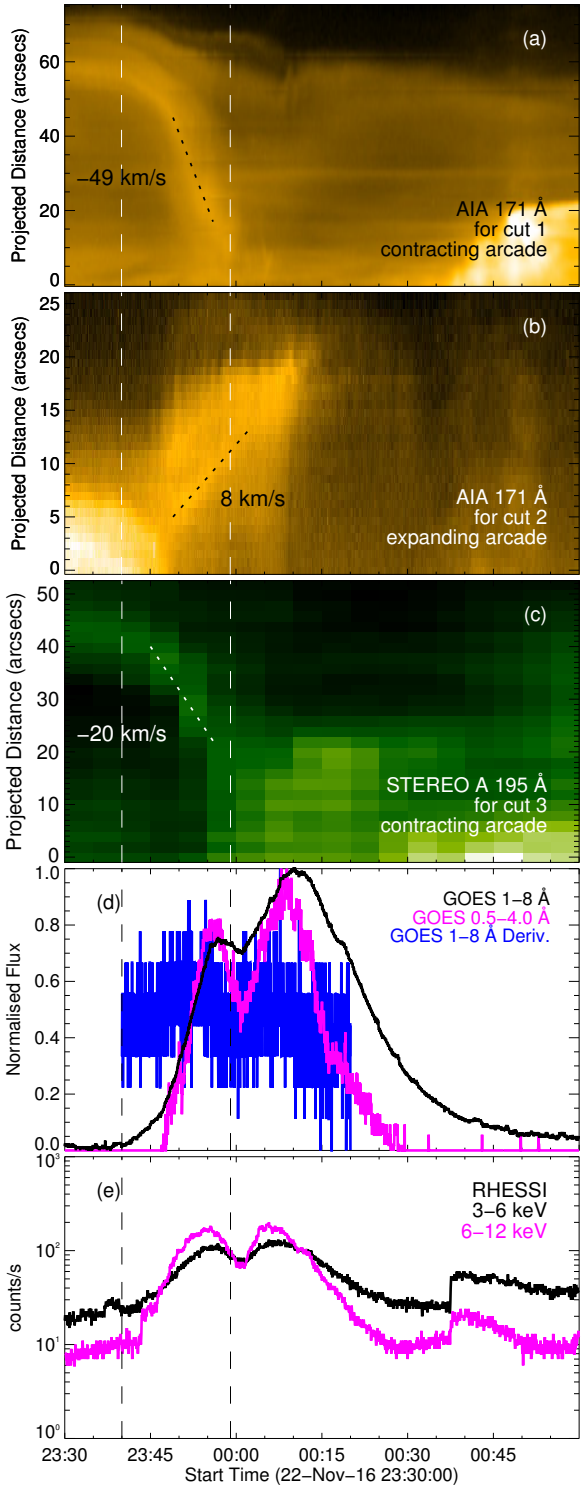

Figure 3.8: Evolution of Event IV. (a)-(c) Timeslices for dynamic features in event IV. The sampling time of STEREO A 195 Å in (C) starts from the beginning of each timeslice, with an exposure duration ~ 8 s. (d)-(e) GOES and RHESSI light curves, respectively. The two vertical dashed lines across the figure shows the time interval of the arcade contraction.

Different from Events I and II, the arcade contraction speed in this event is much larger than the expansion speed (Figure 3.8(a) and (b)). More similarities are found between Events III and IV. The contraction distance is much larger than the expansion distance, and it also happens during the entire impulsive phase (Figure 3.8(d) and (e)).

3.3 Discussion

3.3.1 Observational Characteristics

The apparent contracting loops observed from the perspective of SDO/AIA for these four events are in an almost edge-on state, and we believe that the main contributing factor for the motion is real contraction of loops. It seems unlikely that they could not be tall and narrow loops seen face-on, otherwise the pointed cusp would drag the loop to contract under magnetic tension force even before the event happens, which is not the case in observations. And due to the edge-on property, we can easily exclude the possibility of significant loop inclining perpendicular to its plane, though minor changes in inclination can be observed (especially in Events I and II). Then as large-scale peripheral loops usually have a dipole geometry and could not incline in the loops' plane (even though in some cases they could incline to some extent due to the impact of nearby erupting structures, they would restore to their original positions after the eruption completes, which is not observed here, especially in non-eruptive Events III and IV), the loop inclining in its plane can also be excluded. The last option left to explain the apparent contraction seems to be a real and major contraction of the loops.

Table 3.1 summarises the relevant information about the four selected events on the large scale. We concentrate on their eruptiveness, dynamic timing, distance and speed, which can separately reflect the onset, duration, total amount and rate of associated energy change. Both Events I and II exhibit violent filament (or arcade) eruptions in close proximity to the contracting arcades (Figures 3.1(b) and 3.3(a)), whereas there are only small expansions of arcades (or at most signatures of very weak, invisible flux rope eruptions) during the arcade contractions for Event III and IV (Figures 3.5(b) and 3.7(b)). The arcades in Event I and II mainly contract at the rise stage of the impulsive phase. By contrast, the arcade contractions respond to

their entire impulsive phases in Events III and IV.

Table 3.1: Focused large-scale properties of the uour selected events.

	SOL2011-09-14T16:26 Event I	SOL2014-02-17T23:15 Event II	SOL2016-04-08T01:56 Event III	SOL2016-11-22T23:45 Event IV
Eruptiveness	possess visible, significant filament (or arcade) eruptions		only have small and weak arcade expansions; no obvious filament (or arcade) eruptions	
Timing	mainly contract during the rise stage of the impulsive phase		contract during the entire impulsive phase	
Distance	arcade contraction distance (Event I: $\sim$ 10 arcsec; Event II: $\sim$ 20 arcsec) is much smaller than filament (or arcade) eruption distance (Event I: $>$ 70 arcsec; Event II: $\sim$ 200 arcsec)		arcade contraction distance (Event III: $\sim$ 40 arcsec; Event IV: $\sim$ 45 arcsec) is much larger than arcade expansion distance (Event III: $\sim$ 15 arcsec; Event IV: $\sim$ 15 arcsec)	
Speed	arcade contraction speed (Event I: $\sim$ 45 km s^{-1}; Event II: $\sim$ 100 km s^{-1}) is much smaller than filament (or arcade) eruption speed (Event I: $\sim$ 221 km s^{-1}; Event II: $\sim$ 246 km s^{-1})		arcade contraction speed (Event III: $\sim$ 5 km s^{-1}; Event IV: $\sim$ 49 km s^{-1}) is comparable to, or much larger than arcade expansion speed (Event III: $\sim$ 4 km s^{-1}; Event IV: $\sim$ 8 km s^{-1})	
Possible Origin	eruption-driven implosions		flare-driven implosions	

Note that for Events III and IV, the expanding structures could incline toward or away from SDO, resulting in underestimations of their travelling distances and speeds, but from the accompanied animations and geometry, it seems that they do not incline too much. If we assume the inclination angle to be a characteristic value $\sim 45°$, the conclusions here still hold, not to mention that the contracting structures could not be in the sky plane as well.

In terms of dynamic timing, distance and speed, Events I and II show the typical characteristics of eruptive flares, with eruption processes prominent in the large-scale dynamics, though the vast majority of eruptive flares are not accompanied by observed arcade contractions like those reported here. Events III and IV seem to have the opposite trend as the arcade contraction process dominates over the expansion/eruption on the large scale. This new type of coronal evolution may present a great challenge to eruptive flare models, like the "CSHKP" standard

model (Carmichael 1964; Sturrock 1966; Hirayama 1974; Kopp & Pneuman 1976) or breakout model (Antiochos et al. 1999; Aulanier et al. 2000).

3.3.2 Underlying Physics

What is the physics behind these arcade contraction phenomena? And what causes them to show the two different categories above in Table 3.1? The implosion conjecture proposed by Hudson (2000) provides a possible explanation. In his original paper, it was realised that both eruptions and flares as two main approaches to release magnetic energy stored in the corona could cause implosions. As eruptions and flares may involve different evolutionary time scales and large-scale dynamics, naturally we would expect to detect two kinds of implosion processes separately associated with them, characterised by different properties. This analysis raises a likely interpretation of the two kinds of arcade contraction behaviours observed, i.e., eruption-driven implosions and flare-driven implosions.

The distinctions between these events in Table 3.1 seem to match this expectation. Violent filament (or arcade) eruptions are seen in Events I and II, dynamically related with the arcade contractions, which may indicate them as eruption-driven implosions. On the contrary, with no such noticeable large-scale eruptions and only flares detected, Events III and IV may represent flare-driven implosions. Supporting evidence comes from the time range during which the contraction happens. In Events III and IV, the arcades contract during the entire impulsive phase, which is expected from the flare-driven scenario, because the flares continually release coronal magnetic energy and reduce the corresponding pressure. However, in Events I and II the major contractions only occur before the peak (or during the rise stage) of the impulsive phase, even though the flares still continue to liberate significant energy in the rest of the impulsive phase. This thus reflects there could be a different source responsible for the contraction. This could be the associated filament (or arcade) eruptions, as the escape time from the innermost core regions could be shorter than the flare duration. Since in a few well-observed events (Sun et al. 2012; Simões et al. 2013; Wang et al. 2016, and Events I and II here) we notice that the inner loops, closer to the core region, stop contracting almost at the peak of the impulsive phase, we suggest that it is around this time that the filament escapes from the innermost core region. In the spirit of this argument, the much slower contraction

after the major contraction of Event II (Figure 3.4(c)) might be interpreted as caused by the ongoing flare just underneath the contracting arcade (see Figure 3.3 and accompanying animation). The dominance in distance and speed of the eruptions in Events I and II is in accordance with the expectation of the arcade contractions being merely an auxiliary in the global dynamics, whereas the contractions are much more prominent on the large scale than the expansions/eruptions in Events III and IV, supporting a different triggering source, which could be the flares. Especially, the coincidence of the abrupt acceleration of the contraction and the spike in GOES 1-8 Å flux at ~ 01:20 UT in Event III (Figure 3.6) implies a close connection between these two phenomena.

3.3.3 Models

Figure 3.9 illustrates our understanding of these four events exploiting the implosion conjecture. Figure 3.9(a)-(b) and Figure 3.9(c)-(d) describe the field evolution of Events I and II, respectively. As argued above, Events I and II are of eruption-type, thus possessing similar essential dynamic characteristics, i.e., when the underlying filament erupts outward, the peripheral overlying arcade contracts. This scenario is also used to interpret the event in Wang et al. (2016). The basic idea is that filament (or arcade) field redistribution, and/or conversion of its energy to kinetic and gravitational energy, can locally reduce magnetic energy and pressure in its original position, resulting in forces in the periphery being unbalanced and the associated loops contracting. Another interesting explanation by Zuccarello et al. (2017) and Dudík et al. (2017) is that the eruption and contraction in this MHD situation are an analog of a fast flow creating vortices in its surroundings in hydrodynamics. However, due to the preferable perspectives here, we see that, in Event I (Figure 3.1 and accompanying animation) arcade I just adjacent to arcade II contracts directly when arcade II erupts, without the significant initial expansion and inclination phases that are expected in the vortex-flow scenario (Dudík et al. 2017). And in Event II the arcade only shows an arc-like flow rather than a complete vortex trajectory in the hydrodynamic situation, which is also illustrated in Figure 3.9(d). In theory, the viscous term in the invoked momentum equation (Zuccarello et al. 2015; Aulanier et al. 2005) of the simulation performed by Zuccarello et al. (2017) and Dudík et al. (2017) is much smaller than the Lorentz force in a low β coronal MHD environment. Thus,

the viscosity, which is responsible for vortex generation in the hydrodynamic case, would not be able to create the large-scale organised rapid contraction behaviours, though it might produce small-scale vortices around the erupting structure. The large-scale dynamics is controlled by the dominant Lorentz force. Zuccarello et al. (2017) argued that it is the enhanced magnetic tension, one component of the Lorentz force, caused by compressional Alfvén waves originating from the erupting field, that generates the contraction flow, but according to this argument, the contracting loops are expected to restore to their original locations after the filament (or arcade) erupts completely because of the nature of waves, which does not agree with the reported observations in which the loops remain at lower altitudes. Similarly, if the contracting motion was only caused by enhanced magnetic pressure (the other component of the Lorentz force) above the loops due to the erupting structure, we would also expect their restoration when the eruption terminates, not conforming to the observations either.

The final idea then resorts to reduced magnetic pressure underneath, which is just the core idea of the implosion conjecture. In fact, the arc-like flow in Figure 3.9(d) can be easily explained in this framework. As the filament erupts outward, the magnetic pressure is enhanced at higher altitude and reduced at lower altitude, which would naturally induce an arc-like flow of peripheral unopened arcade field around the central erupting structure because of pressure difference compared to the previous equilibrium state. Depending on the detailed topology and eruption process, the arc-like flow may not be so obvious in some cases, like Event I here; and the loops located at lower altitudes where they are not severely impacted by the high-pressure erupting structure could also contract directly, e.g., the event in Simões et al. (2013). The perturbation in the pressure should propagate outward with a limited speed, as observed by Simões et al. (2013) in a face-on geometry. This could be the fast-mode speed ($\sim$ Alfv́en speed v_A if plasma $\beta \ll 1$ as in the corona).

Particularly, there is strong observational evidence that Events III and IV do not show violent eruptions and vortex-like or even arc-like flows. The arcade in Event III contracts directly, and the two arcades of Event IV even converge towards each other and simultaneously contract downward. The contractions are significantly different from peripheral vortices created by a central fast flow in hydrodynamics, and thus cannot be explained by the analogy. Instead, the implosion conjecture (Hudson 2000) is able to account for these two events, in terms of flare-driven implosions, without

the need for eruptions. This has already been supported by the distinct properties of Events III and IV in Table 3.1, as argued above. Because of a mix of difficulties from limb location, structure overlapping in an edge-on geometry, and low contrast, the 3D field topologies of Events III and IV are not readily reconstructed. However, we propose a general model for them to interpret the major contractions and minor expansions observed, based on the implosion conjecture. Figure 3.9(e)-(f) illustrate the basic idea. The "black box" underlying the two arcade systems represents the core region where a flare occurs. During the flare the total magnetic energy and pressure are reduced within the entire "black box". However, there could exist a situation where the field energy underneath arcade III decreases and that underneath arcade IV increases, but the increase under arcade IV is smaller than the decrease under arcade III. Then we would expect to see that the contraction of arcade III is larger in extent and faster in speed than the expansion of arcade IV, which would then be in agreement with the properties of Events III and IV in Table 3.1. However, the detailed field reconnection process, corresponding topology change and energy transport and dissipation in the "black box" are unclear . The magnetic energy enhancement underneath arcade IV might be due to more closed field formed or field opening there through reconnection between the two domains under the two arcade systems. Such a model of flare-driven implosions is attractive and can reproduce the observations in a general way, but another possibility, which cannot be completely excluded, is that a small and invisible flux tube may continuously transport from under arcade III toward arcade IV, in the spirit of eruption-type implosions but a very weak one.

3.3.4 Unsuccessful Implosion

It is worth noting that well-observed implosions, either face-on or edge-on remain rather rare, whereas the implosion conjecture implies that they should be present in all solar energy-releasing events, including eruptions and flares. This is probably because of unfavourable viewing, complexity of active region field and involved reconnection processes (Liu & Wang 2010), or relatively small expected movements in readily observed peripheral loops when relatively small fraction of active region energy is released in the core region in a flare.

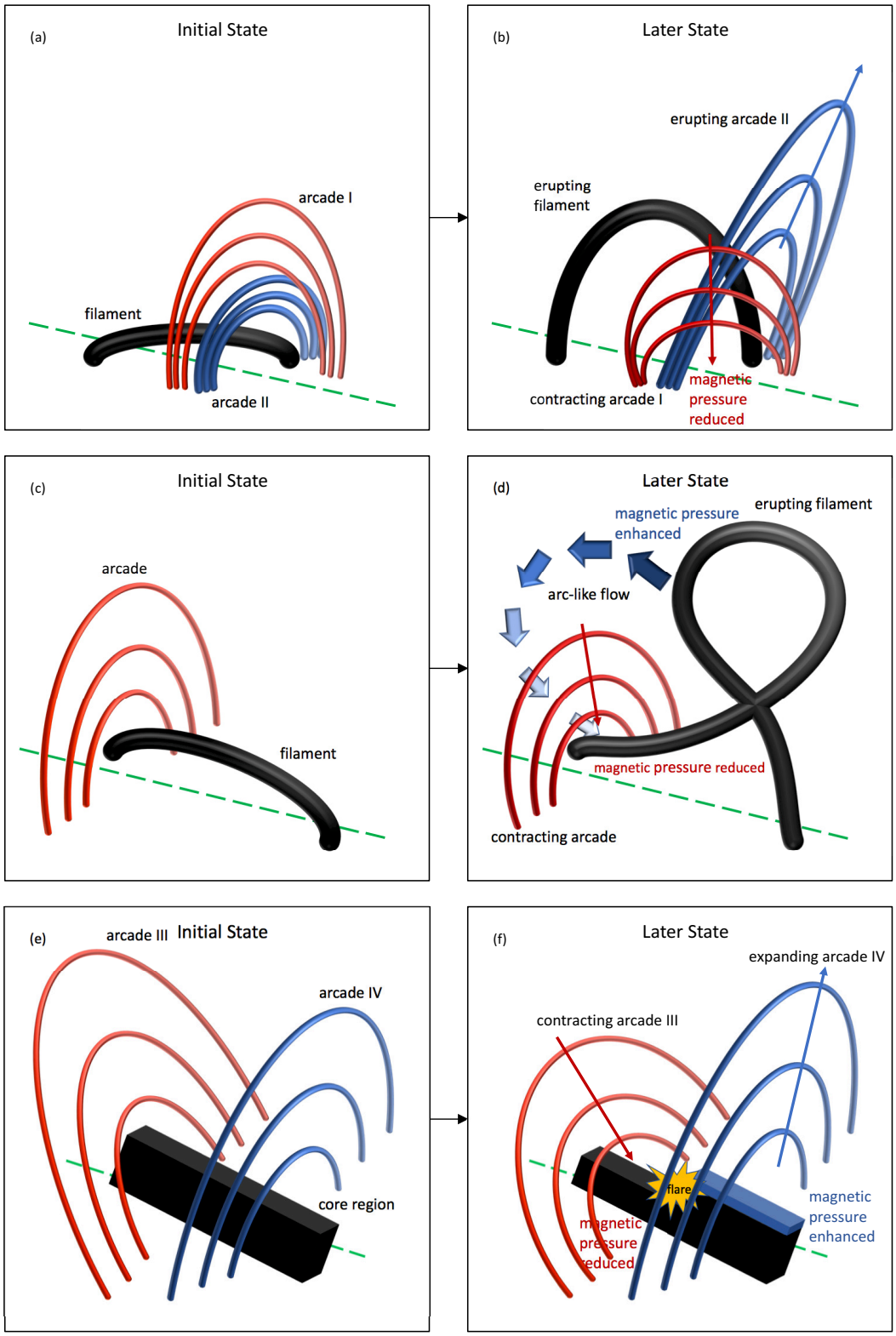

Figure 3.9: Cartoons show our understanding of the implosion events. (a)-(b) for Event I. (c)-(d) for Event II. (e)-(f) for Events III and IV. The thin arrows in each image indicate the directions of the implosion and expansion motions of the arcades. And the green dashed line represents the polarity inversion line.

However, in this context we would like to revisit one of the original assumptions for the implosion conjecture in Hudson (2000) (described in Section 1.3.1), i.e., that gravity takes no significant role in the coronal dynamics. This might not always be the case, especially when a filament is involved, and this could lead to unsuccessful implosions. Take the illustrations Figure 3.9(c)-(d) for example in a general way (rather than considering the specific Event II). Suppose, as a thought experiment, that before the eruption in Figure 3.9(c), the filament is mass loaded, with the downward gravitational force contributing a non-negligible amount to the force balance against the upward Lorentz force. Now imagine what would happen if much of the material along the filament drained down to the photosphere. As the local plasma density and thus gravitational pull are reduced, the filament field would inflate, simultaneously pushing the overlying arcade outward, which is the opposite of implosions. Similarly, during the eruption in Figure 3.9(d), such a process would occur if mass along the filament field could drain down (see relevant studies, e.g., Bi et al. 2014; Fan 2017; Jenkins et al. 2018, pointing out that substantial filament material that drains down may influence the dynamics) and also spread into a larger volume. Moreover, as the filament field becomes more vertical, the draining could increase, further inflating surrounding field. Thus the overlying arcade would expand if the magnetic energy change associated with the filament is not considered. However, in fact, the filament field becomes "weaker" locally, distributing into a larger volume and transferring its energy into plasma kinetic and gravitational energy. As argued by Hudson (2000) and Russell et al. (2015), to achieve a new equilibrium, the overlying arcade would implode toward the magnetic-pressure-reduced filament. At the end, in this scenario we would have two competing mechanisms controlling the dynamics: gravity reduction making the field expand and magnetic pressure reduction making the field implode. In some cases, the magnetic pressure reduction is dominant so we see implosions, like Events I and II here, while the gravity reduction may overtake in other situations, which might be one of the reasons for rarity of well-observed implosions.

3.4 Conclusions

With the four selected events having the up-to-now most clearly observed continuously contracting loops in an edge-on geometry from the viewpoint of SDO/AIA,

supplemented by observations from STEREO, for the first time we demonstrate the existence of real contractions of loops in the global coronal dynamics unambiguously. The implosion conjecture proposed by Hudson (2000) in the interpretation of these events is found to be effective, in comparison with alternative theories for which disagreements currently exist between observations and simulations or other predictions. Meanwhile, the discussion also leads us to find two implosion categories that can be associated either with solar eruptions or with flares, and the models put forward according to the conjecture can reasonably explain their distinct observational characteristics. However, it is also pointed out that in some cases the implosion scenario may not be valid as one of the original assumptions about the role of gravitation in the dynamics may fail.

Chapter 4

Study of an Inflow-type Implosion and Associated Reconnection Flows

This work can be found in the publication Wang et al. (2017). EIS data is processed by Natasha Jeffrey. The alignment between images of AIA and EIS and the analyses of EIS results are conducted by the author.

4.1 Introduction to the Chapter

As demonstrated in Section 1.3.4, inflow can be regarded as a type of implosion, which reflects the magnetic energy release in or transfer out of the diffusion region. In this chapter, we will study an inflow event and associated reconnection flows with excellent observations from SDO/AIA and Hinode/EIS.

The "CSHKP" model is the standard 2D framework for two-ribbon flares (Carmichael 1964; Sturrock 1966; Hirayama 1974; Kopp & Pneuman 1976), and predicts several different flows in the flare corona. There is an inflow of plasma and magnetic field towards a diffusion region where reconnection occurs, and an outflow from this region of newly-reconnected field retracting due to magnetic tension. Both flows are (roughly) perpendicular to the magnetic field direction. There is cooling, condensing material flowing along post-reconnection loops down towards the solar surface. The flare or eruption may influence the ubiquitous upflows at the edge of the active region (AR). In this work, we show that a plasma upflow parallel to the inflow field could also happen as the field erupts.

Evidence for reconnection inflows has been reported in a handful of flares, mainly

at the solar limb. Yokoyama et al. (2001) reported the first clear extreme ultraviolet (EUV) inflow following an eruption, with a bright cusp – another ingredient in the "CSHKP" model – seen underneath in soft X-rays (SXR). Narukage & Shibata (2006) found a further 6 limb inflow events in nearly 5 years of Extreme-ultraviolet Imaging Telescope (EIT) observations. A bright, elongated structure in the inflow convergence region was claimed by Lin et al. (2005) to be a current sheet, and the features flowing up along it to be reconnection outflows. A few more inflows have been reported using observations from the Atmospheric Imaging Assembly (AIA; Lemen et al. 2012) onboard the Solar Dynamics Observatory (SDO; Pesnell et al. 2012). Savage et al. (2012) studied an inflow with speed up to ~ 300 km s^{-1} in an impulsive flare, while other reports, usually of long duration events (LDEs) have speeds below ~ 100 km s^{-1}. Sun et al. (2015a) reported groups of inflowing "threads" with plasma heating where they make contact, but without a clear hot cusp. In 3 different flares, Su et al. (2013), Yang et al. (2015), and Zhu et al. (2016) observed a reconnection inflow with two sets of closed loops approaching each other - a different geometry from the standard model.

Reconnection outflows – the retraction of post-reconnection magnetic loops – have occasionally been reported in SXR limb flares (Forbes & Acton 1996; Reeves et al. 2008), but EUV is better at picking out retracting structures. Liu et al. (2013) detected many individual retracting loops in AIA 131 Å observations of a limb flare, with speeds from tens to hundreds of km s^{-1}. Imada et al. (2013) combined AIA and EIS spectroscopic observations to infer that the hot reconnected loops ~ 30 MK could shrink above 500 km s^{-1}. Supra-arcade downflows, the dark voids in EUV and SXR observations appearing high in the corona and traveling down at tens to hundreds of km s^{-1}, are interpreted as the cross-sections of underdense, retracting post-reconnection loops, or the 'wakes' left as they descend (e.g., McKenzie & Hudson 1999). Plasma draining in flare loops as reconnection downflows has also been observed (e.g., Savage et al. 2012). The EUV Imaging Spectrometer (EIS; Culhane et al. 2007) on Hinode shows that the draining speed along AR loops at quiescent stage (when there is no flare or eruption) is around tens of km s^{-1} (Del Zanna 2008; Syntelis et al. 2012).

The inflow Alfvén Mach number defining the reconnection rate for these events is estimated at $\sim 10^{-1} - 10^{-3}$ in the fast reconnection regime (the slow Sweet-Parker rate is $\sim 10^{-4} - 10^{-6}$ for typical coronal conditions; Aschwanden 2005). But a good

estimate of the reconnection rate requires knowledge of the coronal magnetic field strength, which is difficult to obtain in the limb events stated above. Their position also makes the relationship between the cusp, loops and footpoints hard to ascertain as the footpoints are usually obscured by the solar limb or complex foreground structures.

We report here on a long-lasting reconnection event near the disk center, focusing on its flow processes and magnetic reconnection rate. Li et al. (2017) studied this event using SDO/AIA, demonstrating the relationship between the erupting flux rope and magnetic reconnection, and the transition from 3D to 2D reconnection. The event's location and quasi-2D geometry in the late phase permit a good estimate of the coronal Alfvén speed and reconnection rate. It exhibits the norms of the standard "CSHKP" model, with a well-formed cusp underneath inflow threads which can be mapped well to their lower-atmosphere counterparts. The field below the cusp contracts and cools (though the brightest portion rises). We also find spectroscopic evidence for a new kind of plasma upflows associated with the expanding but closed inflow field, distinct from the common plasma upflows at the AR boundary that have been reported by previous authors.

4.2 Observations and Analyses

4.2.1 Instruments and Data Reduction

SOL2016-03-23T03:54 was a Geostationary Operational Environmental Satellite (GOES) class C1.1 flare in AR NOAA 12524 (N15W16). We study it from ~ 01:00 UT to ~ 07:00 UT. The SDO/AIA and Helioseismic and Magnetic Imager (HMI; Schou et al. 2012) provide EUV images and photospheric magnetograms, respectively, which have been processed using standard software (Boerner et al. 2012) and rotated to 01:00 UT. The EIS on Hinode observes the AR in a slow raster from 04:01:50 UT to 05:02:42 UT with a 1" slit moving around every minute from solar west to east over a field-of-view 119.8"×512.0". Line-of-sight velocities are obtained from Fe XII and Fe XIII lines, which are intense and also visible outside the active region, for estimating a reliable rest wavelength. Standard EIS data reduction procedures were used, and the spectral lines were fitted with single Gaussians. The rest wavelength was extracted from a quiet Sun region X~ (−24″, 85″) and Y~ (157″, 207″) (excluding

missing values along a vertical data gap at X$\sim$ 13″) free of AR emission. The upper-limit uncertainty is ~ 5 km s^{-1} for both Fe XII 195.12 Å and Fe XIII 202.04 Å, and Fe XVI 262.98 Å has an upper-limit uncertainty ~ 9 km s^{-1}. The alignment between AIA and EIS is conducted by eye, and also takes Fe IX 197.86 Å into account (but Fe IX intensity is too low for reliable Doppler velocity diagnostics). Fe IX is aligned with 171 Å, Fe XII with 193 Å, Fe XIII with 211 Å, and Fe XVI with 335 Å, as their characteristic temperatures are comparable separately. The accuracy of the alignment is $\sim 1-2$ arcsecs.

4.2.2 Evolution of the Flare

Figure 4.1 shows the overall evolution of the flare. Before the flare (Figure 4.1(a)) a large arcade of loops in 171 Å envelopes a dark void underneath, possibly a flux rope (Li et al. 2017). Between the arcade footpoints a filament can vaguely be seen (Figure 4.1(b) and (e) show the filament more clearly). In Figure 4.1(b), the two ends of the filament suddenly brighten (microflare), accompanied by a small ejection to the north. This may show the destabilization of the hosted flux rope, leading to the subsequent arcade eruption in Figure 4.1(c). As the arcade erupts, its legs converge, forming a dark cusp underneath in 171 Å, shown in Figure 4.1(d). The flare ensues with a bright cusp in 131 Å (red) inside the dark cusp in 171 Å. Then two ribbons sweep across the footpoints of the bright cusp and separate away from the filament, seen in 304 Å in Figure 4.1(e). Figure 4.1(f) shows the post-flare state with flaring loops appearing in 171 Å. The main evolution from Figure 4.1(a), (c), (d) and (f) reveals that the correspondence between the pre-flare arcade, the erupting arcade, the bright cusp and the flaring loops is well established in terms of their footpoint locations, indicated by the two magenta circles. Figures 4.2(a)-(c) show the timeslices corresponding to cuts 1-3 in Figure 4.1, respectively. A lightcurve in 304 Å for the microflare in Figure 4.1(b) is added in Figure 4.2(c), and the GOES SXR lightcurves in Figure 4.2(d). The vertical dotted line "A" indicates the timing of the microflare and the arcade eruption, and the line "B" the timing of the inflow and the flare. Different flows are discussed in the following paragraphs.

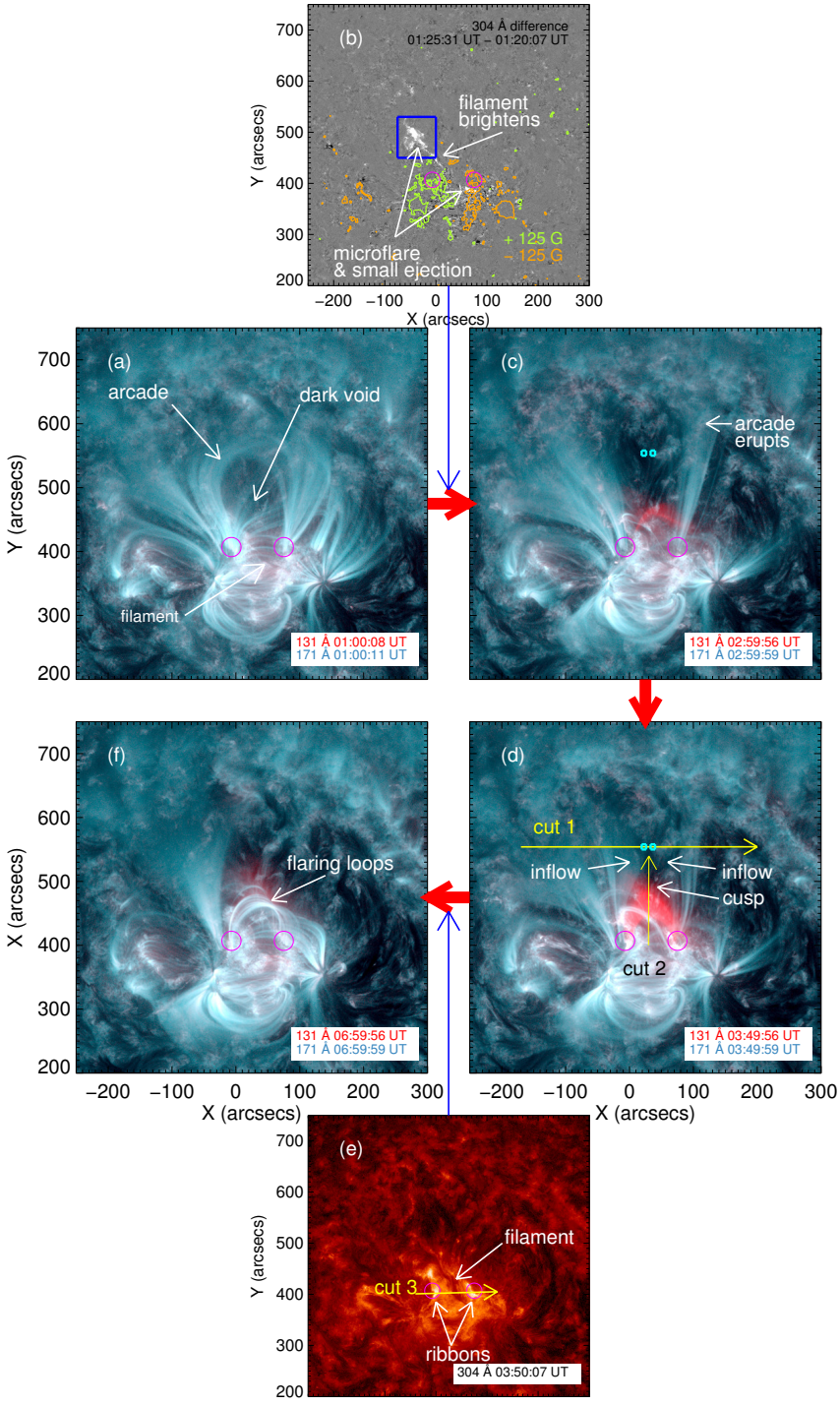

Figure 4.1: Evolution of the flare. (a), (c), (d) and (f) show the main evolution sequence in composite AIA 131 Å and 171 Å images. (b) The microflare and small ejection in the 304 Å difference image just before the arcade eruption. The HMI magnetogram contours at ±125 G are overlaid. The blue rectangle is used for the lightcurve in Figure 4.2(c). (e) The ribbon separation in 304 Å. The magenta circles in each image show the relevant footpoint locations. Cuts 1-3 are used for timeslices in Figures 4.2(a)-(c), respectively. The two cyan boxes in (c) and (d) are for DEM analysis in Section 4.2.4. An animation of this figure is available in Wang et al. (2017) at the link http://iopscience.iop.org/article/10.3847/2041-8213/aa8904/meta.

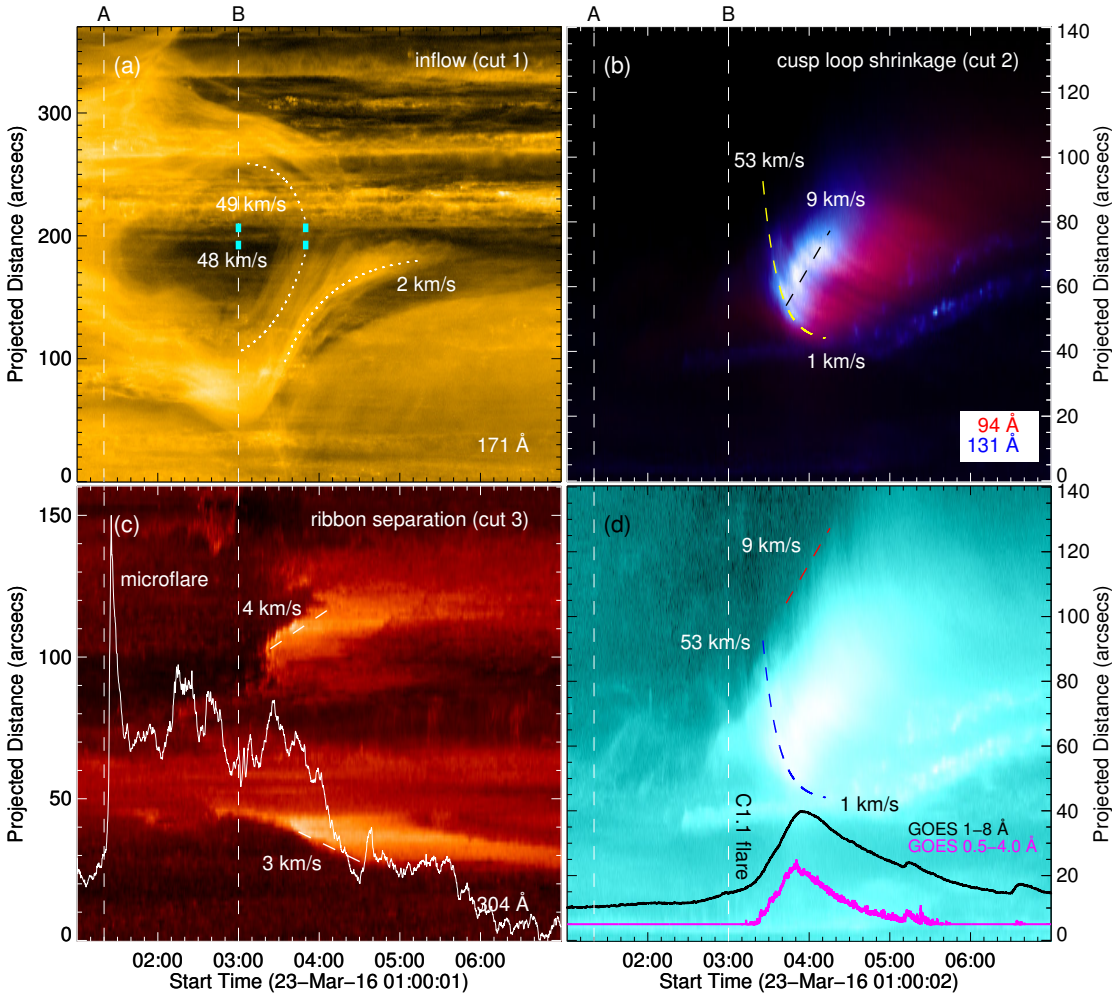

Figure 4.2: Detailed dynamics of the Event. (a) Timeslice of Cut 1 for the evolution of the inflow threads. The two cyan boxes at 03:00 UT and also 03:50 UT show the positions used for DEM analysis in Section 4.2.4, as in Figures 4.1(c) and (d). The speeds given are for the final times of the fit curves. (b) Timeslice of cut 2 combines 94 Å and 131 Å on a linear intensity scale, showing the evolution of the bright cusp. Its corresponding image on a logarithmic intensity scale in 131 Å is plotted in (d). The yellow dashed fit curve is the same as the red one in (d), and the black dashed fit curve is the same as the red one in (d) but moved downwards to match the brightest portion. (c) Timeslice of cut 3 for the evolution of the ribbons. The lightcurve in 304 Å of the microflare indicated in Figure 4.1(b) is overlaid. (d) GOES SXR lightcurves overlaid on the timeslice image of cut 2 in 131 Å on a logarithmic intensity scale for reference. The dotted line "A" denotes the timings of the arcade eruption and the microflare, and "B" the timings of the inflow and the C1.1 flare.

4.2.3 Flows in the Flare

Reconnection Inflows Figure 4.2(a) shows the evolution along cut 1 through the flare cusp region. Before the flare the threads forming the arcade legs separate as the flux rope erupts. The threads then accelerate towards the (presumed) central diffusion region, approaching with projected speeds of tens of km s^{-1}, similar on either side. These are fitted with exponential equations by picking a few points along specific inflow features and extrapolated to the diffusion regions indicated by the cyan boxes. The speeds at the final times of the fit curves are larger than that in Li et al. (2017), because we choose a cut with higher altitude than theirs, closer to the reconnection site at 03:50 UT in Figure 4.1(d), in order to account for the progressively higher up reconnection site. Accelerated inflows were also found by Sun et al. (2015a) and Zhu et al. (2016). After the GOES peak, the western leg gradually fades, while the flow of the outer threads of the eastern leg starts to decelerate towards the central region, reducing to a few km s^{-1} and lasting for around one hour. Figure 4.2(c) shows the corresponding ribbon separation, also with similar speed on each side.

Reconnection Outflows The post-reconnection outflow is manifested as contraction of the loops underneath the cusp, visible as bright and dark striations in the stackplot (Figure 4.2(b)) of superposed 131 Å and 94 Å slices, on a linear intensity scale, along cut 2 vertically down through the cusp loops (also can be seen in the reference image of Figure 4.2(d) on a logarithmic intensity scale in 131 Å). The yellow dashed line in Figure 4.2(b) shows the looptop in the cusp declining in altitude with time, illustrating the contraction of the cusp loops. The contraction decelerates with time, while the loops also cool down from 131 Å (~10 MK) to 94 Å (~6.8 MK). This is not well observed in the past to our knowledge. Meanwhile the brightest portion of the cusp rises, as expected if the reconnection site progressively moves upwards. We note the qualitative similarity between the observed trajectories of the contracting loops and those calculated by Lin (2004) for a 2D reconnecting current sheet model.

Plasma downflows Figures 4.3(a) and (c) show the Fe XVI and Fe XIII intensity maps from EIS, and Figures 4.3(b) and (d) the corresponding line-of-sight velocity maps. For comparison, Figures 4.3(e) and (f) are synthesized AIA "raster" images which simulate the EIS slit scanning mode, produced by combining narrow slices

of AIA images at the EIS slit locations and times. Looptops and loop legs of the flare arcades (Figure 4.3(b) or (d)) have redshifts of ~ 13 km s^{-1} indicating plasma draining, or loop contraction. We consider plasma draining to be the more likely explanation as the line-of-sight speed is much larger than the projected contraction speed ~ 1 km s^{-1} obtained from the hotter 94 Å observations at that time (Figure 4.2(b)). An interpretation in terms of contraction is thus difficult to reconcile with the observed arcade geometry.

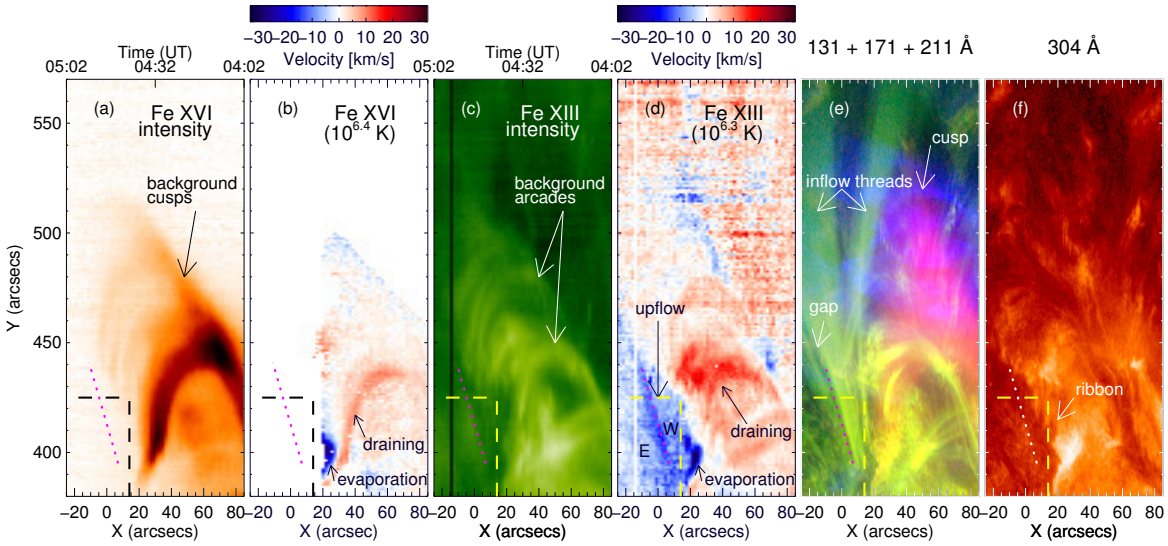

Figure 4.3: Comparison of EIS and AIA observations of the Event. (a)-(b) Fe XVI 262.98 Å intensity and Doppler velocity maps. (c)-(d) Fe XIII 202.04 Å intensity and Doppler velocity maps ((Fe XII 195.12 Å intensity and Doppler velocity maps are not shown here as they are similar to the ones of Fe XIII)). The sampling times of the EIS slit are added above (a) and (c). (e)-(f) synthesized AIA images simulating the EIS slit scanning mode for comparison. 131 Å is red, 171 Å green, and 211 Å blue in (e). To align with EIS observations, they have not been rotated like in Figure 4.1. The dashed line at the bottom left corner encloses the extended blueshift area in (d). The magenta dotted line is for the longitudinal velocity profiles in Figure 4.4.

Plasma Upflows We also have evidence of plasma upflows at the edge of the AR. The strong blueshift ~ 25 km s^{-1} at the eastern footpoint of the cusp (at (X, Y) $\sim$ (25″, 400″) in Figures 4.3(b) and (d)) could indicate chromospheric evaporation onto the reconnected cusp field (Figures 4.3(a) and (e)). Just to its east is an extended

blueshift area (enclosed by the yellow dashed line at the bottom left corner in Figure 4.3(d)). This area can be divided into three parts, the strongest blueshift feature indicated by the magenta dotted line, the "E" region to the east, and the "W" region to the west. The "W" region possesses stronger blueshift than the "E" region. Note that the strongest blueshift feature in this area is well aligned with the gap with weak emission in the composite AIA image in Figure 4.3(e), which boosts our confidence in the accuracy of the alignment between EIS and AIA.

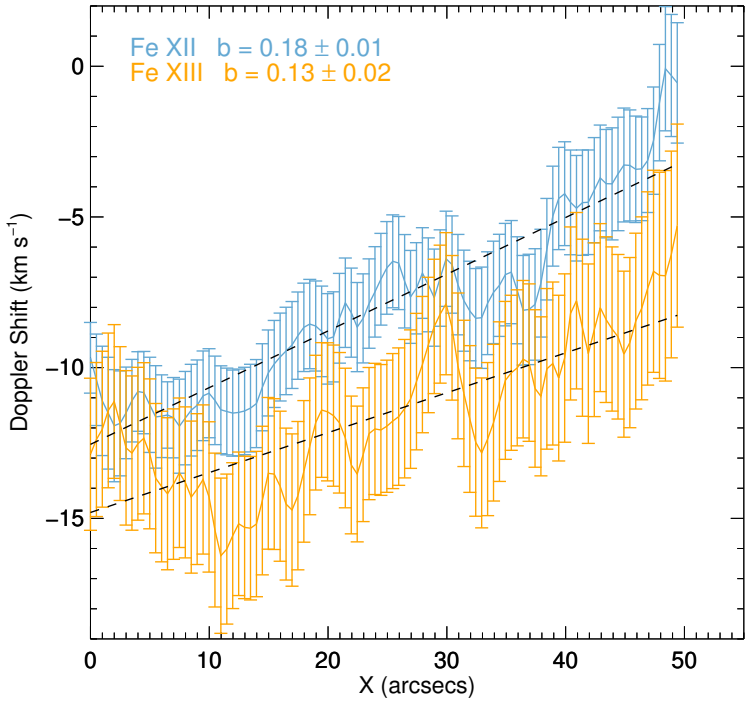

Figure 4.4: Longitudinal velocity profiles for Fe XII and Fe XIII along the dotted line in Figure 4.3. The origin of the X axis represents the bottom of the dotted line. The dashed line is the linear fit for each profile. "b" represents the slope of the fit and its $1-\sigma$ uncertainty. The uncertainty for the rest wavelength estimation is ~ 5 km s^{-1} for both lines, which would shift the entire profiles up or down.

By comparing Figure 4.3(d) with (e), it can be seen that the field corresponding to this extended blueshift area has not yet been reconnected in the main flare related to the bright cusp, so the blueshifts cannot be explained by the evaporation from the

main flare. Nor can they be attributed to evaporation in the background, as the 304 Å ribbon in Figure 4.3(f) has not reached this area. For the strongest blueshift feature indicated by the magenta line, which is just to the east of the edge of the inflow threads, we can also exclude it being due to changing field inclination. If the line-of-sight velocity profiles along the dotted line, shown in Figure 4.4, were completely due to the inflow threads inclining towards us, we would expect a blueshift around zero at the footpoints and increasing with altitude. The observation in Figure 4.4 contradicts this. Figure 4.4 also excludes a loop siphon flow, in which the flows accelerate towards higher altitudes (Aschwanden 2005). An easy way to interpret the blueshift along the dotted line is to invoke a plasma upflow along a field which inclines towards us. The same argument also applies to the "W" region. For the "E" region, it is difficult to argue as the velocity values are comparable to the rest wavelength uncertainty.

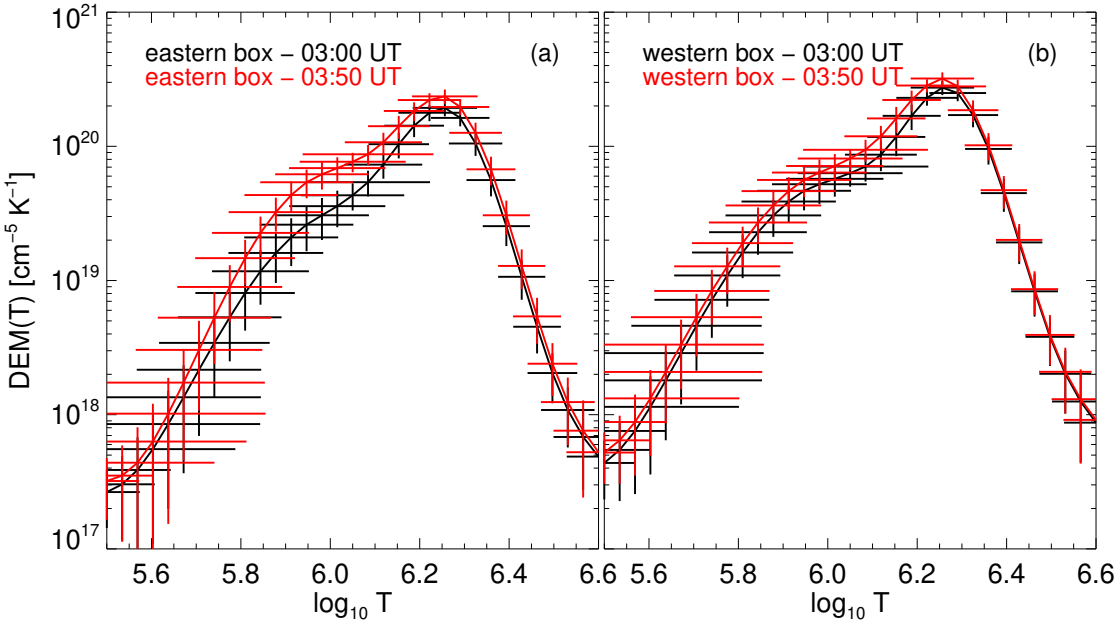

Figure 4.5: DEMs at 03:00 UT and 03:50 UT for the cyan eastern and western boxes in Figures 4.1(c) and (d), respectively.

4.2.4 Electron Density Estimate

DEM (Section 1.4.6) analysis can be used to estimate the electron density n_e (Hannah & Kontar 2013). The DEM is defined as $\xi(T) = n_e^2 dl/dT$ (Craig & Brown 1976), and

integrating over T results in the emission measure along the line-of-sight EM = $\int \xi(t)dT = \int n_e^2 dl$.

We calculate the emission measure during (EM_{fl} at 03:50 UT) and before (EM_{pre} at 03:00 UT) in the inflow, using the regularization method of Hannah & Kontar (2012) to recover $\xi(T)$ from the mean intensity in each of the 6 AIA wave bands (94, 131, 171, 193, 211, 335 Å) with single exposures for both the eastern and western inflow regions (the two cyan boxes in Figure 4.1(c) and (d)). The mean intensity is used in order to smooth out the fluctuations pixel by pixel. The temperature range used as input is $10^{5.5}$-$10^{6.6}$ K, because the inflow threads can hardly be seen in high temperature wavebands like 94 and 131 Å. The DEM results are shown in Figure 4.5. It can be seen that the DEM enhancements mainly happen between $10^{5.8}$ K and $10^{6.3}$ K. This is consistent with AIA observations, as the inflow threads can be most clearly seen in AIA 171 Å which is more sensitive to this temperature range compared to other filters. The DEMs can then be transformed to the EMs using the IDL integral procedure int_tabulated.pro. However, the resulting EM also contains a contribution from the background and foreground corona besides the inflow region. We then exploit the technique of the difference of EMs to estimate the density of the inflow threads, which is demonstrated as follows. In Figure 4.1(c), before the inflow the EM is,

$$\mathrm{EM}_{pre} \approx (n_e^{inflow\_pre})^2\, h_{inflow} + (n_e^{other\_pre})^2\, h_{other} \tag{4.1}$$

where the superscript "inflow_pre" indicates that the quantity is taken from the inflow volume in the pre-inflow state, and "other_pre" the background and foreground corona without the inflow region before the inflow. During the inflow in Figure 4.1(d), the EM is,

$$\mathrm{EM}_{fl} \approx (n_e^{inflow\_fl})^2\, h_{inflow} + (n_e^{other\_fl})^2\, h_{other} \tag{4.2}$$

where the meanings of the superscripts are similar to the above but during the inflow. If we assume that: (i) the background and foreground density outside the inflow threads does not change much during the event, that is $n_e^{other\_fl} \approx n_e^{other\_pre}$; and (ii) the density within the inflow region during the inflow (Figure 4.1(d)) is much larger than before the inflow (Figure 4.1(c)), that is $n_e^{inflow\_fl} \gg n_e^{inflow\_pre}$, it then follows that,

$$\mathrm{EM}_{fl} - \mathrm{EM}_{pre} \approx (n_e^{inflow\_fl})^2\, h_{inflow} \tag{4.3}$$

and finally, the density of the inflow threads can be obtained as,

$$n_e^{inflow\_fl} \approx \sqrt{(\mathrm{EM}_{fl} - \mathrm{EM}_{pre})/h_{inflow}} \tag{4.4}$$

or

$$n_e = \sqrt{\mathrm{EM}_{in}/L}, \tag{4.5}$$

if we use n_e for $n_e^{inflow\_fl}$, EM_{in} to represent $\mathrm{EM}_{fl} - \mathrm{EM}_{pre}$, and L being h_{inflow}, for simplicity.

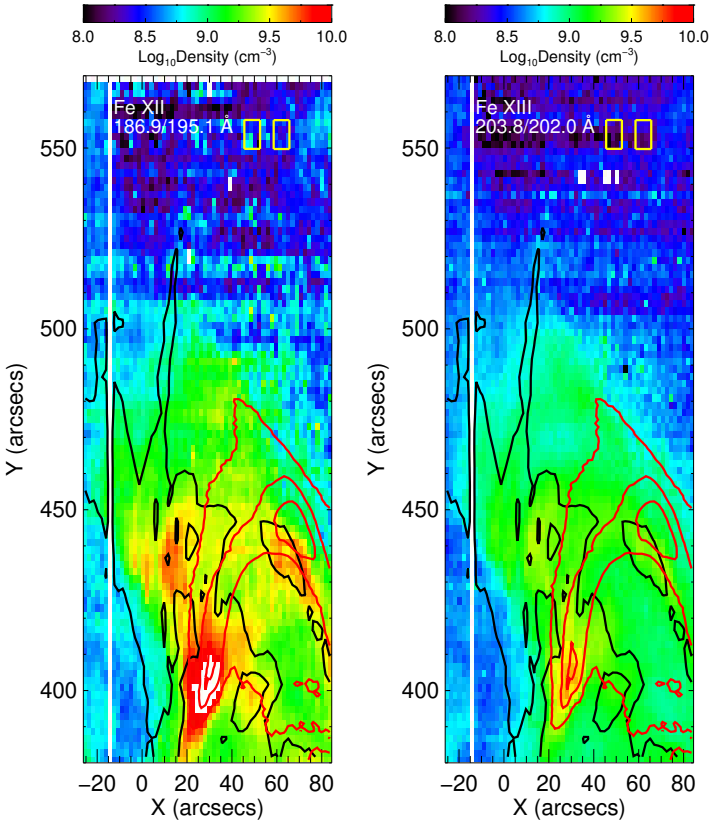

Figure 4.6: EIS density diagnostic results using spectral line ratios, Fe XII 186.9/195.1 Å and Fe XIII 203.8/202.0 Å, respectively. The two yellow boxes in each image correspond to the two cyan boxes in Figure 4.1(c) or (d). The black contours are for Fe IX at 10 % and 30 % levels, and the red ones for Fe XVI at 20 %, 50 % and 80 % levels.

As $n_e \propto L^{-0.5}$ in Equation (4.5), the estimated density is not very sensitive to the choice of the thickness L. Thus we choose the diameter of the magenta circle

(estimated footpoint region of the inflow thread) in Figure 4.1 as an approximation of the thickness of the inflow threads, $L = 15$ arcsecs $\approx 1.1 \times 10^9$ cm. We then find $n_e \approx 2.1 \times 10^8$ cm^{-3} and $\approx 2.0 \times 10^8$ cm^{-3} for the eastern and western regions, respectively (Table 4.1).

We briefly comment on the assumptions (i) and (ii) above for estimating the electron density of the inflow thread. Assumption (i) seems reasonable as no obvious events (except the inflow) happen during this period along the chosen boxes' line of sight. Assumption (ii) could be true, as firstly in the pre-inflow stage the two boxes are located within the dark void region (Figure 4.1(c)), which means lack of emitting plasma, and secondly the void expansion may further evacuate the plasma there. And the obtained results above are well consistent with EIS density diagnostics in Figure 4.6 using spectral line ratios, Fe XII 186.9/195.1 Å formed at $10^{6.2}$ K ($\approx 3.2 \times 10^8$ cm^{-3} for the eastern box and $\approx 2.8 \times 10^8$ cm^{-3} for the western one) and Fe XIII 203.8/202.0 Å at $10^{6.3}$ K ($\approx 1.7 \times 10^8$ cm^{-3} for the eastern box and $\approx 2.0 \times 10^8$ cm^{-3} for the western one). The densities derived from EIS being slightly different from the results from the DEM technique is probably because the inflow regions at the EIS sampling time (already after 04:00 UT as can be seen in Figure 4.3) has moved upwards, or because of the choice of the thickness of the inflow threads in the DEM analysis.

4.2.5 Magnetic Reconnection Rate

The magnetic reconnection rate can be represented by the inflow Alfvén Mach number

$$M_A = V_{\rm in}/V_A \tag{4.6}$$

where $V_{\rm in}$ is the inflow speed and V_A the local Alfvén speed. $V_{\rm in}$ can be estimated using

$$V_{\rm in} = V_{\rm patt} - V_{\rm xp} \tan\theta \tag{4.7}$$

as in Yokoyama et al. (2001), where $V_{\rm patt}$ is the apparent inflow speed obtained from the pattern of inflowing threads, $V_{\rm xp}$ the rising speed of the reconnection X-point, and θ the angle between the inflow threads and the rising direction of the X-point. This equation accounts for the rising motion of the reconnection site. The Alfvén speed V_A is

$$V_A = \frac{B_{\rm in}}{\sqrt{4\pi\rho}} \approx \frac{B_{\rm in}}{\sqrt{4\pi\mu m_H n_e}} \tag{4.8}$$

in Gauss units, where $B_{\rm in}$ is the magnetic field strength in the inflow region, ρ the mass density, μ the mean atomic weight (~ 1.27 for coronal abundances; Aschwanden 2005), m_H the hydrogen mass, and n_e the electron number density. To obtain $B_{\rm in}$, conservation of magnetic flux can be exploited (e.g. Isobe et al. 2002),

$$B_{\rm in} V_{\rm in} = B_{\rm foot} V_{\rm foot} \tag{4.9}$$

where $B_{\rm foot}$ is the vertical magnetic strength at the photosphere and $V_{\rm foot}$ the separation speed of flaring ribbons. As this AR is close to the solar disk center, HMI longitudinal magnetograms can be used as a good approximation of the vertical field. By combining Equations (4.6), (4.7), (4.8) and (4.9), the final equation for the reconnection rate is

$$M_A = \frac{(V_{\rm patt} - V_{\rm xp} \tan\theta)^2}{B_{\rm foot} V_{\rm foot}} \sqrt{4\pi \mu m_H n_e} \tag{4.10}$$

where the electron number density can be estimated as in Section 4.2.4, and other quantities are obtained as described in the notes to Table 4.1. Note that these estimates are made at $\sim$ 03:50 UT, just before the GOES 1-8 Å flux peaks. The resulting reconnection rates are 0.03 for both the eastern and western inflows.

4.3 Discussion and Conclusions

We have reported the first comprehensive observations of reconnection flows on the solar disk. The inflows show threads or strands of plasma accelerating and later decelerating towards a presumed reconnection site, below which a well-defined hot cusp forms, anchored at the threads' endpoints. Individual cusp loops shrink and cool as the brightest portion of the cusp ascends. The magnetic reconnection rates around the GOES flux peak are 0.03 for both the eastern and western inflows, consistent with fast reconnection (described in Section 4.1), and in the range of previous studies (Yokoyama et al. 2001; Lin et al. 2005; Narukage & Shibata 2006; Bemporad et al. 2010; Savage et al. 2012; Su et al. 2013; Sun et al. 2015a; Zhu et al. 2016). And the reconnection is quite symmetric in this case. According to Equation 4.10, if V_{xp} and θ are good observational estimates, the reconnection rate estimated is most sensitive to V_{patt}, only the transverse component of the real inflow velocity. For a rough estimation of the lower limit of the reconnection rate, we double B_{foot}, V_{foot} and reduce n_e by a factor 10, giving reconnection rates of around 0.003

for both the eastern and western inflows, which are still in the fast reconnection regime.

Table 4.1: Magnetic reconnection parameters.

Region	V_{patt}[a] (km s^{-1})	V_{xp}[b] (km s^{-1})	θ[c] degree	V_{in}[d] (km s^{-1})	V_{foot}[e] (km s^{-1})	B_{foot}[f] (G)	B_{in}[g] (G)	EM$_{in}$[h] (10^{25} cm^{-5})	L[i] arcsec	n_e[j] (10^8 cm^{-3})	V_A[k] (km s^{-1})	M_A[l]
Eastern	43	9	27	38	3	131	10	4.8	15	2.1	1371	0.03
Western	49	9	27	44	4	-125	11	4.3	15	2.0	1551	0.03

[a] obtained from Figure 4.2(a).
[b] estimated from the rising speed of the bright cusp in 131 Å in Figure 4.2(b) and (d).
[c] estimated at half the angle of the dark cusp in 171 Å in Figure 4.1(d).
[d] via Equation (4.7).
[e] from Figure 4.2(c).
[f] approximated as the mean of the HMI longitudinal magnetic strength above a noise level $\sim$ 10 G (Liu et al. 2012b) for the magenta circles in Figure 4.1.
[g] via Equation (4.9) and transformed to absolutes.
[h] through the method in Section 4.2.4.
[i] approximated as the diameter of the magenta circle in Figure 4.1.
[j] via Equation (4.5).
[k] through Equation (4.8).
[l] via Equation (4.6) or (4.10).

There is no emission from the presumed reconnection site; it may be too short or thin, or at the wrong temperature to be detected by the instruments used. We note that the upper part of the dark cusp highlighted in Figure 4.1(d) is dark in all AIA wavelengths, implying that it has a very low density, or temperature above the $\sim$ 10 MK at which the AIA 131 Å filter peaks and where the cusp is clearest.

As argued in Section 4.2.3, possibilities like evaporation from the main flare, field inclining and a siphon flow, could not be the reasons for the blueshifts along the dotted line and in the "W" region in Figure 4.3(d). Plasma upflows along field which inclines towards us could be an explanation for these blueshifts. Blueshift features are found to be ubiquitous at the edge of ARs from EIS observations even in non-flaring regions, persisting from hours to days in areas of weak emission and low density, and possessing velocities around tens of km s^{-1}, faster in hotter lines (e.g., Sakao et al. 2007; Del Zanna 2008; Doschek et al. 2008; Harra et al. 2008; Baker et al. 2009; Démoulin et al. 2013; Brooks et al. 2015). They are interpreted as upflows by some authors and considered to be a possible source of the slow solar wind in the

heliosphere, but the real origin of these blueshift features is still controversial (Abbo et al. 2016, and references therein).

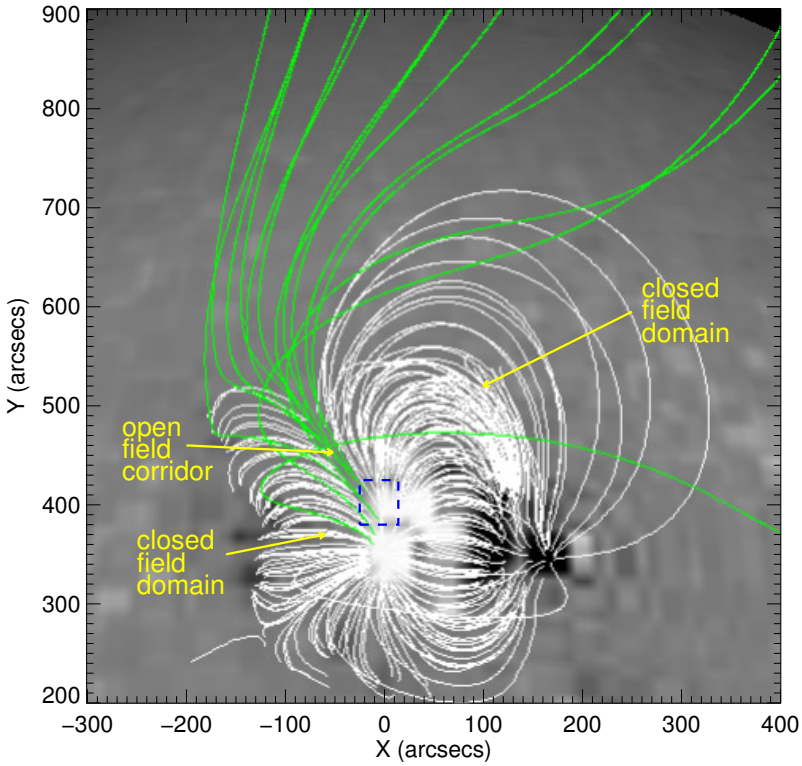

Figure 4.7: Model field at 00:04 UT just before the arcade eruption and the flare, derived from the PFSS package of Solarsoft, showing a narrow open-field corridor between the two closed-field domains. The open-field corridor extends northwards to a coronal hole. The blue dashed box shows the same region as the bottom left corner enclosed by the dashed line in Figure 4.3. To compare with Figure 4.3, this figure has not been rotated like in Figure 4.1.

We here propose a distinction between two upflow components associated with the blueshift features observed in this event. The strongest blueshift in Figure 4.3(d) is well aligned with the gap with weak AIA emission in Figure 4.3(e) which may imply open field short of emitting plasma, while the "W" region evidently corresponds to the large-scale closed loops which are the inflow threads or the legs of the arcade loops erupting outwards[1] in Figure 4.3(e). The potential-field source-surface (PFSS)

[1] The upper part of the inflow threads could be contaminated by the background arcades which

model just before the flare in Figure 4.7 provides supportive evidence. It reflects well the pre-eruption structure seen in Figure 4.1(a), and shows that the extended blueshift area in Figure 4.3(d) consists of a mix of open and closed fields. Two closed-field domains are separated by a very narrow open-field corridor, which matches the structure in the extended blueshift area in Figure 4.3(d) with the strongest blueshift feature indicated by the dotted line separating the "E" and "W" regions apart. Thus it seems that plasma upflows occur along both open field and large-scale closed loops. And the flow along open field could have a higher upward velocity, and a different cause. The argument above helps solve a long-standing problem that whether the blueshift-related upflows at the AR boundary are associated with open or large-scale closed field (Sakao et al. 2007; Harra et al. 2008; Baker et al. 2009; Del Zanna et al. 2011; Boutry et al. 2012; Brooks et al. 2015; Edwards et al. 2016).

As the blueshift levels of the feature indicated by the dotted line in Figure 4.3(d) and the "W" region are quite different, different mechanisms may be responsible for the associated upflows. For the upflow in the "W" region, expansion of related large-scale closed loops (Harra et al. 2008) could be an explanation. When the flux tube of the arcade expands outwards, the plasma within would expand outward and dilute (Reeves et al. 2010, see the third row of its Figure 9), which results in depressurization. We suggest here that the expansion may not be adiabatic, as the depressurization could induce a plasma upflow from the coronal base along the legs of the expanding arcade. A vivid analogy of this depressurization process is the water in a tube being pumped out by rapidly pulling a plunger, or the air being pumped in as the volume of the lung is increased. Both the plasma expansion itself because of the field inflation and the induced upflow due to depressurization could contribute to the blueshift observed along the expanding closed field. As the inflating field is the inflow threads here, the upflow from the bottom of the corona may serve as a way to increase the plasma density advected into the reconnection region or other acceleration regions (e.g., the slow-mode shock), which could help relax the "electron number problem" (Brown & Melrose 1977; Fletcher & Hudson 2008) to some extent. A rough estimate of the upward electron flux is $\sim 10^{19}$ m^{-2} s^{-1}, which can be obtained by using the upflow speed ~ 7 km s^{-1} (inferred later) and coronal density $\sim 10^{9}$ cm^{-3} (if the upflow can be induced deeper in the atmosphere, the density could be higher). *Fermi* Gamma-ray Burst Monitor (GBM; Meegan et al. 2009)

have draining plasma.

observations barely show any hard X-ray emission from this flare (unfortunately also no observations from the Reuven Ramaty High Energy Solar Spectroscopic Imager for this event), implying a very weak requirement for the electron flux. For a major flare, the eruption and arcade expansion could be more violent, possibly with a faster upflow and increased electron supply.

For the upflow along the open-field, Antiochos et al. (2011) shows that a narrow open-field corridor maps to separatrices and QSLs in the heliosphere where the magnetic connectivities change dramatically, and they are the natural region for interchange reconnection between open and closed field to take place (Fisk et al. 1999; Fisk 2003). Thus the open field here in Figure 4.7 could reconnect with the two closed domains nearby, transporting plasma from the closed to the open field. Comparing Figure 4.1(a) with (f), it can be seen that the intensity of the eastern closed domain has a significant decrease during the evolution while the large-scale loops nearby to the west become more intense, which could mean that an interaction happens between the eastern closed domain and the narrow open field corridor. The main flare or the arcade eruption observed in the western domain may facilitate or impede the dynamics.

A characteristic inclination angle of the open field in Figure 4.7 towards us can be obtained from the PFSS model to be $\sim 45°$. Figure 4.3(d) (and also Figure 4.3(b)) provides the characteristic values of the longitudinal velocities of the blueshift feature indicated by the dotted line, the "W" region, the evaporation feature, and the plasma draining, to be ~ 10 km s^{-1}, ~ 5 km s^{-1}, ~ 25 km s^{-1}, and ~ 13 km s^{-1}, separately. If we assume that all the fields related to the above features incline towards us with roughly the same angle $\sim 45°$ as the open field does, the total speeds of the associated plasma flows travelling along these fields can be estimated to be ~ 14 km s^{-1}, ~ 7 km s^{-1}, ~ 35 km s^{-1}, and ~ 18 km s^{-1}, respectively. They are all subsonic as the sound speed for a plasma with a temperature $T_e \sim 2.0$ MK or ~ 2.5 MK (for Fe XIII $\sim 10^{6.3}$ K and Fe XVI $\sim 10^{6.4}$ K, respectively) is $c_s = 147\sqrt{T_e/1\ \mathrm{MK}} \sim 208$ km s^{-1} or ~ 232 km s^{-1} (Aschwanden 2005). The upflow speeds from a few to tens of km s^{-1} at the edge of the AR are consistent with previous EIS observations (Del Zanna 2008). The evaporation speed ~ 35 km s^{-1} is similar to the results obtained by Milligan & Dennis (2009) also for a C class flare at this temperature range. The plasma draining speed ~ 18 km s^{-1} is also comparable to previous results derived from EIS spectroscopy (Del Zanna 2008; Syntelis et al. 2012) though they measured at the

quiet stage of the AR evolution. The plasma draining at these spectral lines may reflect the warm counterpart of the cold coronal rain (e.g., Schrijver 2001; Kamio et al. 2011; Vashalomidze et al. 2015) observed later in 304 Å.

In addition, if we take the field inclination into account when calculating the reconnection rate, this will slightly change the values of V_{xp} and θ in Table 4.1, but the final reconnection rate around the GOES flux peak will still be rounded to 0.03 for both the inflow regions and in agreement with fast reconnection.

Together with Li et al. (2017), this work reveals the 2D and 3D aspects of this event. The wealth of diagnostic information on the flows and plasma properties around the reconnection region and at the periphery of the AR can be further used to explore the energetics of the reconnection process and the detailed dynamics of flow evolution, while the availability of HMI vector magnetograms means that the magnetic evolution and plasma flows can be investigated in more detail using magnetic field extrapolations and MHD simulations.

Chapter 5

Conclusions

5.1 Thesis Summary

This thesis is focused on the implosion phenomenon in solar eruptions and flares, which is predicted by Hudson (2000), on the basis of the equivalence of magnetic energy and pressure, and the dominance of Lorentz force in the corona. Before our work, though the spirit of the implosion idea by which the magnetic field becomes more compact after energy release is insightful and attractive, what implosions exactly correspond to in observations was not well demonstrated in the original paper of Hudson (2000). This led subsequent authors to use the concept ambiguously, and produced confusion. To address this problem, in Section 1.3.4, we incorporate three different phenomena, that is, contraction of peripheral arcade loops, reconnection inflow, and dipolarisation of newly reconnected field lines, into the implosion idea. They are separately called "peripheral implosion", "inflow-type implosion" and "dipolarisation-type implosion". The dipolarisation-type implosion is different from the former two types in that it is caused by enhanced magnetic tension rather than reduced magnetic pressure, and the energy-releasing core shrinks itself. According to this generalization and categorization, future study and understanding of implosions can be clearer and more specific.

Before the research of Chapter 2, observations usually showed contraction of loops in a face-on state on the solar disk. This motion was suspected to be a projection effect as the loops are pushed downward the solar surface by an associated erupting magnetic structure, rather than a real contraction. In Chapter 2, by employing an excellent observation of a flare near the disk center, we find two pieces of evidence

from observations (loops contracting by a half; and two parallel contracting features), and a third piece of evidence from NLFFF extrapolations by comparing the states before and after the flare, which together support the reality of the contracting motion of the peripheral arcade loops. It is also found that this arcade implosion is more likely to be caused by the reduction of the underlying filament field in the erupting process instead of local energy dissipation in the flare invoked by previous authors. This is because the contraction of the inner arcade loops only happens before the peak of the impulsive phase. A sequence of events, i.e., the microflare, the distortion and eruption of the disturbed filament, the peripheral arcade implosion, and the main flare, prompts us to unite three scenarios for active region magnetic evolution, namely the metastable eruption model, the implosion conjecture, and the standard"CSHKP" flare model.

Though the arguments in Chapter 2 are novel, they are still indirect and it is not conclusive that the apparent contraction of loops observed face-on must correspond to implosion. In Chapter 3, after surveying tens of thousands of solar events, we selected four with the continuously contracting loops in an almost edge-on state, and in terms of geometry and dynamics, demonstrate the reality of implosion phenomena in the global coronal evolution unambiguously for the first time. Together with previous simulations and associated theories, the observations of these four events allow us to exclude the explanation proposed by Zuccarello et al. (2017) using the analog of a vortex flow generated by a central fast flow in hydrodynamic situations. Instead, the implosion conjecture is still adequate for interpreting these events, and based on this, we propose different models for the two types of implosions. We categorize them into these models according to their distinct observational properties in terms of eruptiveness, dynamic timing, distance and speed. The first type is similar to the event in Chapter 2 and is suggested to be eruption-driven implosions, with the rapid contraction of peripheral loops during the rise stage of the impulsive phase when the filament erupts and is removed from the core region. The second type is new and found to be more likely related to the flare, thus called flare-driven implosions where loop contracts through the entire impulsive phase, reflecting the continuous magnetic energy conversion in the flare underneath the shrinking loops. Finally, we also argue that eruption-driven peripheral implosions may not always occur and could be suppressed when the originally underlying filament is heavily mass-loaded, because its non-negligible gravity may play an important role in the global dynamic

evolution, which would make one of the assumptions for the implosion conjecture in Hudson (2000) fail. This proposal may serve as an alternative explanation for the rarity of observed implosion behaviours in solar eruption events.

In Section 1.3.4, we argue that inflow is a special type of implosion. Then in Chapter 4, we study one excellent example of this kind and associated reconnection flows. The favorable location and perspective allow this first comprehensive observation of reconnection flows in a flare on the solar disk, which include the inflows from both sides toward the presumed central diffusion region; beneath it retracting loops as the outflows; cooling plasma settling as the downflows and also the chromospheric evaporation along these loops. We propose that the extended blueshift area just adjacent to the intense evaporation feature can be associated with two types of upflows, one along a narrow open field corridor and the other along the expanding closed arcade field. We argue that the expansion and induced depressurization of the arcade field can generate an upflow from the coronal base. And the open field corridor, which may correspond to separatrices or QSLs in the heliosphere, could create a different upflow via magnetic reconnection with nearby closed field. Making a distinction between the two upflow components helps solve the long-standing problem of whether the blueshift-related upflows at the AR boundary propagate along open or large-scale closed field, and the upflow along the expanding closed field which is also the inflow field may help alleviate the "electron number problem" to some extent, as it can provide more particles to the reconnection region or other acceleration regions. Moreover, the reconnection rates for the inflows at both sides in this long-duration event are estimated to be in the fast reconnection regime, compared to the slow Sweet-Parker rate.

5.2 Future Work

Though the implosion conjecture was proposed almost two decades ago, observations of such field imploding motion are still rare, compared to numerous eruptions and flares detected, and the understanding of this phenomenon is also far from complete. The aim of my future work is to study the physical mechanisms of implosions and intimately related phenomena like disappearance and oscillations of coronal loops (Figure 5.1). The open issues that have been identified in our previous study are described as below, which I propose to investigate in the future using advanced

magnetohydrodynamic simulations successfully developed and applied by Jiang et al. (2016a,c), combined with high spatial and temporal resolution extreme ultraviolet (EUV) imaging from Solar Dynamics Observatory/Atmospheric Imaging Assembly (SDO/AIA). The answers to these questions will help us understand coronal dynamics and solar physics in more depth.

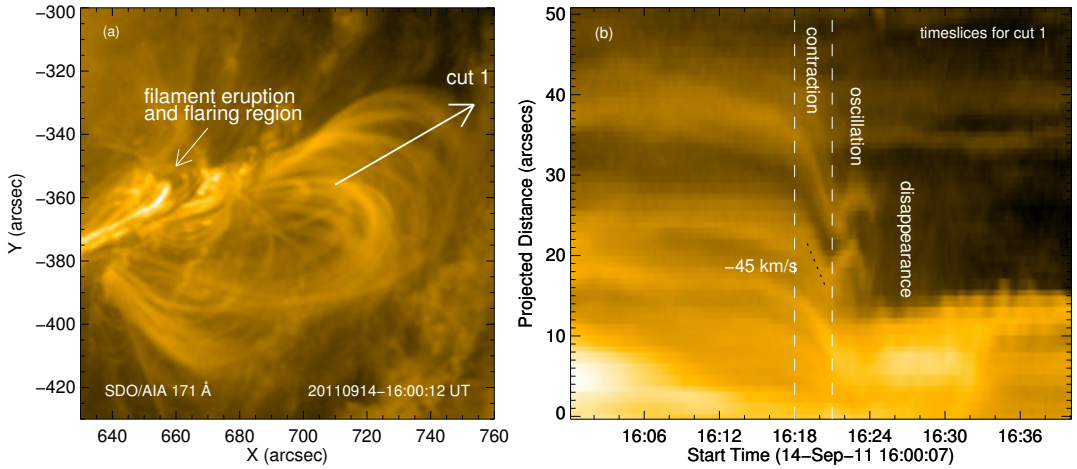

Figure 5.1: (a) Image for the event SOL2011-09-14T16:26. Cut 1 is for measuring the evolution of the contracting loops. (b) Timeslices for cut 1, showing the contraction, oscillation and disappearance of the contracting loops.

I. **Does the line-tied magnetic field really contract?** Previous authors often report apparent peripheral coronal loop contractions in a face-on geometry on the solar disk, accompanied by central filament or arcade eruptions, but these events are plagued by projection effects so that loop contraction could be either true implosion or just a change in loop inclination. In Chapter 2, we have proven the reality of the contraction nature indirectly from nonlinear force-free field (NLFFF) extrapolations and arguments from observations in one favourable case near the disk center, and Chapter 3 has shown the loop contractions unambiguously with the loop in an edge-on state. However, there are still some cases where the loops on the disk exhibit very strange kinetic motion in terms of their locations and geometry. A more severe situation is that according to the implosion conjecture, every event involving energy release should have field imploding signatures; and the observation in Simões et al.

(2013) even shows a general trend that the more distant the peripheral loop from the energy releasing core is, the more dramatically in distance and speed it implodes; however, for some major flares without eruptions on the disk, we usually do not observe the arcade overlying the flaring core or any associated implosion signatures, thus the questions that could be addressed using MHD simulations are: does the invisible overlying arcade in these events actually implode, and what is its dynamic characteristic? Even if NLFFF extrapolations may help provide a hint at these problems, the detailed dynamics still cannot be explored by this method as it only applies to pre- and post-flare equilibrium states. An MHD simulation, able to capture the coronal evolution, may help us to further understand loop dynamics and their relationship to the coronal magnetic energy.

II. **What is the physical mechanism causing loop contractions?** Though Hudson (2000) predicted loop contraction in solar eruptions and flares on the basis of reduction of magnetic pressure, Zuccarello et al. (2017) proposed an alternative explanation using an analog of vortices created by a central fast flow in hydrodynamics. They argued that the loop contraction is induced by enhanced tension caused by compressional Alfvén waves originating from the erupting field. In Chapter 3 we have presented EUV imaging observations that cannot be explained by the scenario of Zuccarello et al. (2017). However, what we lack now is further and more robust evidence from exact physical quantities of the evolving magnetic field, which unfortunately cannot be obtained by either observations or NLFFF extrapolations up to now. And also these two approaches are not enough to reveal the detailed magnetic reconnection process and corresponding energy transport concealed in the invisible magnetic field, thus are unable to prove the model for the new type of implosions which is suggested to be related to flares without eruptions in Chapter 3.

III. **Why do the contracting loops disappear and where are they going?** Very interestingly, the imploding loops in most of the reported events disappear at the observing wavelength at the end (e.g., Figure 5.1). So far we have not understood the underlying physics of this phenomenon. What we can imagine is plasma cooling, heating, or depletion (draining down to the chromosphere or diffusion into the flaring region). In one particular case, we found possible

evidence of heating, which might be caused by the betatron mechanism in a collapsing magnetic trap. According to this argument, we would expect that some of the invisible overlying arcade before the flare in some events could be heated to emit at the present observing passband during its implosion. However, up to now we have not noticed such phenomena. Thus, the physical mechanism behind the disappearance of these imploding loops is still mysterious. And because of the disappearance, we cannot track their subsequent evolution in observation. Thus another question to address using MHD simulations is: will they stay at the positions when they disappear, or implode further, or even inflate instead? Especially, what would happen around the interface between the imploding loops and the flaring core? And would the imploding loops provide extra plasma to the flaring region to be heated, or provide extra magnetic field to diffuse into the flaring core to be dissipated? We ask this because in some cases in Chapters 2 and 3, we noted a second major peak in GOES soft X-ray flux just after the contracting loops disappear.

IV. **What is the mechanism driving loop oscillations and will the oscillation affect the flaring core?** In some of the cases when a filament eruption is involved, we observed peripheral loops oscillating during or after their contraction (e.g., Figure 5.1, and Sun et al. 2012; Simões et al. 2013). Russell et al. (2015) proposed a model that considers a one-loop system as a simple harmonic oscillator, showing that the contracting and oscillating behaviours can be reproduced in a general way by the change in loop equilibrium position due to magnetic energy release underneath. However, inspired by the simulation of Zuccarello et al. (2017) and combining it with the idea of our work in Chapter 3, we notice that around the interface between the expanding and contracting fields in the periphery, there may exist a vortex center that could also generate loop oscillations. And Liu & Wang (2010) suggested that the interaction between the contracting loop and surrounding ones (one of the reasons we speculate is due to magnetic pressure gradient) may also make them oscillate (MHD waves). Thus, the character of the real physics behind this phenomenon and whether they can act together to produce the observations are still unknown. A further question is: will this field oscillation propagate into the flaring core region and modulate the physical conditions for reconnection there as proposed by Simões et al. (2013, 2015), which serves as an alternative way to explain flare SXR and

radio pulsations?

To solve these problems where observations by present instruments and NLFFF extrapolations for pre- and post-flare stages are on their own not adequate, the state-of-the-art data-driven magnetohydrodynamic simulation method "3D MHD AR evolution (DARE) model" developed by Jiang et al. (2016a,c) provides us with an unprecedented approach, especially in combination with the newly released high-cadence (up to 90s vs previous 12min) photospheric magnetograms (Sun et al. 2017). We propose to use the advanced method to study the event in Chapter 2, an event with strange geometry and motion with respect to its location in our archive, and a major flare on the disk without an eruption, which would reveal the detailed magnetohydrodynamic evolution information, e.g., changes in magnetic field quantities like magnetic pressure and tension, magnetic field redistribution and reconfiguration, corresponding magnetic field disturbance propagation and energy transport, and variation in plasma velocity field, thus able to help resolve Problems I, II and III. The simulations of the events in Sun et al. (2012) and Simões et al. (2013), and the first event in Chapter 3 would be excellent opportunities for validation of the method in reproducing realistic oscillations in the corona, and may give us helpful insights into Problem IV. We expect that the investigations using the advanced simulation method on this topic in the future can provide deeper and more comprehensive understanding on solar coronal dynamics. The ideal set of instruments with higher sensitivity across a wider temperature range than present, covering the full Sun with 3D stereoscopic view, is also wished for in future solar missions.

Bibliography

Abbo, L., Ofman, L., et al. 2016, *Space Science Reviews*, 201, 55

Alexander, D. & Metcalf, T. R. 1997, *The Astrophysical Journal*, 489, 442

Altschuler, M. D. & Newkirk, G. 1969, *Solar Physics*, 9, 131

Aly, J. J. 1984, *The Astrophysical Journal*, 283, 349

Aly, J. J. 1991, *The Astrophysical Journal, Letters*, 375, L61

Amari, T., Boulmezaoud, T. Z., et al. 1998, *Astronomy and Astrophysics*, 339, 252

Amari, T., Canou, A., et al. 2014, *Nature*, 514, 465

Antiochos, S. K., DeVore, C. R., et al. 1999, *The Astrophysical Journal*, 510, 485

Antiochos, S. K., Mikić, Z., et al. 2011, *The Astrophysical Journal*, 731, 112

Aschwanden, M. J. 2005, Physics of the Solar Corona. An Introduction with Problems and Solutions (2nd edition)

Aschwanden, M. J., Schmahl, E., et al. 2002, *Solar Physics*, 210, 193

Aulanier, G., DeLuca, E. E., et al. 2000, *The Astrophysical Journal*, 540, 1126

Aulanier, G., Démoulin, P., et al. 2005, *Astronomy and Astrophysics*, 430, 1067

Baker, D., van Driel-Gesztelyi, L., et al. 2009, *The Astrophysical Journal*, 705, 926

Bemporad, A., Soenen, A., et al. 2010, *The Astrophysical Journal*, 718, 251

Bi, Y., Jiang, Y., et al. 2014, *The Astrophysical Journal*, 790, 100

Boerner, P., Edwards, C., et al. 2012, *Solar Physics*, 275, 41

Borrero, J. M., Tomczyk, S., et al. 2011, *Solar Physics*, 273, 267

Boutry, C., Buchlin, E., et al. 2012, *The Astrophysical Journal*, 752, 13

Brooks, D. H., Ugarte-Urra, I., et al. 2015, *Nature Communications*, 6, 5947

Brown, C. M., Feldman, U., et al. 2008, *The Astrophysical Journal, Supplement*, 176, 511

Brown, J. C. & Melrose, D. B. 1977, *Solar Physics*, 52, 117

Carmichael, H. 1964, *NASA Special Publication*, 50, 451

Craig, I. J. D. & Brown, J. C. 1976, *Astronomy and Astrophysics*, 49, 239

Culhane, J. L., Harra, L. K., et al. 2007, *Solar Physics*, 243, 19

Dahlburg, R. B., Antiochos, S. K., et al. 1991, *The Astrophysical Journal*, 383, 420

Del Zanna, G. 2008, *Astronomy and Astrophysics*, 481, L49

Del Zanna, G., Aulanier, G., et al. 2011, *Astronomy and Astrophysics*, 526, A137

Del Zanna, G., Landini, M., et al. 2002, *Astronomy and Astrophysics*, 385, 968

Démoulin, P., Baker, D., et al. 2013, *Solar Physics*, 283, 341

Demoulin, P. & Priest, E. R. 1992, *Astronomy and Astrophysics*, 258, 535

Dere, K. P., Landi, E., et al. 1997, *Astronomy and Astrophysics, Supplement*, 125, 149

DeRosa, M. L., Wheatland, M. S., et al. 2015, *The Astrophysical Journal*, 811, 107

Doschek, G. A., Warren, H. P., et al. 2008, *The Astrophysical Journal*, 686, 1362

Dudík, J., Aulanier, G., et al. 2008, *Solar Physics*, 248, 29

Dudík, J., Zuccarello, F. P., et al. 2017, *The Astrophysical Journal*, 844, 54

Edwards, S. J., Parnell, C. E., et al. 2016, *Solar Physics*, 291, 117

Emslie, A. G. & Sturrock, P. A. 1982, *Solar Physics*, 80, 99

Fan, Y. 2017, *The Astrophysical Journal*, 844, 26

Fan, Y. & Gibson, S. E. 2007, *The Astrophysical Journal*, 668, 1232

Filippov, B. 2014, *Monthly Notices of the Royal Astronomical Society*, 442, 2892

Fisher, G. H., Bercik, D. J., et al. 2012, *Solar Physics*, 277, 59

Fisk, L. A. 2003, *Journal of Geophysical Research (Space Physics)*, 108, 1157

Fisk, L. A., Zurbuchen, T. H., et al. 1999, *The Astrophysical Journal*, 521, 868

Fletcher, L. & Hudson, H. S. 2008, *The Astrophysical Journal*, 675, 1645

Forbes, T. G. & Acton, L. W. 1996, *The Astrophysical Journal*, 459, 330

Gary, G. A. & Hagyard, M. J. 1990, *Solar Physics*, 126, 21

Gibson, S. E. & Fan, Y. 2006, *Journal of Geophysical Research (Space Physics)*, 111, A12103

Golub, L., Deluca, E., et al. 2007, *Solar Physics*, 243, 63

Gosain, S. 2012, *The Astrophysical Journal*, 749, 85

Grad, H. & Rubin, H. 1958, Hydromagnetic Equilibria and Force-free Fields (U.S. Government Printing Office)

Guo, Y., Cheng, X., et al. 2017, *Science in China Earth Sciences*, 60

Hannah, I. G., Hudson, H. S., et al. 2011, *Space Science Reviews*, 159, 263

Hannah, I. G. & Kontar, E. P. 2012, *Astronomy and Astrophysics*, 539, A146

Hannah, I. G. & Kontar, E. P. 2013, *Astronomy and Astrophysics*, 553, A10

Hansen, P. C. 1992, *Inverse Problems*, 8, 849

Harra, L. K., Sakao, T., et al. 2008, *The Astrophysical Journal, Letters*, 676, L147

Hirayama, T. 1974, *Solar Physics*, 34, 323

Hoeksema, J. T., Liu, Y., et al. 2014, *Solar Physics*, 289, 3483

Högbom, J. A. 1974, *Astronomy and Astrophysics, Supplement*, 15, 417

Hood, A. W. & Priest, E. R. 1979, *Solar Physics*, 64, 303

Howard, R. A., Moses, J. D., et al. 2008, *Space Science Reviews*, 136, 67

Hudson, H. S. 2000, *The Astrophysical Journal, Letters*, 531, L75

Hudson, H. S., Acton, L. W., et al. 1999, *The Astrophysical Journal, Letters*, 513, L83

Hudson, H. S., Fisher, G. H., et al. 2008, in Astronomical Society of the Pacific Conference Series, Vol. 383, Subsurface and Atmospheric Influences on Solar Activity, ed. R. Howe, R. W. Komm, K. S. Balasubramaniam, & G. J. D. Petrie, 221

Hurford, G. J., Schmahl, E. J., et al. 2002, *Solar Physics*, 210, 61

Imada, S., Aoki, K., et al. 2013, *The Astrophysical Journal, Letters*, 776, L11

Isobe, H., Yokoyama, T., et al. 2002, *The Astrophysical Journal*, 566, 528

Jenkins, J. M., Long, D. M., et al. 2018, *Solar Physics*, 293, 7

Ji, H., Huang, G., et al. 2007, *The Astrophysical Journal*, 660, 893

Jiang, C., Wu, S. T., et al. 2016a, *Nature Communications*, 7, 11522

Jiang, C., Wu, S. T., et al. 2016b, *The Astrophysical Journal*, 828, 62

Jiang, C., Wu, S. T., et al. 2016c, *The Astrophysical Journal*, 828, 62

Joshi, N. C., Srivastava, A. K., et al. 2013, *The Astrophysical Journal*, 771, 65

Kamio, S., Peter, H., et al. 2011, *Astronomy and Astrophysics*, 532, A96

Karpen, J. T., Antiochos, S. K., et al. 2012, *The Astrophysical Journal*, 760, 81

Kliem, B. & Török, T. 2006, *Physical Review Letters*, 96, 255002

Kopp, R. A. & Pneuman, G. W. 1976, *Solar Physics*, 50, 85

Kosugi, T., Matsuzaki, K., et al. 2007, *Solar Physics*, 243, 3

Krucker, S., Hurford, G. J., et al. 2008, *The Astrophysical Journal, Letters*, 678, L63

Kushwaha, U., Joshi, B., et al. 2015, *The Astrophysical Journal*, 807, 101

Landi, E., Young, P. R., et al. 2013, *The Astrophysical Journal*, 763, 86

Leka, K. D., Barnes, G., et al. 2009, *Solar Physics*, 260, 83

Lemen, J. R., Title, A. M., et al. 2012, *Solar Physics*, 275, 17

Li, L., Zhang, J., et al. 2016, *Nature Physics*, 12, 847

Li, Y., Sun, X., et al. 2017, *The Astrophysical Journal*, 835, 190

Lin, J. 2004, *Solar Physics*, 222, 115

Lin, J., Ko, Y.-K., et al. 2005, *The Astrophysical Journal*, 622, 1251

Lin, R. P., Dennis, B. R., et al. 2002, *Solar Physics*, 210, 3

Liu, R., Alexander, D., et al. 2009a, *The Astrophysical Journal*, 691, 1079

Liu, R., Liu, C., et al. 2012a, *The Astrophysical Journal*, 757, 150

Liu, R. & Wang, H. 2009, *The Astrophysical Journal, Letters*, 703, L23

Liu, R. & Wang, H. 2010, *The Astrophysical Journal, Letters*, 714, L41

Liu, R., Wang, H., et al. 2009b, *The Astrophysical Journal*, 696, 121

Liu, W., Chen, Q., et al. 2013, *The Astrophysical Journal*, 767, 168

Liu, W. & Ofman, L. 2014, *Solar Physics*, 289, 3233

Liu, Y. 2008, *The Astrophysical Journal, Letters*, 679, L151

Liu, Y., Hoeksema, J. T., et al. 2012b, *Solar Physics*, 279, 295

Longcope, D. W., Guidoni, S. E., et al. 2009, *The Astrophysical Journal, Letters*, 690, L18

Mann, G., Warmuth, A., et al. 2009, *Astronomy and Astrophysics*, 494, 669

McClymont, A. N. & Fisher, G. H. 1989, *Washington DC American Geophysical Union Geophysical Monograph Series*, 54, 219

McKenzie, D. E. & Hudson, H. S. 1999, *The Astrophysical Journal, Letters*, 519, L93

Meegan, C., Lichti, G., et al. 2009, *The Astrophysical Journal*, 702, 791

Metcalf, T. R. 1994, *Solar Physics*, 155, 235

Metcalf, T. R., Hudson, H. S., et al. 1996, *The Astrophysical Journal*, 466, 585

Metcalf, T. R., Leka, K. D., et al. 2006, *Solar Physics*, 237, 267

Mikic, Z. & McClymont, A. N. 1994, in Astronomical Society of the Pacific Conference Series, Vol. 68, Solar Active Region Evolution: Comparing Models with Observations, ed. K. S. Balasubramaniam & G. W. Simon, 225

Milligan, R. O. & Dennis, B. R. 2009, *The Astrophysical Journal*, 699, 968

Morgan, H. & Druckmüller, M. 2014, *Solar Physics*, 289, 2945

Nakagawa, Y. 1974, *The Astrophysical Journal*, 190, 437

Narukage, N. & Shibata, K. 2006, *The Astrophysical Journal*, 637, 1122

Neupert, W. M. 1968, *The Astrophysical Journal, Letters*, 153, L59

Pascoe, D. J., Russell, A. J. B., et al. 2017, *Astronomy and Astrophysics*, 607, A8

Pesnell, W. D., Thompson, B. J., et al. 2012, *Solar Physics*, 275, 3

Petrie, G. J. D. 2012, *The Astrophysical Journal*, 759, 50

Petrie, G. J. D. 2016, *Solar Physics*, 291, 791

Petrie, G. J. D. & Sudol, J. J. 2010, *The Astrophysical Journal*, 724, 1218

Priest, E. 2014, Magnetohydrodynamics of the Sun

Priest, E. R. & Forbes, T. G. 2002, *Astronomy and Astrophysics Reviews*, 10, 313

Puetter, R. C. 1995, *International Journal of Imaging Systems Technology*, 6, 314

Rachmeler, L. A., DeForest, C. E., et al. 2009, *The Astrophysical Journal*, 693, 1431

Reeves, K. K., Linker, J. A., et al. 2010, *The Astrophysical Journal*, 721, 1547

Reeves, K. K., Seaton, D. B., et al. 2008, *The Astrophysical Journal*, 675, 868

Roumeliotis, G. 1996, *The Astrophysical Journal*, 473, 1095

Roussev, I. I., Forbes, T. G., et al. 2003, *The Astrophysical Journal, Letters*, 588, L45

Russell, A. J. B., Simões, P. J. A., et al. 2015, *Astronomy and Astrophysics*, 581, A8

Rust, D. M. & Kumar, A. 1996, *The Astrophysical Journal, Letters*, 464, L199

Sakao, T., Kano, R., et al. 2007, *Science*, 318, 1585

Sakurai, T. 1976, *Publications of the ASJ*, 28, 177

Sakurai, T. 1981, *Solar Physics*, 69, 343

Sarkar, A., Vaidya, B., et al. 2017, *ArXiv e-prints*

Sato, J., Kosugi, T., et al. 1999, *Publications of the ASJ*, 51, 127

Savage, S. L., Holman, G., et al. 2012, *The Astrophysical Journal*, 754, 13

Schatten, K. H., Wilcox, J. M., et al. 1969, *Solar Physics*, 6, 442

Scherrer, P. H., Schou, J., et al. 2012, *Solar Physics*, 275, 207

Schmahl, E. J., Pernak, R. L., et al. 2007, *Solar Physics*, 240, 241

Schmieder, B., Aulanier, G., et al. 2015, *Solar Physics*, 290, 3457

Schou, J., Scherrer, P. H., et al. 2012, *Solar Physics*, 275, 229

Schrijver, C. J. 2001, *Solar Physics*, 198, 325

Shen, J., Zhou, T., et al. 2014, *The Astrophysical Journal*, 791, 83

Simões, P. J. A., Fletcher, L., et al. 2013, *The Astrophysical Journal*, 777, 152

Simões, P. J. A., Hudson, H. S., et al. 2015, *Solar Physics*, 290, 3625

Simões, P. J. A. & Kontar, E. P. 2013, *Astronomy and Astrophysics*, 551, A135

Sinclair Reid, H. A. & Ratcliffe, H. 2014, *Research in Astronomy and Astrophysics*, 14, 773

Stix, M. 2004, The sun : an introduction

Sturrock, P. A. 1966, *Nature*, 211, 695

Sturrock, P. A. 1991, *The Astrophysical Journal*, 380, 655

Sturrock, P. A., Antiochos, S. K., et al. 1994, *The Astrophysical Journal*, 431, 870

Sturrock, P. A., Weber, M., et al. 2001, *The Astrophysical Journal*, 548, 492

Su, Y., Veronig, A. M., et al. 2013, *Nature Physics*, 9, 489

Sudol, J. J. & Harvey, J. W. 2005, *The Astrophysical Journal*, 635, 647

Suematsu, Y., Tsuneta, S., et al. 2008, *Solar Physics*, 249, 197

Sun, J. Q., Cheng, X., et al. 2015a, *Nature Communications*, 6, 7598

Sun, X., Bobra, M. G., et al. 2015b, *The Astrophysical Journal, Letters*, 804, L28

Sun, X., Hoeksema, J. T., et al. 2017, *The Astrophysical Journal*, 839, 67

Sun, X., Hoeksema, J. T., et al. 2012, *The Astrophysical Journal*, 748, 77

Syntelis, P., Gontikakis, C., et al. 2012, *Solar Physics*, 280, 475

Thalmann, J. K., Veronig, A., et al. 2016, *The Astrophysical Journal*, 826, 143

Tsuneta, S., Ichimoto, K., et al. 2008, *Solar Physics*, 249, 167

Vashalomidze, Z., Kukhianidze, V., et al. 2015, *Astronomy and Astrophysics*, 577, A136

Veronig, A. M., Karlický, M., et al. 2006, *Astronomy and Astrophysics*, 446, 675

Wang, H. & Liu, C. 2010, *The Astrophysical Journal, Letters*, 716, L195

Wang, J., Simões, P. J. A., et al. 2016, *The Astrophysical Journal*, 833, 221

Wang, J., Simões, P. J. A., et al. 2017, *The Astrophysical Journal, Letters*, 847, L1

Wang, J., Simoes, P. J. A., et al. 2018, *ArXiv e-prints*

Wheatland, M. S. 2004, *Solar Physics*, 222, 247

Wheatland, M. S., Sturrock, P. A., et al. 2000, *The Astrophysical Journal*, 540, 1150

Wiegelmann, T. 2004, *Solar Physics*, 219, 87

Wiegelmann, T. & Inhester, B. 2010, *Astronomy and Astrophysics*, 516, A107

Wiegelmann, T., Inhester, B., et al. 2006, *Solar Physics*, 233, 215

Wiegelmann, T. & Neukirch, T. 2003, *Nonlinear Processes in Geophysics*, 10, 313

Wiegelmann, T., Solanki, S. K., et al. 2013, *Solar Physics*, 283, 253

Wiegelmann, T., Thalmann, J. K., et al. 2012, *Solar Physics*, 281, 37

Woods, T. N., Eparvier, F. G., et al. 2012, *Solar Physics*, 275, 115

Yan, X. L., Pan, G. M., et al. 2013, *Astronomical Journal*, 145, 153

Yang, S., Zhang, J., et al. 2015, *The Astrophysical Journal, Letters*, 798, L11

Yokoyama, T., Akita, K., et al. 2001, *The Astrophysical Journal, Letters*, 546, L69

Zheng, R., Korsós, M. B., et al. 2015, *The Astrophysical Journal*, 809, 45

Zhu, C., Liu, R., et al. 2016, *The Astrophysical Journal, Letters*, 821, L29

Zuccarello, F. P., Aulanier, G., et al. 2017, *The Astrophysical Journal*, 837, 115

Zuccarello, F. P., Aulanier, G., et al. 2015, *The Astrophysical Journal*, 814, 126